

NOTE TO USERS

The original manuscript received by UMI contains pages with indistinct and/or slanted print. Pages were microfilmed as received.

This reproduction is the best copy available

UMI

**CHARACTERIZATION OF QUANTUM WELLS USING DEGREE OF
POLARIZATION OF PHOTOLUMINESCENCE**

By

LAKSHMI BALASUBRAMANIAN, B.Sc., M.Sc.

A Thesis

Submitted to the School of Graduate Studies

in Partial Fulfilment of the Requirements

for the Degree

Doctor of Philosophy

McMaster University

© Copyright by Lakshmi Balasubramanian, June 1997



**National Library
of Canada**

**Acquisitions and
Bibliographic Services**

**395 Wellington Street
Ottawa ON K1A 0N4
Canada**

**Bibliothèque nationale
du Canada**

**Acquisitions et
services bibliographiques**

**395, rue Wellington
Ottawa ON K1A 0N4
Canada**

Your file Votre référence

Our file Notre référence

The author has granted a non-exclusive licence allowing the National Library of Canada to reproduce, loan, distribute or sell copies of this thesis in microform, paper or electronic formats.

The author retains ownership of the copyright in this thesis. Neither the thesis nor substantial extracts from it may be printed or otherwise reproduced without the author's permission.

L'auteur a accordé une licence non exclusive permettant à la Bibliothèque nationale du Canada de reproduire, prêter, distribuer ou vendre des copies de cette thèse sous la forme de microfiche/film, de reproduction sur papier ou sur format électronique.

L'auteur conserve la propriété du droit d'auteur qui protège cette thèse. Ni la thèse ni des extraits substantiels de celle-ci ne doivent être imprimés ou autrement reproduits sans son autorisation.

0-612-30070-6

Abstract

The state of polarization of photoluminescence that is emitted along [001] and [110] crystallographic orientations has been studied to obtain quantitative information on the interfacial strain, thickness and biaxial strain in InP/InGaAs(P)/InP quantum wells. It is demonstrated that the edge emission from quantum wells is a sensitive function of the strain and thickness of the quantum well. The anisotropic polarization of photoluminescence that is emitted normal to the plane of the quantum well provides information regarding the interfacial features. This anisotropy has been correlated to the anisotropic strain field that is associated with the strained bonds at the interfaces of the quantum wells.

Acknowledgements

I would like to thank my supervisor, Dr. Dan Cassidy for his insight, guidance, and encouragement during this program. I sincerely thank Brad Robinson for innumerable discussions during the course of my study. I wish to thank Dr. Thompson and my committee members, Prof. Simmons and Dr. Weatherly for their suggestions and time. I am grateful to Scott McMaster for growing MBE samples. I owe Doug a lot for helping me in the lab during these four years. V-groove samples were provided by Jun Wang and the strain gauge used for calibration was developed by Paul Colbourne during his studies at McMaster. Ion-implantation was done by Doris Stevanovic.

I wish to acknowledge the financial support provided by the Canadian Commonwealth and Fellowship Program, and the Department of Engineering Physics. I am grateful to the Society for Applied Microwave Electronics and Engineering Research (SAMEER), India for sanctioning a study leave to complete my degree.

I am extremely thankful to my parents, sisters, and my nephew Balaji for their love and encouragement. Of course without my husband's friendship, love, and moral support, it would have been a difficult task for me to pull through four years without going home. Finally, this thesis is in memory of my little nephew, Prasanna and my father-in-law Dr. P. Muthuswamy.

Table of Contents

Chapter 1.	Introduction	1
1.1	Background	1
1.2	New contributions	8
Chapter 2.	Experimental Methods	12
2.1	Introduction	12
2.2	Experimental Technique	12
2.3	System Calibration	18
2.3.1	Experimental Results	19
2.3.2	Simulation Using ANSYS	23
2.4	Growth Aspects	27
2.4.1	Gas Source Molecular Beam Epitaxy (GSMBE)	27
2.4.2	Surface Reconstruction	28
2.5	Summary	30
Chapter 3.	Degree of Polarization of Luminescence From the Facet	31
3.1	Introduction	31
3.2	Experimental Details	32
3.3	Results of DOP_{110} Measurements	36
3.4	Discussion	42
3.5	TE and TM Spectral Measurements	55
3.6	Summary	56
Chapter 4.	Anisotropic Interfacial Strain	60
4.1	Introduction	60
4.2	Experimental Details	61
4.3	Results	63
4.4	Discussion	69
4.5	Other related Experiments	79
4.6	Summary	81
Chapter 5.	Valence Force Field Model	83
5.1	Introduction	83
5.2	The Model	84
5.3	Anisotropy between $[110]$ and $[\bar{1}\bar{1}0]$ directions	89
5.4	Anisotropy between $[100]$ and $[010]$ directions	93
5.5	Summary	97
Chapter 6.	Suggested Future Work and Conclusion	98

6.1	Suggested Future Work	98
6.2	Conclusion	102
Chapter 7.	Appendices	104
7.1	Appendix A	104
7.2	Appendix B	116
Chapter 8.	References	154

List of Figures

Figure 1.1	Constant energy bandgap curves for various combinations of 'x' and 'y' in $\text{In}_{1-x}\text{Ga}_x\text{As}_y\text{P}_{1-y}$	2
Figure 1.2	Schematic diagram showing energy levels in the conduction band and valence band as the thickness of the well decreases in the growth direction.	3
Figure 1.3	A schematic representation of the band structure of a tensile strained, unstrained and compressively strained direct bandgap tetrahedral semiconductor. E_g - Bandgap energy; CB - Conduction Band; HH - Heavy hole band; LH - Light hole band; SO - spin-orbit split-off band; Γ - zone center; k_{\parallel} - wave vector in the plane of growth; k_{\perp} - wave vector along the growth direction .	4
Figure 1.4	Schematic of the apparatus used for the polarization-resolved luminescence measurements.	7
Figure 1.5	Typical material structure of the samples used in this work.	8
Figure 2.1	a) Experimental apparatus, and b) Scanning directions	14
Figure 2.2	Schematic of the simply-supported beam-bending experiment.	19
Figure 2.3	An image of the distribution of DOP for the V-groove structure for an external load of 0.2N. The fringe spacing is .019.	21
Figure 2.4	Images of distribution of DOP and ROP of InP V-groove structures for four different applied stress: a) $F = 0$; b) $F = 0.047 \text{ N}$; c) $F = 0.21 \text{ N}$; d) $F = -0.159 \text{ N}$.	22
Figure 2.5	Schematic of the V-groove geometry used in ANSYS. Δ represents the displacement constraint at that location.	24
Figure 2.6	Images of the distributions of DOP and ROP of V-groove structures obtained from: (a and b) - Experiment; (c and d) - Simulation using ANSYS.	25

Figure 2.7	a) Ball-and stick model of the GaAs(001)-(2×4) reconstructed surface with three dimer rows and one missing dimer row per unit cell. b) Corresponding RHEED pattern viewed along [110] and [1 $\bar{1}$ 0] directions.	29
Figure 3.1	A typical material structure of sample set I.	33
Figure 3.2	a) The material structure of sample Set II. b) Top view of the sample.	35
Figure 3.3	Experimental apparatus to perform polarization-resolved integrated photoluminescence and spectrally-resolved photoluminescence measurements.	36
Figure 3.4	Measured DOP ₁₁₀ on sample Set I. The variation of DOP ₁₁₀ with quantum well thickness for three different strain conditions is shown.	37
Figure 3.5	a) Illustration of a scan across the facet of sample Set II along the z direction. The three layers of thickness 500, 100, and 50 Å are spatially resolved and are indicated in the figure. Also shown is the direction of the scan in the inset. b) Illustration of DOP across the facet. The locations of the three layers are indicated.	39
Figure 3.6	a) Measured DOP ₁₁₀ on sample Set II as the sample is scanned across the facet from location A to B. The slopes of the lines are indicated in the figure. b) The room-temperature photoluminescence spectra at location A. c) The room-temperature photoluminescence spectra at location B.	41
Figure 3.7	Coordinate system used in the discussion for the quantum well structure.	49
Figure 3.8	Relative band edge transition strengths for quantum wells.	52
Figure 3.9	Theoretical prediction of variation of DOP ₁₁₀ with quantum well thickness for four different strain conditions.	54
Figure 3.10	Room-temperature polarization-resolved photoluminescence spectra on a	

	100Å-thick quantum well for three conditions of strain: a) 1% compression; b) lattice-matched; c) 1% tension.	57
Figure 3.11	Room-temperature polarization-resolved photoluminescence spectra on three lattice-matched layers of thicknesses 30, 100, and 300 Å: a) 300 Å; b) 100 Å; c) 30 Å. The TM intensity in (c) is scaled by a factor of 10.	58
Figure 4.1	Experimental apparatus	61
Figure 4.2	Typical a) Material structure, and b) Growth sequence	63
Figure 4.3	Variation of DOP_{001} with the reciprocal of the quantum well thickness ($1/L$). L is varied from 300 Å to 20 Å.	64
Figure 4.4	Variation of DOP_{001} with the dwell time in phosphorous.	67
Figure 4.5	14K PL spectra for three cases of dwell time in phosphorous (t_p): a) $t_p = 5$ sec., b) $t_p = 15$ sec., and c) $t_p = 55$ sec.	68
Figure 4.6	Variation of DOP_{001} with the Ga composition in the well.	69
Figure 4.7	Ball-and-stick model showing three stages of reconstruction at the bottom interface. a) P-terminated, (2×4)-reconstructed surface; b) Replacement of P by As when As was switched ON; c) Upon resuming the growth of InGaAs.	71
Figure 4.8	Ball-and-stick model showing three stages of reconstruction at the top interface. a) As-terminated, (2×4)-reconstructed surface; b) When P was switched ON, the surface is still As-terminated; c) Upon resuming the growth of InP.	72
Figure 4.9	Bonding schematic along $[110]$ and $[1\bar{1}0]$ directions. 'f' is the fraction of As atoms, and 'x' is the Ga content.	75
Figure 5.1	Zinc-blende crystal structure showing crystallographic orientations.	85
Figure 5.2	Propagation of strain field along $[110]$ and $[1\bar{1}0]$ directions into the quantum well due to a single Ga-P bond per $(N_x \times N_y)$ periodic structure at	

the interface.

89

- Figure 5.3 Theoretical prediction of variation of DOP_{001} with the inverse of number of monolayers in the quantum well. The thickness of the well shown in the figures is calculated from the distance between two atomic layers = 1.46 \AA ($a_{\text{InP}} / 4$, where a_{InP} is the lattice constant of InP). 91
- Figure 5.4 Propagation of shear strain into the quantum well and the cap layer due to a single Ga-P bond per $(N_x \times N_y)$ periodic structure at the well/cap layer interface. 94
- Figure 5.5 a) Experimental apparatus for polarization-resolved photoluminescence measurements. b) The crystallographic orientations of the sample. 95

List of Tables

Table 4.1	Variation of DOP_{001} with growth interruption time. I_1 is the buffer/QW interface and I_2 is the QW/cap layer interface.	65
Table 4.2	Variation of DOP_{001} , PL peak wavelength, and FWHM with the inverse of the ion-implantation dose.	80

Chapter 1. Introduction

1.1 Background

The past two decades have seen a phenomenal effort in the study of InP based alloy semiconductor materials and devices. The tremendous interest in opto-electronic and photonic technology has pushed InP based alloys to the forefront of semiconductor research. The bandgap energy of the ternary $\text{In}_{1-x}\text{Ga}_x\text{As}$ and quaternary $\text{In}_{1-x}\text{Ga}_x\text{As}_y\text{P}_{1-y}$ alloys can be varied over a wide range (0.71 to 1.35 eV) by varying the alloy composition [1,2,3,4] as shown in Fig. 1.1. The energy range includes the optimum wavelengths of minimum dispersion ($1.3 \mu\text{m}$) and of minimum absorption loss ($1.55 \mu\text{m}$) in silica based optical fibers, which are the medium of transmission for long-haul fiberoptic communication systems [5].

A major breakthrough in exploiting the electrical and optical properties of semiconductors was achieved when confinement of carriers to two dimensions became a reality. With the advancement in growth technology it was possible to grow epitaxial layers using molecular beam epitaxy (MBE) [6,7,8] and metalorganic chemical vapor deposition (MOCVD) with precise control over thickness and composition. This led to the realization of the theoretical ‘one-dimensional particle in a box’ problem in the name of a ‘quantum well’. In a quantum well, a thin ($\leq 300 \text{ \AA}$), lower bandgap material is sandwiched between

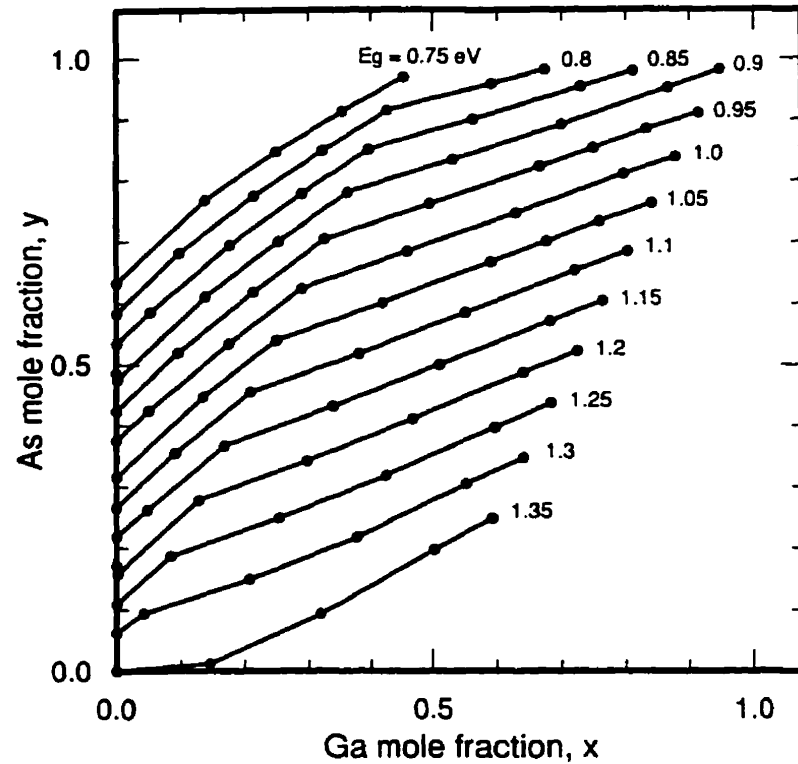


Figure 1.1 Constant energy bandgap curves for various combination of ‘x’ and ‘y’ in $\text{In}_{1-x}\text{Ga}_x\text{As}_y\text{P}_{1-y}$

higher bandgap materials. Well-known examples of quantum wells are AlGaAs/GaAs/AlGaAs and InP/InGaAsP/InP. As the thickness of the quantum well, L_z , becomes comparable to de Broglie wavelength of the particle, the separation between the quantized energy levels of the particles in the growth direction becomes much larger than the thermal broadening at room temperature. The carriers effectively behave as if their motion was bi-dimensional in the (x,y) plane and locked in one of the discrete bound states in the

direction of growth, z . Valence bands are more complicated than the conduction band due to the degenerate states at the zone center (Γ). Quantum-size effect lifts the degeneracy at the zone center with the heavy hole energy level shifting to a lower energy with respect to the light hole owing to the difference in the effective masses of the heavy and light holes [9,10,11,12,13]. The energy of the lowest state increases with the decrease in L_z which is illustrated in the schematic diagram, Fig.1.2.

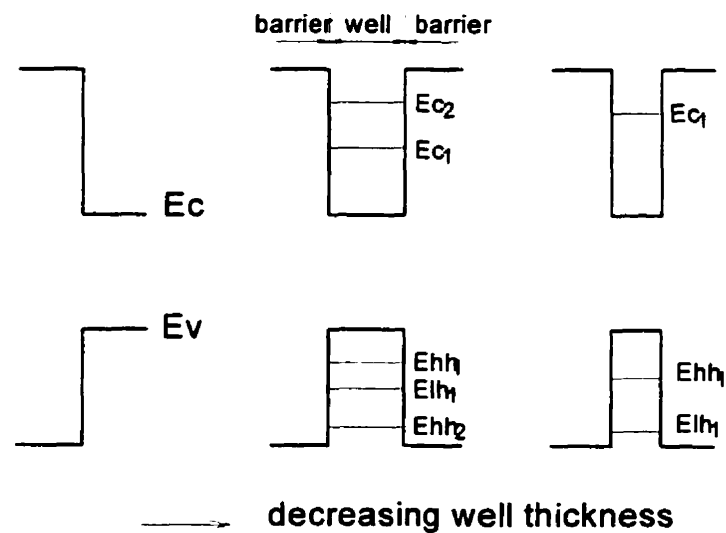


Figure 1.2 Schematic diagram showing energy levels in the conduction band and valence band as the thickness of the well decreases in the growth direction.

Introduction of elastic strain in the layers offers an additional degree of freedom to alter the energy separation between the heavy hole and the light hole. In the elastic regime and for coherent growth the lattice mismatch is accommodated by a tetragonal distortion

of the layer [14,15]. This results in lowering of the symmetry of the cubic structure, lifting the degeneracy at the zone center and creating an anisotropic valence band dispersion. When the lattice parameter of the epitaxial layer is larger (smaller) than that of the substrate, there is an in-plane compressive (tensile) strain in the layer. The variation of bandgap and band dispersion for three different strain conditions are depicted in Fig. 1.3 [16,17,18,19,20,21,22].

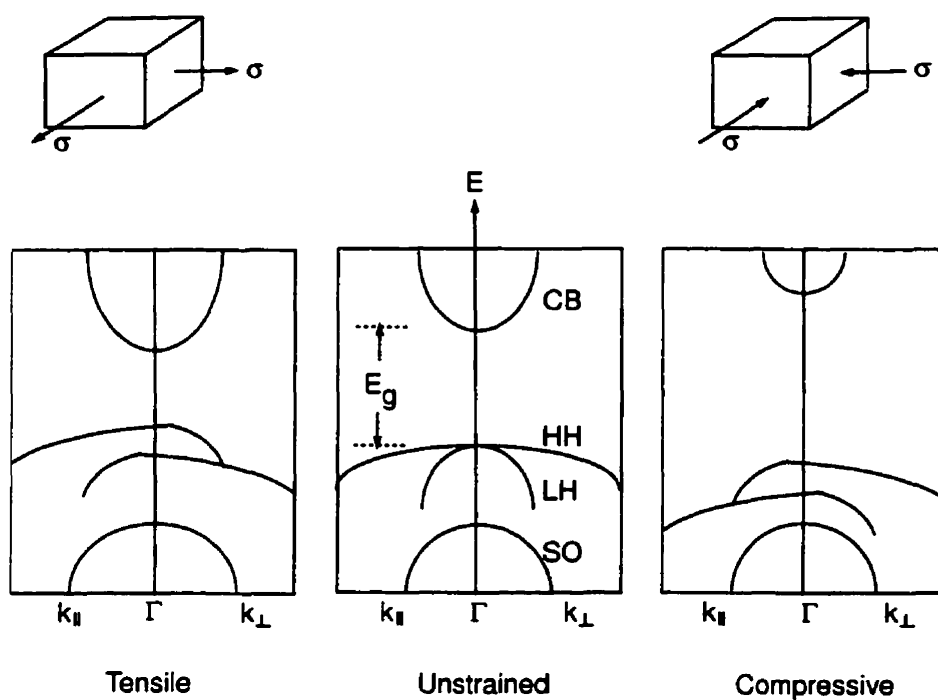


Figure 1.3 A schematic representation of the band structure of a tensile strained, unstrained and compressively strained direct bandgap tetrahedral semiconductor. E_g - Bandgap energy; CB - Conduction Band; HH - Heavy hole band; LH - Light hole band; SO - spin-orbit split-off band; Γ - zone center; $k_{||}$ - wave vector in the plane of growth; k_{\perp} - wave vector along the growth direction

In order for the heterostructure quantum wells to be a useful material for electrical and optical devices, it is desirable to have atomically smooth interfaces having an abrupt step potential with as low a density of defects as possible [23,24,25,26,27]. However, it is very hard to produce high quality abrupt interfaces and difficult to probe the structural disorder on the atomic scale. The structural, and chemical details of the interface affect the formation and distribution of electron states at the interface which in turn alter the electrical and optical properties of the heterostructures. Especially in the case of thin quantum wells ($<100\text{\AA}$), the impact of any interfacial perturbation on the properties of wells is larger since the relative volume of the interface with respect to the total quantum well is larger. The bonding arrangements at the interfaces become more complicated in heterostructures that require a switching between two Group V species, such as in the InGaAs/InP system [28]. Hence, a detailed knowledge of the structural and chemical properties of the epitaxial interfaces is a prerequisite to understand the performance of heterostructure devices.

It is evident from the above discussion that composition, strain and quantum size effect play a critical role in engineering the bandgap of InP/InGaAsP/InP semiconductors and the quality of the interfaces dictates the electrical and optical performances of heterostructure devices. Some of the important device parameters such as the emission (absorption) wavelength of a laser (detector), spectral output, threshold current, differential gain, and the state of polarization of the output of a laser depend on the strain in the material, thickness of the quantum well, and the quality of the interface. Hence, non-contact, fast, and accurate

means to measure the physical properties of materials and devices are needed to provide feedback to the growth personnel to optimize growth and verify materials.

The standard non-contact ex-situ technique for measurement of strain is x-ray diffraction while the standard technique for estimation of the thickness and composition of wells is an analysis of the spectrally-resolved photoluminescence or absorption. Multiple crystal x-ray diffraction is a useful technique for bulk and large period superlattices. However, the ability to measure the strain in single quantum wells diminishes for wells of thicknesses less than 100\AA [29,30]. Acquisition and analysis of spectrally-resolved luminescence data is a time-consuming technique to extract information on the thickness and composition.

Polarization-resolved photoluminescence has been shown to be a useful technique to map the strain field arising owing to device processing such as metallization and bonding [31,32,33], or due to the presence of defects such as edge or misfit dislocations in GaAs or InP semiconductor materials [34]. It is possible to achieve a strain resolution of 1×10^{-5} and a spatial resolution of better than $1\ \mu\text{m}$ using this technique. This technique basically measures the relative strength of luminescence polarized along two orthogonal directions. Figure 1.4 is a schematic of the apparatus used for the polarization-resolved photoluminescence measurements. Let 'z' be the direction of propagation and L_x , L_y be the magnitudes of the luminescence that are polarized in the 'x' and 'y' directions respectively.

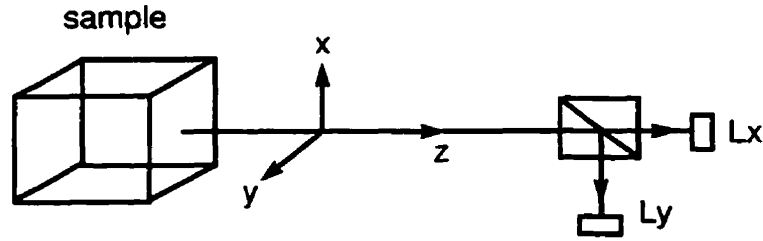


Figure 1.4 Schematic of the apparatus used for polarization-resolved luminescence measurements.

A parameter, degree of polarization of photoluminescence (DOP) is defined as

$$DOP_z = \frac{\int_0^{\infty} [L_x(E) - L_y(E)] R(E) dE}{\int_0^{\infty} [L_x(E) + L_y(E)] R(E) dE} \quad (1.1)$$

where $\int [L_x(E) + L_y(E)] R(E) dE$ and $\int [L_x(E) - L_y(E)] R(E) dE$ are the sum and difference of the intensities of L_x and L_y , integrated over all energy transitions. $R(E)$ is the responsivity of the detector. The magnitude of the DOP is a direct measure of the state of polarization of luminescence and is proportional to strain in the material [31]. The subscript in DOP refers to the direction of propagation of luminescence. In subsequent chapters, the subscript will change depending upon the direction of propagation with reference to the crystallographic orientation. Hence, DOP_{110} and DOP_{001} correspond to the DOP of photoluminescence that is propagating along $[110]$ and $[001]$ directions respectively.

1.2 New Contributions

The DOP technique has been mainly used to measure the strain field in bulk semiconductors [31,32,33]. With the replacement of bulk materials by thin quantum wells in many optical and electronic devices it becomes imperative to understand the properties of quantum wells. Based on the previous experience with the measurements of DOP of luminescence, a natural question that emerged was, ‘Given the state of polarization of photoluminescence from the quantum wells, what can we say about the properties of quantum wells?’ Some of the answers to that question blossomed into the work reported in this thesis.

Single InP/InGaAs(P)/InP quantum wells were used throughout this work. A typical structure is shown in Fig. 1.5. The state of polarization of photoluminescence from (001) and (110) crystallographic orientations was studied to obtain quantitative information on the interfacial strain, thickness and biaxial strain in quantum wells. The results were compared with the results from other measurement techniques.

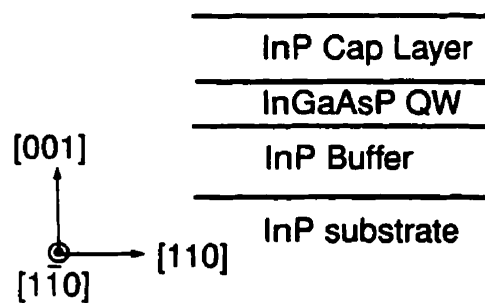


Figure 1.5 Typical material structure of the samples used in this work

Edge emissions from quantum wells are highly polarized and the state of polarization of photoluminescence depends on both the strain and thickness of the quantum well [35, 36]. This led us to ask whether it is possible to obtain information on strain and thickness of the quantum well by measuring the relative strength of TE (electric field in the plane of the layer) and TM (electric field perpendicular to the plane of the layer) polarized photoluminescence (DOP_{110}). Our measurements of DOP_{110} on InP/InGaAsP/InP single quantum wells, presented in chapter 3, show that DOP_{110} is a sensitive function of the strain and thickness of the quantum well [37]. It is also demonstrated that this technique is substantially faster, and at room temperature, more sensitive than the spectral technique.

Probing of heterostructure interfaces has been done using various characterization tools. In-situ techniques like Reflection High Energy Electron Diffraction (RHEED) [38], kinetic ellipsometry [39], and reflectance anisotropy spectroscopy [40,41,42,43], and ex-situ techniques such as low-temperature photoluminescence [44,45], optical absorption [46], Scanning Electron Microscopy [47], Transmission Electron Microscopy [48], Scanning Tunneling Microscopy [49], X-ray diffraction [28,50,51], and X-ray absorption [52] have been extensively used to study the interface. In this thesis, an anisotropic state of polarization of photoluminescence observed from the (001) surface of quantum wells has been correlated to the features at the heterostructure interfaces.

From considerations of symmetry, quantum wells grown on (001) oriented substrates

are not expected to show an anisotropy of polarization of luminescence in the in-plane of the quantum well (i.e., between $[110]$ and $[1\bar{1}0]$ directions). Polarization-resolved measurements from (001) surface of bulk InP material show a DOP_{001} of less than 0.2 percentage points. However, we have measured DOP_{001} upto 30 percentage points in thin ($<100\text{\AA}$) InP/InGaAs/InP quantum wells and found DOP_{001} to depend on the quantum well thickness, Ga composition, and gas switching times at the growth interrupted interface requiring an As to P flux change. The experimental results are presented in Chapter 4. This is an interesting result since anisotropy in the polarization of photoluminescence, to my knowledge, has not so far been observed in InP/InGaAs/InP quantum wells grown on planar substrates.

A linear relationship of DOP_{001} with the reciprocal of the thickness of the quantum well has been observed. This suggests that DOP_{001} may be mainly an interface phenomenon. Using a simple bond-counting model, we suggested that the DOP_{001} can be correlated to an effect of an anisotropic strain field that is associated with strained bonds at the interfaces of the quantum well [53,54]. However, this model could not predict the propagation of strain into the quantum well. Hence, we felt a need for a better model to understand the dependence of DOP_{001} on the thickness of the quantum well and is the model I discuss in chapter 5.

A numerical simulation based on valence force field model predicted a net anisotropic strain between $[110]$ and $[1\bar{1}0]$ directions in the quantum well due to strained bonds at the interfaces [55]. A small magnitude of shear strain (difference in the components

of strain between [100] and [010] directions) of the order of 10^{-4} in the quantum well was also predicted by the simulation. The results of the polarization-resolved photoluminescence measurements on shear strain are consistent with the predictions from the model.

Polarizing beam splitter (PBS) cubes have been successfully used to separate the two polarizations. In this thesis work, a rotating polarizer was used instead of a PBS which enabled us to measure simultaneously DOP and ROP and to calibrate the experimental apparatus to obtain information on both the difference in the principal components of strain and shear strain in the material [56]. We define ROP as

$$ROP = \frac{\int_0^{\infty} [L_{x'}(E) - L_{y'}(E)] R(E) dE}{\int_0^{\infty} [L_{x'}(E) + L_{y'}(E)] R(E) dE} \quad (1.2)$$

where $L_{x'}$ and $L_{y'}$ are the magnitudes of the luminescence polarized along x' and y' which are rotated by 45° with reference to (x, y) coordinate axes.

The thesis consists of 8 chapters including this introductory chapter. Chapter 2 describes the details of the experimental technique used for measuring DOP and ROP simultaneously. The relationships between DOP (ROP) and the difference in the strain components (shear strain) are also explained therein. The dependence of the state of polarization of photoluminescence on biaxial strain and thickness of the quantum well is dealt with in chapter 3. Probing of interfacial structures is discussed in chapters 4 and 5.

Chapter 4 focuses on the results related to the anisotropic interfacial strain. The details of the valence force field to explain the experimental results given in chapter 4 and the observations of shear strain in quantum wells are presented in chapter 5. Chapter 6 contains conclusions from this work and few suggestions for future research. The software written for computing DOP_{110} in chapter 3 and DOP_{001} using valence force field model are given in Appendix A and B respectively. The last chapter contains the bibliography.

In summary, InP/InGaAs(P)/InP quantum wells have been probed using polarization-resolved photoluminescence. Some of the important physical properties of the quantum wells such as biaxial strain, thickness of the quantum well, and interfacial features have been studied. This research has shed light on some of the novel features associated with quantum well interfaces. It is demonstrated that the measurements of DOP and ROP of photoluminescence that is propagating along various crystallographic orientations are useful for characterizing strained quantum wells. Part of the work described in this thesis has been published [37,54] or submitted for publication [55,56] in journal articles and presented in a conference [53].

Chapter 2. Experimental Methods

2.1 Introduction

The main technique that is implemented in this work for characterization of strained quantum well materials is room-temperature polarization-resolved photoluminescence. The important aspects of the experimental apparatus used to measure degree of polarization of photoluminescence (DOP) and rotated degree of polarization of photoluminescence (ROP) are discussed in this chapter. It is demonstrated that simultaneous measurement of both DOP and ROP enables one to obtain information on both the difference in the principal components of strain and shear strain in the material. The experimental apparatus has been calibrated for a known externally- applied load on an InP beam.

Some of the salient features related to the growth of InP-based compounds using gas source molecular beam epitaxy are also presented. These aspects of growth are the foundations for the analysis of experimental results given in Chapter IV.

2.2 Experimental Technique

The experimental apparatus used to measure DOP and ROP of photoluminescence is shown in Fig. 2.1a. The samples were excited by the output of a He-Ne laser that was

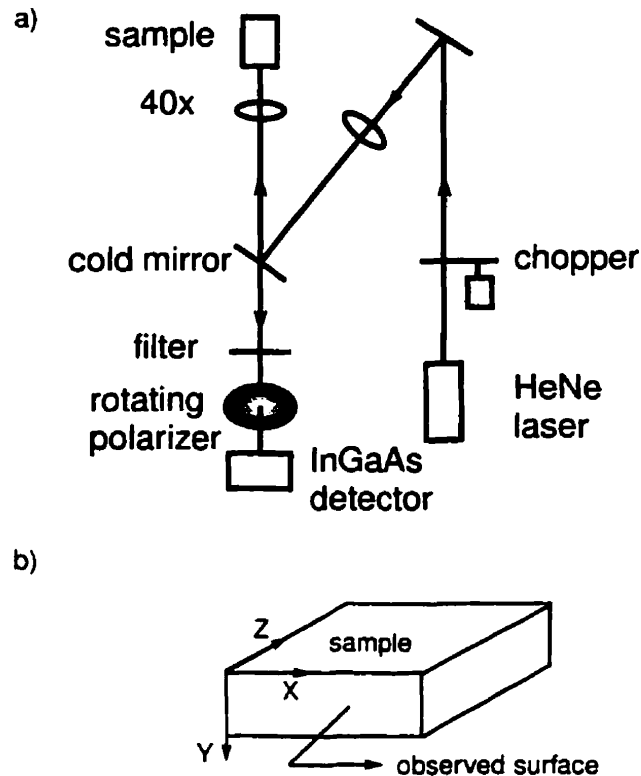


Figure 2.1 a) Experimental Apparatus, and b) Scanning directions

chopped at a frequency ω_c ($=2\pi \times 1010$ Hz). The luminescence from the samples was collected through a 40x microscope objective (Newport M-40X) in a confocal arrangement and then passed through a linear polarizer (Meadowlark Optics DP-050-HR) rotating at a frequency ω_m ($2\pi \times 200$ Hz) and a $200\mu\text{m}$ pin hole to an InGaAs detector. The samples were scanned past the measurement system under computer control using DC motor drives (Oriel Motor Mike). Electronic gauge units (Mitutoyo series 519 Mu-checker gauge heads) were used to determine the position. The accuracy of the measurement of position is $\approx 0.1 \mu\text{m}$ and the smallest step size used in the measurements was $0.2 \mu\text{m}$. The scanning directions are indicated in Fig.2.1b. The samples were scanned over the 'x' direction and then stepped in

the 'y' direction. At each scan point, the values of (L_x+L_y) , DOP and ROP were recorded, where L_x and L_y are the luminescence polarized along the x and y directions respectively.

A polarizer beam splitter cube can be used to separate L_x and L_y and measure simultaneously L_x and L_y using two photodiodes. However, the alignment of the two photodiodes is critical in order to image the same location on the surface of the material [57]. The rotating linear polarizer has three distinct advantages. i) Demodulation of the output of the photodiode, by phase sensitive detectors at the frequency of the chopper yields $(L_x + L_y)$ and at twice the rate of rotation of the polarizer gives $(L_x - L_y)$ and $(L_x \cdot - L_y)$, for the in-phase and quadrature components. ii) Measurement with a single detector helps to ensure measurement of L_x and L_y components of luminescence from the same location of the sample. iii) Measurements are wavelength independent over a wide range of λ (≈ 850 - 1800 nm)..

The chopped luminescence, in general, has a square wave form and considering the Fourier components, the signal at the detector, V_s , can be written as

$$V_s = \left[L_x \cos^2 \theta + L_y \sin^2 \theta \right] \left[\frac{1}{2} + \frac{2}{\pi} \sum_{n=0}^{\infty} \frac{\sin(2n+1)\omega_c t}{2n+1} \right] \quad (2.1)$$

where $(L_x \cos^2 \theta + L_y \sin^2 \theta)$ is the transmittance of the linear polarizer, $\theta = \omega_m t$ is the angle between the axis of polarization of the incident beam and the axis of preferred transmission of the polarizer and ω_m is the rate of rotation of the polarizer. Expanding Eq.2.1 yields

$$V_s = \frac{(L_x + L_y)}{2} \left[\frac{1}{2} + \frac{2}{\pi} \sum_{n=0}^{\infty} \frac{\sin(2n+1)\omega_c t}{2n+1} \right] + \frac{(L_x - L_y)}{2} \cos 2\omega_m t \left[\frac{1}{2} + \frac{2}{\pi} \sum_{n=0}^{\infty} \frac{\sin(2n+1)\omega_c t}{2n+1} \right] \quad (2.2)$$

Phase-sensitive detection of V_s at the chopper frequency and at twice the rate of rotation of the polarizer, for an in-phase operation, gives output signals that are proportional to $\langle L_x + L_y \rangle$ and $\langle L_x - L_y \rangle$ respectively where $\langle \rangle$ indicates a weighted time average. The measurement of the out-of-phase or quadrature component at $2\omega_m$ yields an output proportional to $\langle L_x - L_y \rangle$ where L_x and L_y are the magnitudes of the luminescence polarized along x' and y' which are rotated by 45° with reference to the (x,y) coordinate axes.

The lock-in amplifiers (phase sensitive detectors) used in this work are of a switched multiplier type [58]. The inputs to the lock-ins are amplified, multiplied effectively by a square wave, which has a 50% duty cycle and values of one or minus one, and low-pass filtered with two simple low-pass filters with time constants of 100 ms and 50 ms. Thus the dc component of the output of a lock-in for the input of a unit amplitude harmonic wave with the same phase and frequency as the square wave that is used to multiply the signal is $g/2$ where g is a gain factor. The dc component of the output of a lock-in for the input of a unit amplitude square wave with the same frequency and phase as the square wave that is used to perform the multiplication is g .

Three lock-in amplifiers are used to determine DOP and ROP. The outputs of the

lock-ins are digitized with a 12-bit analog-digital converter (ADC) and the ROP and DOP are calculated as the ratio of the means, which are based typically on 200 samples from the ADC, of the output of the appropriate lock-ins.

Owing to the finite bandwidth of the electronics and the non-zero width of the He-Ne beam, the chopped signal is not a perfect square wave and the output of the lock-in used to detect the signal at the chopper frequency is $< gA$ where A is the amplitude of the chopped signal. It is not difficult to account for the effect of the non-ideal shape of the chopped signal on the measurement of DOP and ROP. A polarizer with an extinction ratio $< 10^{-3}$ is inserted in the beam and the DOP and ROP measured. The measured value of the DOP is used to normalize the experimentally determined values since the DOP or ROP with the polarizer in place should be unity. The polarizer is also used to set the phase and x direction since the axis of transmission is known for the polarizer.

The output of the lock-ins are weighted time averages of the multiplication of the inputs to the lock-ins with square waves of unit amplitude and the desired frequency and phase. The time average is a convolution of the output of the multiplication with the unit area impulse response of the low-pass filters. The unit area impulse response h of two independent low-pass filters with RC time constants of τ_1 and τ_2 is

$$h = \frac{\exp(-t/\tau_2)}{\tau_2 - \tau_1} \left[1 - \exp -t \left(\frac{\tau_2 - \tau_1}{\tau_1 \tau_2} \right) \right] \quad (2.3)$$

Any signals with time variations faster than the RC time constants will be attenuated. The time average is exponentially weighted. Events that happened 5 RC time constants previous are weighted by about 0.05. This has bearing on the amount of time one must wait after changing gains, phases, or areas of observation on the surface of samples.

2.3 System Calibration

From previous calibration experiments using a simply-supported beam-bending technique [32], it has been shown that DOP is proportional to the difference in the components of strain along two orthogonal directions:

$$DOP = -C_{\epsilon} (\epsilon_x - \epsilon_y) \quad (2.4)$$

where ϵ_x and ϵ_y are the components of strain along 'x' and 'y' directions respectively. $C_{\epsilon} = 42.0 \pm 4.5$ is a calibration constant obtained from the polarization-resolved photoluminescence measurements performed in bulk InP material. In a similar way, ROP is related to the shear strain in the material [34] and is given by

$$ROP = 2C_{\gamma} \gamma_{xy} \quad (2.5)$$

where γ_{xy} is the shear strain between the planes 'xz' and 'yz' and C_{γ} is a calibration parameter.

The distributions of stress in the V-groove quantum wire structures have been studied using Raman, PL [59,60] and TEM [61] measurements and calculated using a Finite Element

method [61,62]. Apparently, the V-groove structures show a significant stress distribution at the bottom of the groove, due to biaxially strained epitaxial layers. Utilizing this feature of V-groove geometry, a known uniaxial load was applied to the V-groove and the distribution of DOP and ROP were measured in order to determine the calibration constants, C_ϵ and C_γ simultaneously.

2.3.1 Experimental Results

A bulk InP bar with etched V-grooves was used as a beam that is supported at two points 3 mm apart. The thickness and width of the bar are $200\ \mu\text{m}$ and $500\ \mu\text{m}$ respectively. The V-grooves are $4\ \mu\text{m}$ deep and $8\ \mu\text{m}$ wide. Since the grooves were $150\ \mu\text{m}$ apart, the interaction of the strain field due to nearest neighbour grooves was negligible. A known force was applied to the top surface of the sample using a spherically-tipped probe as shown in Fig. 2.3. The force was calibrated using a strain gauge attached to the probe [63].

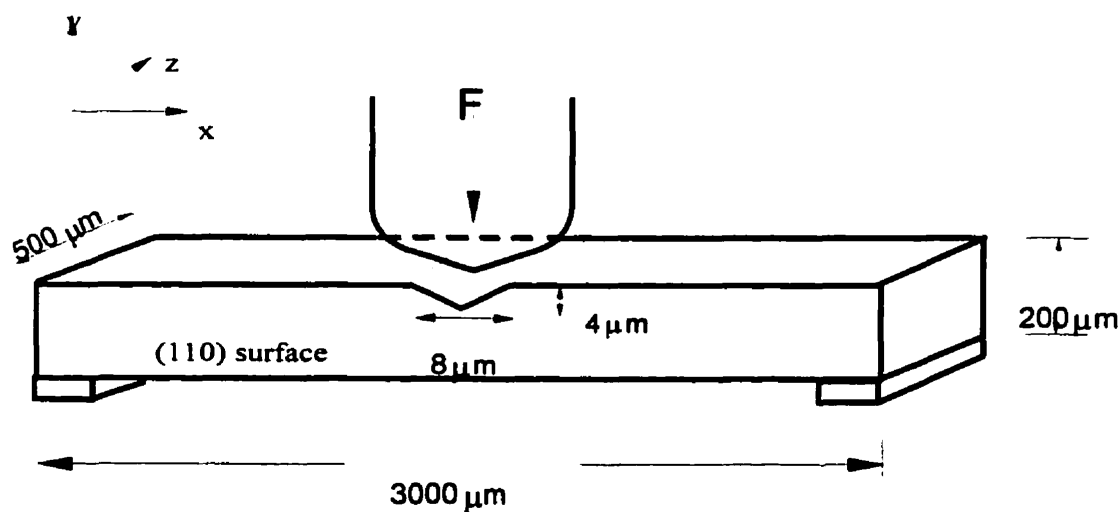


Figure 2.2 Schematic of the simply-supported beam-bending experiment

As it is well known [64], in a pure bending experiment, the applied force induces a bending stress in the bar creating a compressive stress on the top surface and tensile at the bottom surface of the sample. Fig. 2.3 shows an image of the distribution of DOP of the photoluminescence from the cleaved (110) surface for an applied load of 0.2N. The fringes represent lines of equal DOP and resemble fringes of the difference in the stress components of photoelastic measurements. The DOP fringe spacing, in the image, is 0.019. The scanned area was $100 \times 200 \mu\text{m}^2$ and the step size in the two directions were $1 \mu\text{m}$ and $2 \mu\text{m}$ respectively. In accordance with Eq. 5, the image shows a compressively-strained top surface with the strain of the order of $1.6 \times 10^{-3} \text{ dyn/cm}^2$. The rough bottom surface of the sample due to poor polishing is also seen in the figure.

Near the top surface, the region below the V-grooves showed characteristic distributions of DOP as well as ROP. A detailed scan was taken under the V-groove over an area of $60 \times 50 \mu\text{m}^2$ with a scan-step of $0.5 \mu\text{m}$. Fig. 2.4 shows the images of the distribution of DOP and ROP of the edge emission photoluminescence for four different applied forces. A) $F = 0$; B) $F = 0.047\text{N}$; C) $F = 0.21\text{N}$; and D) $F = -0.159\text{N}$. The color scheme used in the figure is as follows: Green corresponds to a reference offset value of DOP (ROP) marked in the figure; moving towards Blue refers to a positive value of DOP (ROP) and moving towards Red refers to a negative value of DOP (ROP) with reference to the offset. The offset values of DOP (ROP) were chosen to highlight the distribution of DOP (ROP) beneath the V-grooves compared to the distribution of DOP (ROP) due to bending of the simply-supported beam. This suggests, based on Eqs. 2.4 and 2.5, that the material beneath the

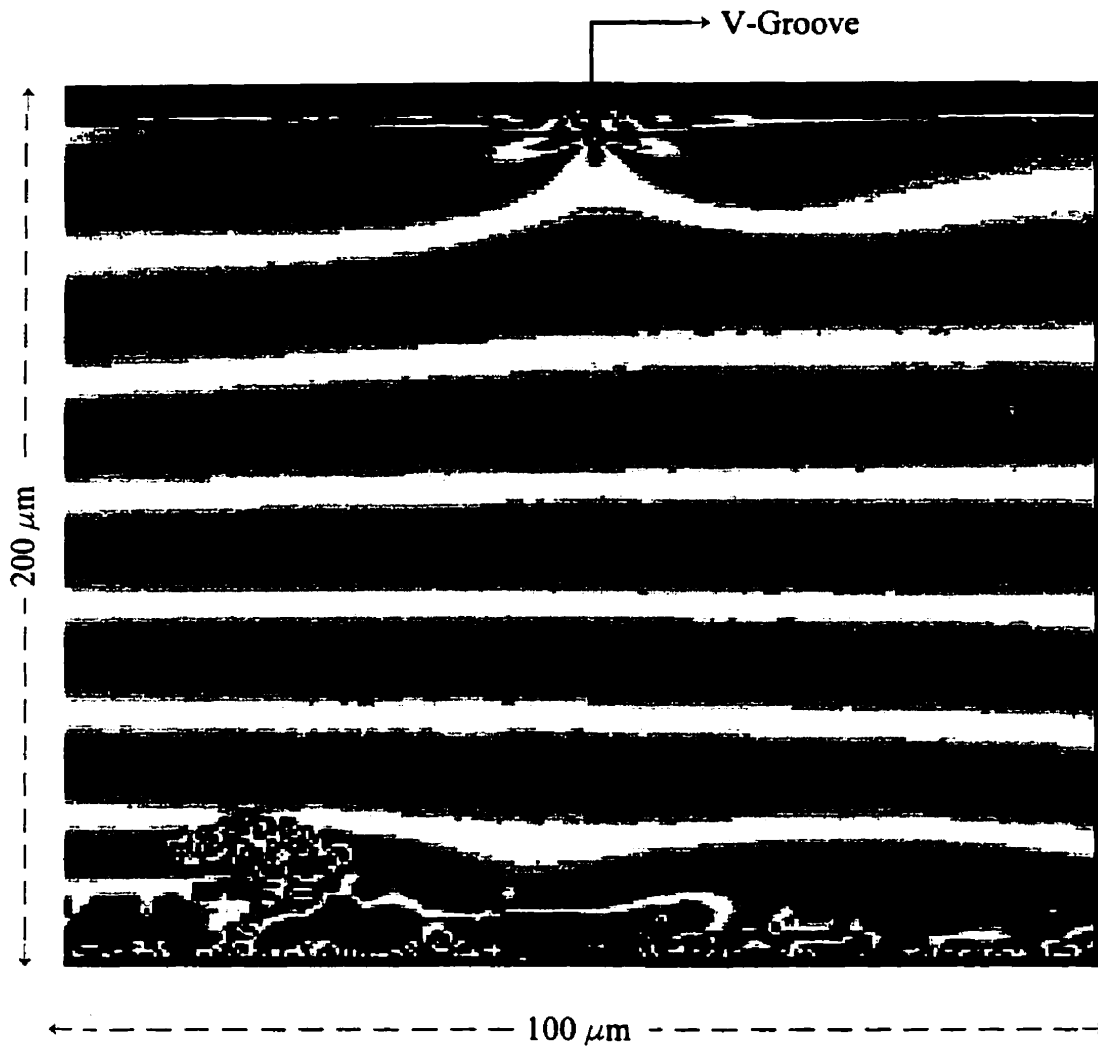


Figure 2.3 An image of the distribution of DOP for the V-groove structure for an external load of 0.2 N. The fringe spacing is .019.



groove has anisotropic normal components of strain and shearing strain and both increase with applied stress.

Having measured the distribution of DOP and ROP, the next task is to simulate the above experiment to determine the relationship between DOP (ROP) and the difference in the normal components of strain (shear strain).

2.3.2 Simulation Using ANSYS

The simply-supported beam-bending experiment was simulated using ANSYS, a software based on the finite-element method. ANSYS is a general purpose software that can be used to perform structural, mechanical, electromagnetic, thermal and fluid types of analysis. Various versions of this software are available. We have installed a University-version in a 133 MHz pentium machine with 32 MB RAM. The maximum number of elements and nodes that are available in this version are 8000 each.

PLANE42 element was chosen for the analysis. The geometry of the beam ($3000 \times 200 \mu\text{m}^2$) with a single V-groove of size $4 \mu\text{m}$ deep and $8 \mu\text{m}$ wide was constructed. The width of the beam ($= 500 \mu\text{m}$) is introduced in the form of 'Real Constant'. The displacements, in the 'y' direction, of the two end-points in the bottom surface of the structure were taken to be zero. Due to the symmetric nature of the structure, only half of the structure was modeled and the analysis extended to the other half. Symmetric boundary conditions were applied which will produce the same results as an analysis of the full model. This was

ensured by introducing displacement constraints along the 'x' direction at all nodes along the line 1. The load ($F = 0.105\text{N}$) was applied at the bottom of the groove. Fig. 2.5 shows the geometry used for the analysis.

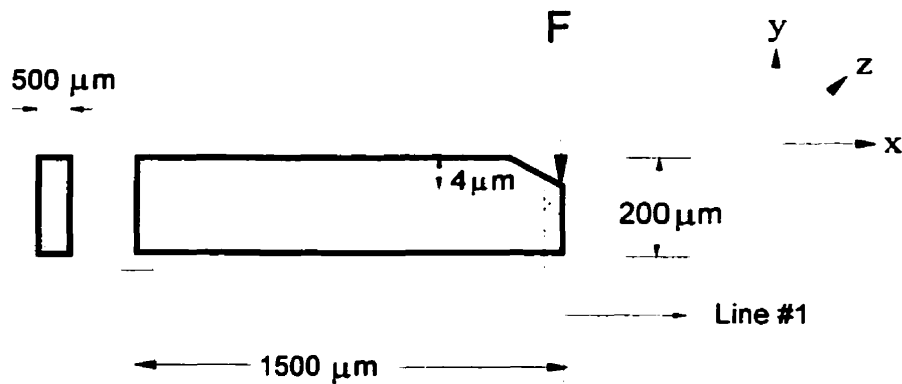
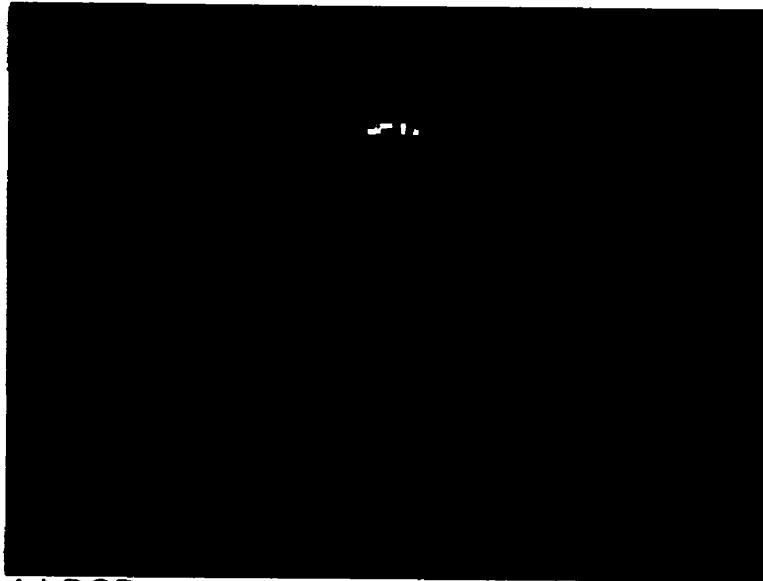


Figure 2.5 Schematic of the V-Groove geometry used in ANSYS. Δ represents the displacement constraint at that location.

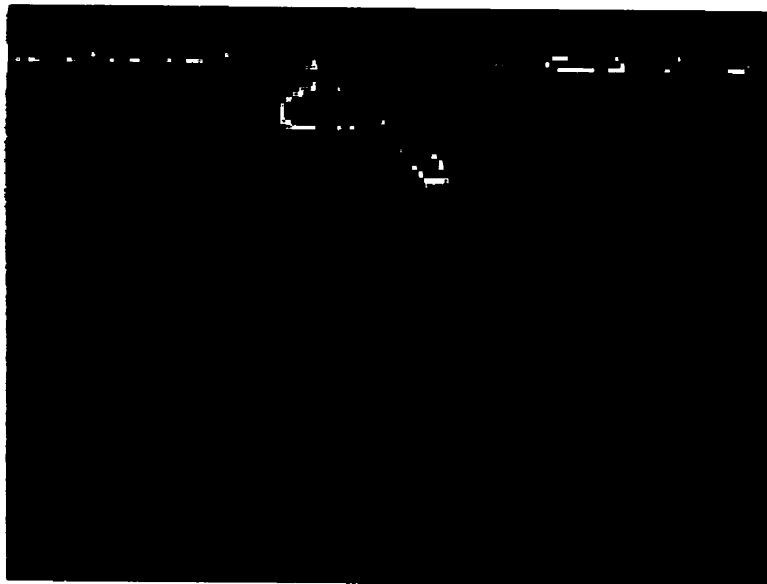
Young's Modulus (E) of $6.07 \times 10^{11} \text{ dyn/cm}^2$, and Poisson's ratio (ν) of 0.3575 were used corresponding to InP [65]. Static structural analysis was performed to calculate the elastic stress distribution.

Interpolating the results from ANSYS at experimental locations and least-square fitting to the experimental data of DOP and ROP yields the calibration constants $C_\epsilon = -37.9 \pm 1.7$ and $C_\gamma = -11.5 \pm 1.0$. Least-square fitting of the data from simulation was done over 10 different sections of the scanned area and the mean values of C_γ and C_ϵ were obtained.

EXPERIMENT

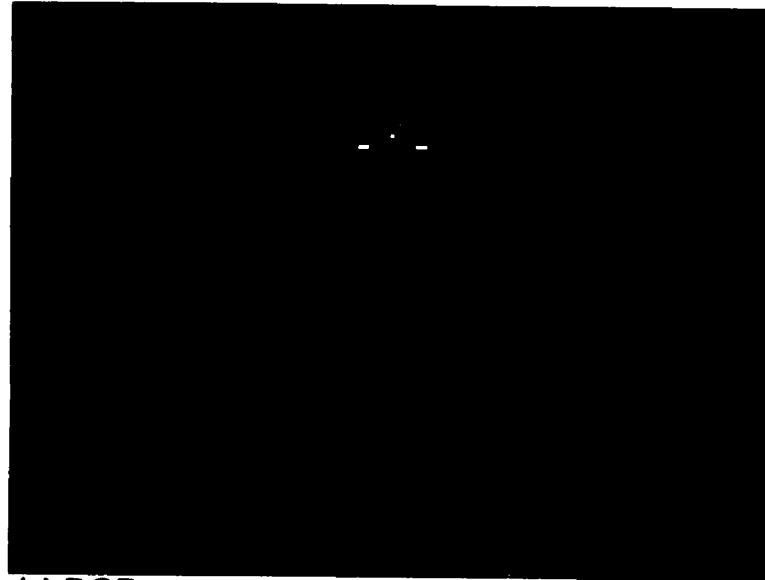


(a) DOP

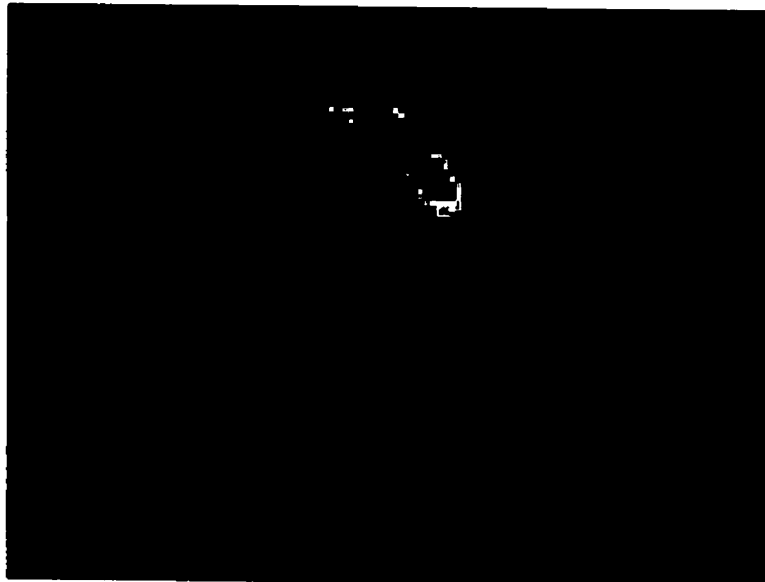


(b) ROP

SIMULATION



(c) DOP



(d) ROP

(e) color bar

Figure 2.6 Images of distributions of DOP and ROP of V-groove structures obtained from: (a) & (b) Experiment ; (c) & (d) Simulation using ANSYS.

deviation. The experimental uncertainty of a number T is reported in this thesis as $\pm \sigma$. Assuming normal statistics this gives a confidence level of 68%, i.e., it is expected that the true value for the quantity under measure is in the range of $T-\sigma$ to $T+\sigma$ 68% of the time. An uncertainty of $\pm 2\sigma$ yields a confidence interval of 95%. In most measurements the standard deviation was obtained from a large number of measurements and thus it is not necessary to employ a Student's T distribution. In calculating the uncertainty of the dependent variable in a least-squares fit to data it is necessary to include the correlation between the parameter.

Fig. 2.6 compares the experimental and simulated distributions of DOP and ROP. The calibration constants $C_\epsilon = -37.9$ and $C_\gamma = -11.5$ were used to plot the simulation results. The value of C_ϵ agrees reasonably within experimental uncertainty with the value 42.0 ± 4.5 obtained from the beam-bending experiment performed on bulk InP material without V-grooves.

It is evident that the simulation predicts a larger strain under the tip of the V-groove (approximately over a $2 \times 2 \mu\text{m}^2$ area). This may be due to two reasons: a) the applied force is not a concentrated load as was assumed in the simulation. The radius of curvature of the tip of the probe in the experiments is approximately $50 \mu\text{m}$; and b) Experimentally, the load is not applied precisely at $z=0$; but rather in the center of the beam as shown in Fig. 2.2. Hence, the effect due to the contact stresses may not be prominent in the measurements. Any effect due to the sharp geometry at the bottom of the groove was checked in ANSYS by flattening the bottom. Since the distributions of strain obtained from both situations were

similar, it is concluded that the large value of strain just below the groove is due to the contact stresses and not associated with the geometry of the structure.

The maximum shearing strain at the bottom of the groove is of the order of 7.4×10^{-4} when the external load is 0.21N. The calibration parameters, C_ϵ , C_γ will be used in chapter 4 and 5 to obtain the value of difference in the normal components of strain and shear strain in InP/InGaAs/InP quantum wells.

2.4 Growth Aspects

2.4.1 Gas Source Molecular Beam Epitaxy (GSMBE)

Molecular beam epitaxy (MBE) is an ultrahigh-vacuum technique for fabricating epitaxial layers by the reaction of one or more thermal beams of atoms or molecules with a heated crystalline surface [66]. The absence of gas phase interactions, the ability to start and stop a molecular beam in less than the time taken to grow a single atomic or molecular layer, and the use of substrate rotation have led to the ability to control precisely the thickness ($\pm 2.5\%$), composition ($\pm 2.5\%$) and uniformity ($\pm 1.5\%$) across the entire substrate. While MBE is suitable for the growth of As-based compounds, to achieve well-controlled phosphorous and arsenic beams, the elemental Group V sources were replaced by hydrides (AsH_3 and PH_3). The use of gas sources for group V in MBE has led to the name Gas Source Molecular Beam Epitaxy (GSMBE) [67,68].

The system at McMaster University is a GSMBE, mainly used for the growth of

GaAs and InP-based compounds, such as $\text{In}_{1-x}\text{Ga}_x\text{As}_y\text{P}_{1-y}$, $\text{In}_{1-x}\text{Ga}_x\text{As}$ on InP and InGaAs on GaAs. The ultimate base pressure of the growth chamber is $\sim 1 \times 10^{-10}$ Torr. The H_2 background pressure introduced during the growth raises the chamber pressure to $\sim 1 \times 10^{-5}$ Torr. The temperatures of the effusion cells are controlled within $\pm 0.5^\circ\text{C}$ using Eurotherm temperature controllers to control the composition of the layers to within $\pm 2.5\%$ points. The substrate temperature is monitored by a pyrometer. The chamber is also equipped with an in-situ Auger Electron Spectroscopy (AES) chamber where the epi-ready wafer is degassed at 350°C and with an Electron cyclotron resonance (ECR) plasma source to desorb the oxide from the substrate.

The $(100 \pm 0.06^\circ)$ -oriented substrates used in this work were obtained from 'Sumitomo Electric Industries'. The samples were normally of size $14 \times 14 \text{ mm}^2$. Typical growth temperature used in this study was 460°C and the substrates were rotated at 30 rpm to obtain uniform growth. Growth rates for InP were typically $1 \mu\text{m/hr}$ ($\sim 1 \text{ ML/s}$).

2.4.2 Surface Reconstruction

In general semiconductor surfaces either relax by bond rotation or reconstruct in order to minimize the surface energy due to unsatisfied dangling bonds. Since the (001) surface of zinc-blende structures (GaAs or InP) is polar, the surface can be terminated by a complete layer of either group III or group V atoms. The concentration of the surface atoms depends on the conditions of temperature and partial pressure of group III or group V molecules and hence a wide range of stoichiometry and structure can result. The surface-structure orientation

with respect to the underlying crystal bonds was first discussed by Cho [69] and he showed that the surface structure of GaAs can vary from As-stabilized GaAs(001)-c(2×8) to Ga-stabilized GaAs(001)-c(8×2) surfaces. The notation c(2×8) etc. is due to Wood [70]. In general, the surface reconstruction of III-V is represented as IIIV(hkl)-c(a×b)R<, where the (hkl) direction is normal to the surface, a and b indicate that the unit cell on the surface is a×b larger than that of the bulk crystal, and c indicates surfaces that are centered. If the structures are rotated with reference to the bulk, the amount of rotation is indicated by R<.

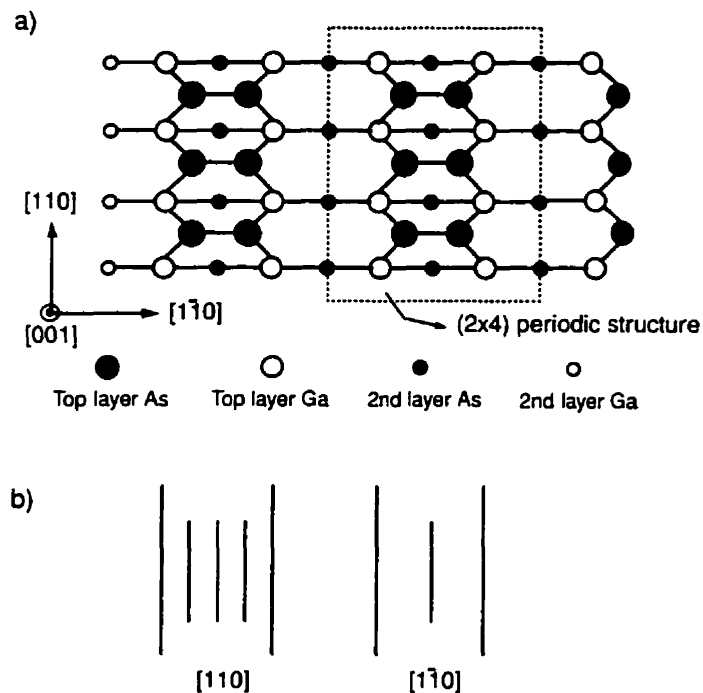


Figure 2.7 a) Ball-and-stick model of the GaAs(001)-(2×4) reconstructed surface with three dimer rows and one missing dimer row per unit cell.
b) Corresponding RHEED pattern viewed along [110] and [1 $\bar{1}$ 0] directions.

Under normal GSMBE growth conditions of GaAs, the surface results in an As-terminated

and (2×4) or $c(2 \times 8)$ reconstructed surface. The surface is thus believed to consist of a periodic pattern of three arsenic dimers and a missing dimer along the $[110]$ direction as shown in Fig. 2.7a. The surface structure is commonly studied using Reflection High Energy Electron Diffraction (RHEED). Fig. 2.7b shows the RHEED pattern corresponding to a As-stabilized, (2×4) reconstructed surface. Similar (2×4) -reconstructed surface has been observed during the growth of other III-V compounds, such as InP [71].

2.5. Summary

A technique for measuring the difference in the normal components of strain and shear strain in III-V compound semiconductor materials has been discussed in this chapter. A relationship between DOP and the difference in the normal components of strain and between ROP and shear strain have been established. The calibration constants, C_ϵ , C_γ , describing the two relationships have been obtained simultaneously by fitting the experimental distributions of DOP and ROP to finite-element simulations. These calibration constants will be used in chapters 4 and 5 to compute strain components that may be present in the material.

Chapter 3. Degree of polarization of luminescence from the facet

3.1 Introduction

The edge emission from quantum wells is highly polarized. The state of polarization of edge emission from quantum wells depends on both the strain and thickness of the well. Thus, by measuring the relative strength of TE (electric field in the plane of the layer) and TM (electric field perpendicular to the plane of the layer) polarized edge emission from the well, it is possible to obtain information on the strain and thickness of the well. We define edge emission to be photoluminescence from a cleaved (110) surface perpendicular to the plane (001) of the quantum well.

Two ways of performing polarization-resolved measurements are by 1) spectrally-resolved, and 2) room temperature (RT) integrated luminescence. The first method has been employed by many groups [72-78] in recent years to obtain the value of the strain in either bulk or large period superlattices with *a priori* knowledge of the thickness of the layers. The second technique, an integrated luminescence measurement at room temperature, is faster and gives a more sensitive measure of strain than the spectrally-resolved measurements.

The degree of polarization of the edge emission luminescence, DOP_{110} , we define as

$$DOP_{110} = \frac{\int_0^{\infty} [L_{TE}(E) - L_{TM}(E)] R(E) dE}{\int_0^{\infty} [L_{TE}(E) + L_{TM}(E)] R(E) dE} \quad (3.1)$$

where $\int [L_{TE}(E) + L_{TM}(E)] R(E) dE$ and $\int [L_{TE}(E) - L_{TM}(E)] R(E) dE$ are the sum and difference of the intensities of the TE (directed along $[1\bar{1}0]$) and TM (directed along $[001]$) polarized luminescence from the quantum well, integrated over all energy transitions. $R(E)$ is the responsivity of the detector. The magnitude of the DOP_{110} is a direct indication of the state of polarization of the luminescence from the quantum wells.

In this chapter, it is demonstrated that the DOP_{110} of the edge emission from InGaAsP single quantum wells provides information on the thickness and strain in the wells. When the composition of the alloy and the strain of the layers are maintained constant, it is shown that the DOP_{110} of the edge emission is a strong function of the thickness of the quantum well. Similarly, for a given thickness of the well, the DOP_{110} of the edge emission is a sensitive measure of the strain in the well. The results of the room-temperature DOP_{110} measurements on InGaAsP single quantum wells of various combinations of thickness and strain and on a multilayered structure are also presented. Finally, the DOP_{110} results are compared with polarization-resolved and spectrally-resolved measurements of the luminescence.

3.2 Experimental details

To understand the relationship between polarization-resolved measurements (DOP_{110})

and the quantum well parameters (strain and thickness), a study was done on two sets of samples. The samples were grown by gas-source molecular beam epitaxy. Twelve samples, referred to as sample Set I, were grown with single quantum wells of thicknesses 30, 50, 100 and 300Å and strains of 1% compression, lattice-matched, and 1% tension. A typical structure for sample Set I is shown in Fig. 3.1.

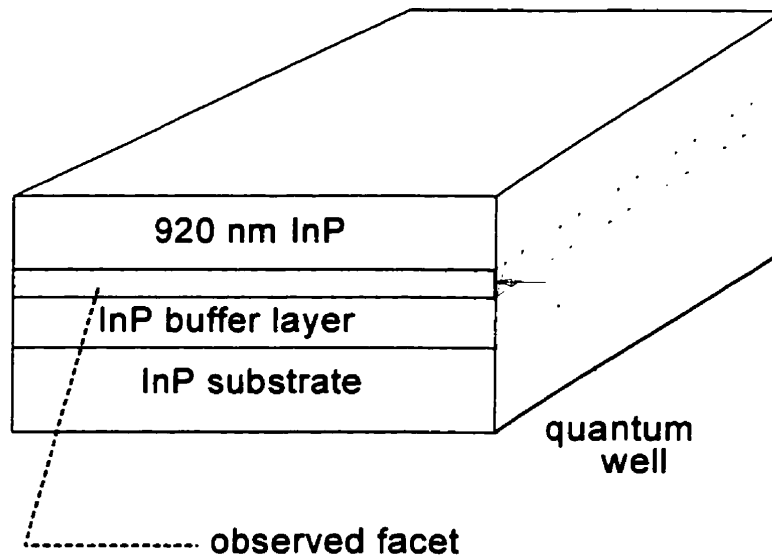


Figure 3.1 A typical material structure of sample Set I

A 0.92 μm thick InP layer was grown above the quantum well to minimize the effect of the (001) surface on the measurement of the DOP of the edge emission [79]. The compositions of the quaternary layers were chosen to give a bulk bandgap of 1.55 μm . Double crystal x-ray diffraction measurements gave the value of strain in the 300Å layers to be -1.1 % for a layer under compression and 0.95% for a layer under tension. It was not possible to measure strain

in the thinner samples using double crystal x-ray diffraction. Since all twelve samples of Set I were grown under similar growth conditions, it is assumed that the thinner samples are strained by the same amount as the 300Å layers.

In the second type of sample (referred to as Set II), a continuous variation of composition across the sample was obtained by not rotating the sample during growth. The sample structure, shown in Figure 3.2a, consists of three InGaAsP quaternary layers (with a nominal, lattice-matched, bulk bandgap of 1.28 μm wavelength) of thicknesses 50, 100 and 500Å, each separated by a 1 μm thick InP spacer layer. Double crystal x-ray diffraction measurements from the 500 Å layer indicate that the material at location 'B' is under less compression than the material at location 'A' (marked in Figure 3.2b). The variation of strain across the sample from 'A' to 'B' is approximately 8.5×10^{-4} for the 500Å layer. The variation of strain across the sample is attributed to a spatial variation of the ratio of the two group III elements which originate from separate effusion cells. The group V elements originate from a single cracker cell with dual input and therefore are not expected to contribute significantly to the spatial variation in composition.

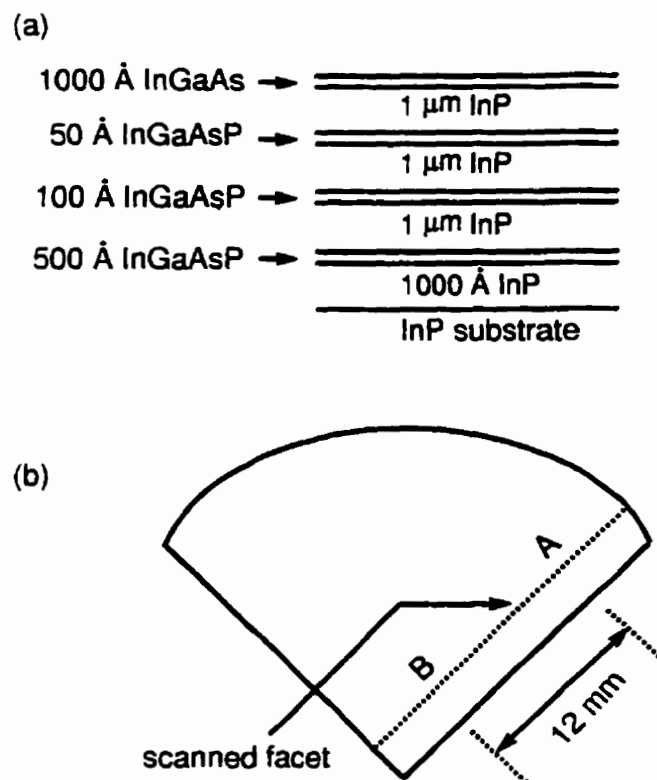


Figure 3.2 (a) The material structure of sample Set II. (b) Top view of the sample

The details of the experimental apparatus used to measure the DOP_{110} are given in chapter 2. The apparatus was extended to perform polarization-resolved spectral measurements using a DIGIKROM 240 monochromator from CVI corporation and the apparatus is shown in Fig. 3.3. A $1.0 \mu\text{m}$ long-pass filter was used to block the luminescence from InP. The sample of Set II was scanned across the facet along the growth direction to resolve spatially the quantum wells. The smallest step size used in these measurements was $0.2 \mu\text{m}$. At each scan point, the values of $\int [L_{TE}(E) + L_{TM}(E)] R(E) dE$, $\int [L_{TE}(E) - L_{TM}(E)] R(E) dE$

(E)]R(E)dE, and DOP_{110} were recorded.

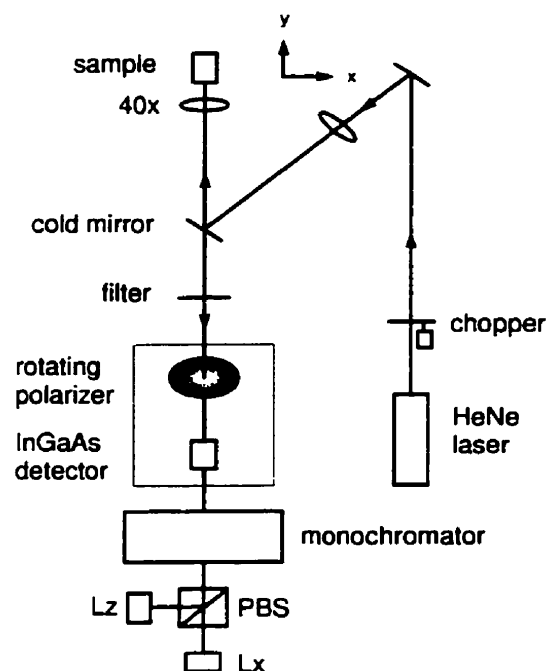


Figure 3.3 Experimental apparatus to perform polarization-resolved integrated photoluminescence and spectrally-resolved photoluminescence measurements.

3.3 Results of DOP_{110} measurements

a) Sample set I

Figure 3.4 shows a plot of the measured DOP_{110} versus thickness for the nominally 1% compressive, lattice matched, and 1% tensile strained wells of sample Set I. The data indicate that the DOP_{110} decreases with an increase in thickness of the well and that the DOP_{110} decreases as the strain varies from compression to tension. For a lattice-matched

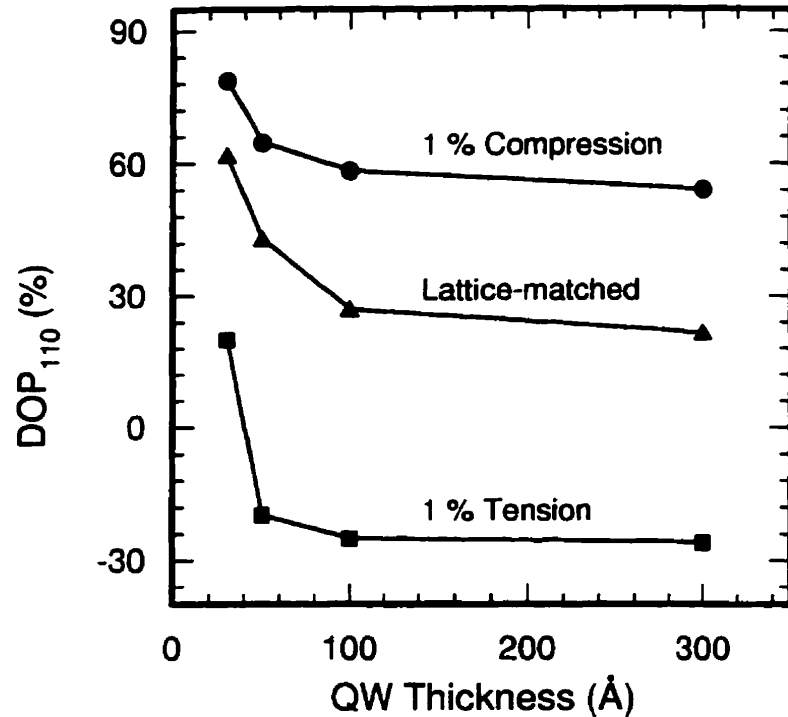


Figure 3.4 Measured DOP_{110} on sample Set I. The variation of DOP_{110} with quantum well thickness for three different strain conditions is shown.

case, a linear fit of $1/L_z$ to the data gives a relationship between the DOP_{110} and the thickness of the well (L_z) as

$$DOP_{110} \approx 12.5 + 1490/L_z .$$

From the above equation, a slope ($\Delta DOP_{110}/\Delta L_z$) of -0.60 ± 0.05 ($\% / \text{\AA}$) at 50\AA is obtained which is greater than the rms noise (± 0.2 percentage points) of the system. The variation in the measured DOP_{110} over a 1 cm, nominally uniform sample, is within ± 0.75 percentage points. These results suggest that from a measurement of DOP_{110} on quantum wells of

thicknesses less than 100\AA , it is possible to distinguish a small difference in thickness at a given strain.

The variation in DOP_{110} on a 50\AA thick sample is about 70 percentage points as the strain varies from approximately 1% compression to 1% tension. This suggests that from a measurement of DOP_{110} it is possible to distinguish a small difference in strain at a given thickness.

b) Sample Set II

Typical plots of the edge emission luminescence and the DOP_{110} of the photoluminescence scans across the wells in the 'xz' plane on the sample of Set II are shown in Figures 3.5a and 3.5b. The layers of thicknesses 50, 100 and 500\AA are marked in the figure. Assuming that the photoluminescence intensity distribution from each layer is Gaussian in shape, a nonlinear fit of the experimental data gives the FWHM of the luminescence of $0.98\ \mu\text{m}$, a value that is close to the diffraction limit [80]. Since the main interest was in the trend of DOP_{110} with thickness and strain, the effect on the DOP_{110} of one layer due to the small amount of emission captured from the adjacent layers was not removed. The effect of the luminescence from the 100 and 500\AA layers on the value of DOP_{110} of 33% for a 50\AA layer was calculated to be less than 3 percentage points. This suggests that the perturbation on the DOP_{110} of one layer due to the presence of the neighbouring layers can, to the first order, be neglected. The plateaus in the DOP_{110} in Fig. 3.5b show that it is possible to find regions dominated by each well. The InGaAs cap layer

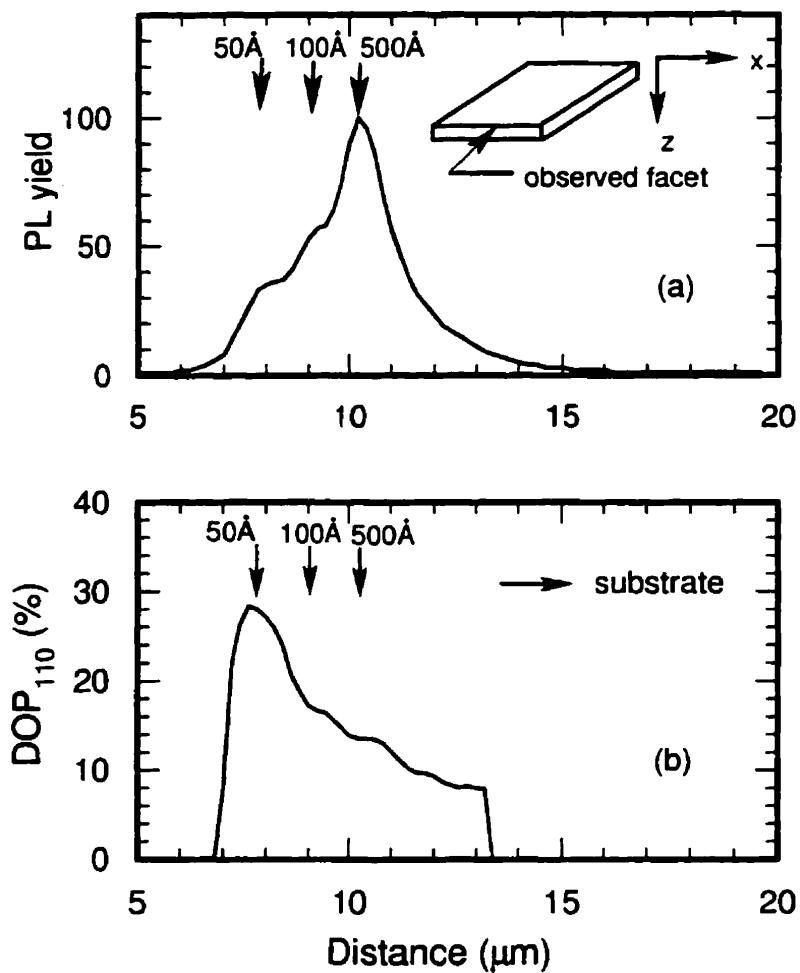


Figure 3.5 (a) Illustration of a scan across the facet of sample Set II along the z direction. The three layers of thickness 500, 100, and 50 \AA are spatially resolved and are indicated in the figure. Also shown is the direction of the scan in the inset. (b) Illustration of DOP across the facet. The locations of the three layers are indicated.

is out of focus due to the chromatic aberration in the microscope objective and a weak PL signal is observed from this layer compared to the quaternary layers. Most of the luminescence from InP is filtered out by a $1.0\mu\text{m}$ long pass filter. Hence, the effect on the DOP_{110} of the quaternary layers due to the presence of the InGaAs and InP layers is negligible.

The DOP_{110} measured across the sample of Set II is plotted in Figure 3.6a as a function of the distance between locations 'A' and 'B' (shown in Figure 3.2b). From X-ray data on the 500\AA thick layer, location 'A' is more compressive than location 'B' and the estimated strain variation across the sample is about 8.5×10^{-4} . For each layer, the DOP_{110} at 'A' is higher than the DOP_{110} at 'B' by about 5 percentage points. This difference in DOP_{110} can be attributed to variation in thickness and composition (i.e., strain and bandgap). From the linear fit of the data, the slopes ($\Delta\text{DOP}_{110}/\Delta\text{distance}$) for the 500, 100, and 50\AA layers are found to be $-0.43 \pm .03$, -0.54 ± 0.03 , and -0.77 ± 0.04 percentage points/mm respectively. As it was observed in sample Set I, the change in DOP_{110} due to a change in thickness is small for layers of $L_z > 100\text{\AA}$. Hence, the change in DOP_{110} from 'A' to 'B' in the 500\AA layer can be attributed mainly to a change in strain. This indicates that larger DOP_{110} corresponds to larger compressive strain (or reduced tensile strain). This variation in DOP_{110} from 'A' to 'B' is consistent with the change in strain measured using double crystal x-ray diffraction and the trend observed in sample Set I. It is interesting to note that the slopes of the lines shown in figure 3.6a are not the same to within experimental uncertainty. For thin layers the DOP_{110} is a strong function of the thickness of the layer and the simulation (discussed in section IV)

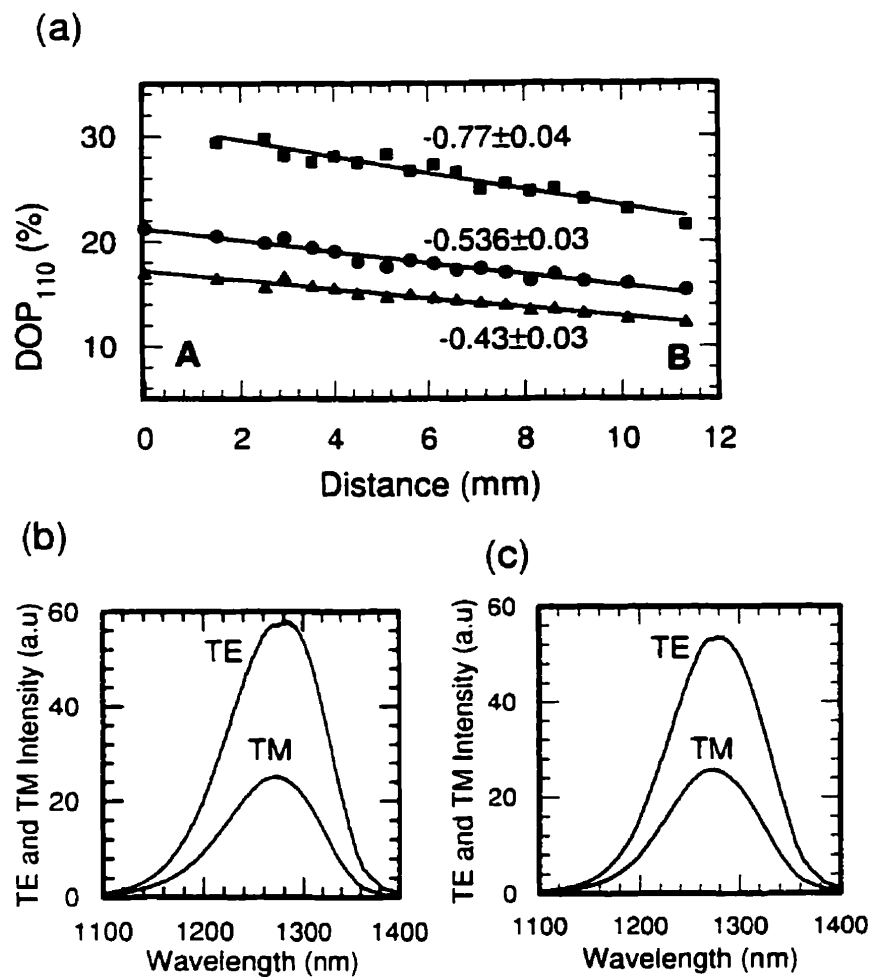


Figure 3.6 (a) Measured DOP_{110} on sample Set II as the sample is scanned across the facet from location A to B. The slopes of the lines are indicated in the figure. (b) The room-temperature photoluminescence spectra at location A. (c) The room-temperature photoluminescence spectra at location B.

suggests that changes of both thickness and composition play a role in the variation of DOP_{110} . This may explain the different slopes for the layers.

Shown in Figures 3.6b and 3.6c is the spectrally resolved and polarization-resolved luminescence taken at locations 'A' and 'B' for the 500Å thick layer. It is obvious that the shifts in the TE and TM peak wavelengths between 'A' and 'B' are very small and difficult to measure at room-temperature. However, the change in DOP_{110} (≥ 5 percentage points) is obvious. This demonstrates the sensitivity of the DOP_{110} technique to small changes in thickness and composition.

The trend of DOP_{110} with thickness is also confirmed in the sample of Set II. As seen in Fig. 3.4a, DOP_{110} increases with a decrease in the thickness of the layer at any location, similar to the observations made in sample Set I. The following section gives a brief explanation for the observed polarization of the edge emission of strained quantum wells.

3.4 Discussion

Some of the salient features related to the polarization properties of luminescence from quantum wells are discussed in this section. The Fortran code given in Appendix A computes the localized energy levels in quantum wells, in-plane band dispersion, and the degree of polarization of photoluminescence. The details of the derivation are given in many published articles [35,36,81,82,83,84,85,86,87,88,89] and text books by Bastard [90],

Chuang [91], and P. Zory [92].

The magnitude of the intensity of photoluminescence emitted from semiconductor materials due to the interaction of photons with electrons in the crystal depends on three important terms.

Term 1: Probability that an optical transition occurs from an initial energy state (conduction band) to a final energy state (valence band) at any given time

Term 2: Density of initial and final states

Term 3: Probability of simultaneously having the initial state filled and the final state empty

Term 1 gives the transition probability per unit time, W_{e-h} , that an electron, under the influence of an electromagnetic perturbation, makes a transition from the state $|\psi_e\rangle$ to the state $|\psi_h\rangle$.

$$W_{e-h} = \frac{2\pi}{\hbar} \frac{e^2 A_0^2}{m_0^2} |\langle \psi_h | \hat{\mathbf{e}} \cdot \hat{\mathbf{p}} | \psi_e \rangle|^2 \delta(E_e - E_h - \hbar\omega) \quad (3.2)$$

where A_0 is the magnitude of the vector potential \mathbf{A} ; $\hat{\mathbf{e}}$ is the unit polarization vector in the direction of the optical field; and $\hat{\mathbf{p}}$ is the momentum operator; m_0 is the free electron mass; e is the charge of an electron; E_e , E_h are the energies of an electron in the initial and final state respectively and $\hbar\omega$ is the energy of the photon. The delta function enforces energy conservation. $|\langle \psi_h | \hat{\mathbf{e}} \cdot \hat{\mathbf{p}} | \psi_e \rangle|^2 = |M_T|^2$ is known as the transition matrix element and is sensitive to the overlap of the wavefunction in the two bands and the state of

polarization of the optical field.

The transition rate given in Eq.1 corresponds to a single pair of electron and hole states in the conduction and valence band. The total transition rate can be obtained by summing over all possible states in the two bands (Term 2). Since the allowed transitions require momentum to be conserved, a reduced density of states can be used. For quantum wells and for parabolic energy bands, the reduced density of states can be given by

$$\rho_{red}(E) = \frac{m_r}{\pi \hbar^2 L_z} \sum_n Y(E_{en} - E_{hn} - E_{gn}) \quad (3.3)$$

where $Y(E_{en}-E_{hn}-E_g)$ is the unit step function; n refers to the subband index and E_{gn} is the bandgap between two given subbands; L_z is the thickness of the quantum well; and m_r is the reduced effective mass and is given by

$$\frac{1}{m_r} = \frac{1}{m_c} + \frac{1}{m_v} \quad (3.4)$$

m_c , m_v are the effective masses of the carriers in the conduction band and valence band respectively.

When the levels are partially filled (empty), it is necessary to take into consideration the probability of occupation of a given energy level which is given by the Fermi-Dirac distribution:

$$f_{c,v} = \frac{1}{1 + \exp[(E_{e,h} - E_{f(c,v)})/k_B T]} \quad (3.5)$$

where E_{fc} , E_{fv} are the quasi Fermi levels in the conduction and valence bands respectively.

The total transition rate can now be written as

$$W_{e-h} = \frac{2\pi}{\hbar} \frac{e^2 A_0^2}{m_0^2} |M_T|^2 \rho_{red} f_c (1 - f_v) \quad (3.6)$$

Hence, the total number of transitions per unit time depends on the three terms defined in Eqs. 3.2, 3.3, and 3.5. However, the transition matrix elements determine the polarization properties of luminescence. The polarization dependence of the transition matrix element may be understood by examining the details of the electron wavefunctions in the conduction and valence band.

Under an envelope function approximation [93,94], the localized wavefunction of an electron in the quantum well can be expanded on the periodic parts of the Bloch functions of the band edges and is given by the sum of the product of a rapidly varying Bloch functions, which have the periodicity as the lattice, and the slowly varying envelope function,

$F(\mathbf{r})$:

$$\Psi_{v,n}(\vec{r}) = \sum_l u_v^l(\vec{r}) F_{v,n}^l(\vec{r}) \quad (3.7)$$

$$F_{v,n}^l(\vec{r}) = \exp(i\vec{k}_{1,n} \cdot \vec{r}_{1,n}) \chi_{v,n}^l(\vec{z}) \quad (3.8)$$

where ν refers to conduction or valence band and n is the index of the quantum well-subband. The summation l runs over the number of band edges taken into account for the calculation. For example, $l=2$ for conduction band and $l=4$ corresponding to heavy and light hole valence bands. $u_\nu(\mathbf{r})$ is the Bloch wavefunction in the band ν and $\chi_{\nu,n}(\mathbf{z})$ is the envelope function that describes the z motion of the electron in the band ν corresponding to the l^{th} band edge and that satisfies the effective mass equation; $\mathbf{k}_l = (k_x, k_y)$; and $\mathbf{r}_l = (x, y)$.

The matrix element can be written as

$$\begin{aligned} |M_T|^2 &= \int_V \Psi_{h,n}^* \hat{\mathbf{e}} \cdot \bar{\mathbf{p}} \Psi_{e,n} d^3r = \int_V F_{h,n}^* u_\nu^* \hat{\mathbf{e}} \cdot \bar{\mathbf{p}} F_{e,n} u_c d^3r \\ &= \int_V [F_{h,n}^* F_{e,n}] u_\nu^* \hat{\mathbf{e}} \cdot \bar{\mathbf{p}} u_c d^3r + \int_V [u_\nu^* u_c] F_{h,n}^* \hat{\mathbf{e}} \cdot \bar{\mathbf{p}} F_{e,n} d^3r \end{aligned} \quad (3.9)$$

Due to orthogonality of u_c and u_ν , the second term vanishes.

$$|M_T|^2 = |\langle F_{h,n} | F_{e,n} \rangle|^2 |\langle u_\nu | \hat{\mathbf{e}} \cdot \bar{\mathbf{p}} | u_c \rangle|^2$$

The selection rules for the allowed optical transitions can be defined from the above equation.

1) the overlap integral between envelope functions selects the quantum numbers of the initial and final subbands.

$$|\langle F_{h,n} | F_{e,n} \rangle|^2 = |\langle \chi_{h,n} | \chi_{e,n} \rangle|^2 \delta(k_{1,h} - k_{1,e})$$

The delta function indicates that in order for a transition to occur, the in-plane momentum has to be conserved which is also known as the k -conservation or k -selection

rule. This arises due to the translational invariance in the in-plane of the quantum well. The envelope functions for an infinite-barrier quantum wells, are independent of the effective masses and they form an orthonormal set of functions. Hence, $|\langle F_{h,n} | F_{e,n} \rangle|^2 = 1$ when the quantum numbers (subband index) of the initial and final states are same, i.e., $\Delta n = 0$. However, in finite barrier quantum wells the wavefunctions of the carriers penetrate the barrier and the depth of penetration depends on the effective mass of the carrier. Hence the envelope functions of electrons in the conduction band and holes in the valence band are no longer identical for the same subband number and the functions are not perfectly orthonormal to each other. This leads to $|\langle F_{h,n} | F_{e,n} \rangle|^2 \neq 1$ and the possibility of forbidden transitions (i.e. $\Delta n \neq 0$). Another important phenomenon that affects the overlap integral between envelope functions arises due to mixing of the heavy hole and light hole bands for $k_{\parallel} \neq 0$. When the heavy hole and light hole energy levels decouple due to quantum confinement or strain, under a zeroth order approximation, the heavy hole and light hole bands cross each other. This is due to the fact that the heavy hole effective mass is heavy along \hat{z} and light in the in-plane of the quantum well. Similarly, the effective mass of light hole is light along \hat{z} and heavy in the in-plane of the quantum well. Hence, as we move away from the band edge, $k_{\parallel} \neq 0$, the concept of heavy and light hole vanishes and the wavefunction has both light and heavy hole character.

2) the atomic-like dipole matrix element, $|\langle u_v | \hat{\mathbf{e}} \cdot \hat{\mathbf{p}} | u_c \rangle|^2$, gives rise to the selection rules on the state of polarization of the light wave.

In III-V compounds, the eight outermost electrons (3 electrons from group III atoms and 5 electrons from group V atom) hybridize to form tetrahedral bonds. The s and p orbitals of each atom hybridize with s and p orbitals of four neighbouring atoms resulting in bonding and antibonding bands. The bonding s levels having the lowest energy are bound to the nucleus (localized) and the three bonding p orbitals which are filled by 6 electrons form the valence band. The antibonding s band forms the lowest lying conduction band. At the point of high symmetry, the conduction band edge retains the symmetry property as that of the s-atomic orbitals and the valence band edge retains the symmetry property as that of p-atomic orbitals. Let the Bloch functions of the s,x,y, and z atomic orbitals be given by $|S\rangle$, $|X\rangle$, $|Y\rangle$, and $|Z\rangle$. Some of the symmetry relations follow from the symmetry of the atomic orbitals.

$$\langle S|p_x|X\rangle = \langle S|p_y|Y\rangle = \langle S|p_z|Z\rangle = M \quad \text{and} \quad \langle S|p_\alpha|\beta\rangle = 0, \quad \text{for } \alpha \neq \beta$$

where $\alpha, \beta = X, Y, Z$. M is the momentum matrix parameter. From the cyclotron measurements of the effective masses of the carriers, the magnitude of M can be estimated. The basis functions for the conduction and valence band Bloch functions can be obtained from the linear combination of the states corresponding to s,x,y,z atomic orbitals. The valence band basis functions are taken from the spherical harmonics for the p-state wave functions of a hydrogen atom. In the angular momentum representation, it is convenient to write the conduction and valence band basis functions for the electron wave vector, \mathbf{k} , in the 'z' direction and $k_x = k_y = 0$. However if \mathbf{k} is in an arbitrary direction, as shown in Fig. 3-7, the basis functions can be found by coordinate transformation. The electron \mathbf{k} vector in an

arbitrary direction can be written in polar coordinates as

$$\vec{k} = k \sin\theta \cos\phi \hat{x} + k \sin\theta \sin\phi \hat{y} + k \cos\theta \hat{z}$$

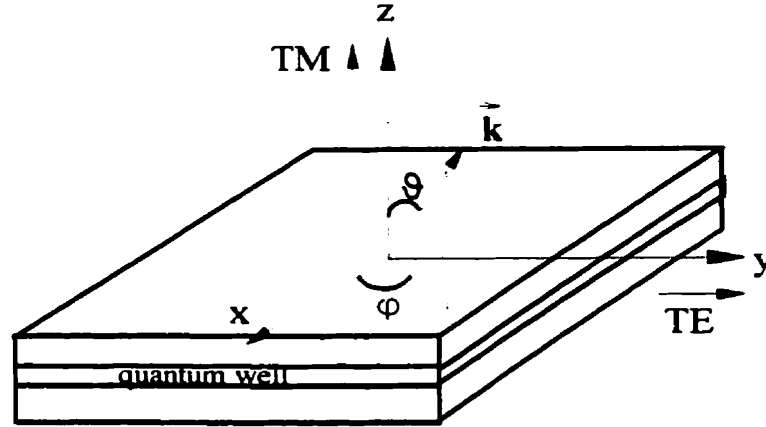


Figure 3.7 Coordinate system used in the discussion for the quantum well structure.

The conduction and valence band edge Bloch functions for spin-up and spin-down states are then given by

Conduction band $|u_c \uparrow\rangle$ and $|u_c \downarrow\rangle$

$$|iS \downarrow\rangle \text{ and } |iS \uparrow\rangle$$

Heavy hole band $|u_{hh} \uparrow\rangle$ and $|u_{hh} \downarrow\rangle$

$$\frac{-1}{\sqrt{2}} |(\cos\theta \cos\phi - i \sin\phi)X + (\cos\theta \sin\phi + i \cos\phi)Y - \sin\theta Z\rangle |\uparrow\rangle \quad \text{and} \quad \frac{-1}{\sqrt{2}} |(\cos\theta \cos\phi + i \sin\phi)X + (\cos\theta \sin\phi - i \cos\phi)Y - \sin\theta Z\rangle |\downarrow\rangle$$

Light hole band $|u_{lh \uparrow}\rangle$ and $|u_{lh \downarrow}\rangle$

$$-\frac{1}{\sqrt{6}} |(\cos\theta \cos\phi - i \sin\phi)X + (\cos\theta \sin\phi + i \cos\phi)Y - \sin\theta Z\rangle | \downarrow \rangle + \sqrt{\frac{2}{3}} | \sin\theta \cos\phi X + \sin\theta \sin\phi Y + \cos\theta Z \rangle | \uparrow \rangle$$

and

$$\frac{1}{\sqrt{6}} |(\cos\theta \cos\phi + i \sin\phi)X + (\cos\theta \sin\phi - i \cos\phi)Y - \sin\theta Z\rangle | \downarrow \rangle + \sqrt{\frac{2}{3}} | \sin\theta \cos\phi X + \sin\theta \sin\phi Y + \cos\theta Z \rangle | \uparrow \rangle$$

$| \uparrow \rangle$ and $| \downarrow \rangle$ refer to spin-up and spin-down states respectively. The spin-orbit interaction term is diagonalized in the above representation.

The strength of the transition matrix element along x,y, and z directions can be evaluated using these conduction and valence band wave functions and assuming $|\langle F_{hh,n} | F_{e,n} \rangle|^2 = 1$. The matrix element can be integrated over the azimuthal angle ϕ in the plane of the quantum well. For luminescence propagating along the 'y' direction, TE polarization is defined as $\hat{e} = \hat{x}$ and TM polarization is defined as $\hat{e} = \hat{z}$.

TE polarization $\rightarrow \hat{e} = \hat{x}$

$$|M_T|_{c-hh}^2 = \left[\langle u_s \uparrow | \hat{x} \cdot p_x | u_{hh \uparrow} \rangle|^2 + \langle u_s \downarrow | \hat{x} \cdot p_x | u_{hh \downarrow} \rangle|^2 \right] |\langle F_{hh,n} | F_{e,n} \rangle|^2 = \frac{M^2}{2} (\cos^2\theta \cos^2\phi + \sin^2\phi) |\langle F_{hh,n} | F_{e,n} \rangle|^2$$

$$\begin{aligned}
|M_T|_{c-lh}^2 &= \left[\langle u_s \uparrow | \hat{x} \cdot p_x | u_{lh} \uparrow \rangle|^2 + \langle u_s \downarrow | \hat{x} \cdot p_x | u_{lh} \downarrow \rangle|^2 \right] |\langle F_{lh,n} | F_{e,n} \rangle|^2 \\
&= M^2 \left(\frac{2}{3} \sin^2 \theta \cos^2 \phi + \frac{1}{6} \cos^2 \theta \cos^2 \phi + \frac{1}{6} \sin^2 \phi \right) |\langle F_{hh,n} | F_{e,n} \rangle|^2
\end{aligned}$$

TM polarization - $\hat{e} = \hat{z}$

$$\begin{aligned}
|M_T|_{c-hh}^2 &= \left[\langle u_s \uparrow | \hat{z} \cdot p_z | u_{hh} \uparrow \rangle|^2 + \langle u_s \downarrow | \hat{z} \cdot p_z | u_{hh} \downarrow \rangle|^2 \right] |\langle F_{hh,n} | F_{e,n} \rangle|^2 \\
&= \frac{M^2}{2} \sin^2 \theta |\langle F_{hh,n} | F_{e,n} \rangle|^2 \\
|M_T|_{c-lh}^2 &= \left[\langle u_s \uparrow | \hat{z} \cdot p_z | u_{lh} \uparrow \rangle|^2 + \langle u_s \downarrow | \hat{z} \cdot p_z | u_{lh} \downarrow \rangle|^2 \right] |\langle F_{lh,n} | F_{e,n} \rangle|^2 \\
&= M^2 \left(\frac{2}{3} \cos^2 \theta + \frac{1}{6} \sin^2 \theta \right) |\langle F_{lh,n} | F_{e,n} \rangle|^2
\end{aligned}$$

Averaging the matrix elements over the azimuthal angle ϕ in the plane of the quantum well, the TE and TM transition strengths due to C-HH and C-LH transitions become

$$\begin{aligned}
|M_T|_{TE}^2 &= M^2 \left[\left(\frac{3}{4} (1 + \cos^2 \theta) |\langle F_{hh,n} | F_{e,n} \rangle|^2 \right) + \left(\frac{5}{4} - \frac{3}{4} \cos^2 \theta \right) |\langle F_{lh,n} | F_{e,n} \rangle|^2 \right] \\
|M_T|_{TM}^2 &= M^2 \left[\left(\frac{3}{2} \sin^2 \theta \right) |\langle F_{hh,n} | F_{e,n} \rangle|^2 + \left(\frac{1}{2} + \frac{3}{2} \cos^2 \theta \right) |\langle F_{lh,n} | F_{e,n} \rangle|^2 \right]
\end{aligned}$$

Figure 3.8 illustrates the strength of the transition matrix elements corresponding to TE and TM polarizations when electron wave vector \mathbf{k} is along the z direction ($\theta=0$) and the envelope function overlap term is assumed to be unity.

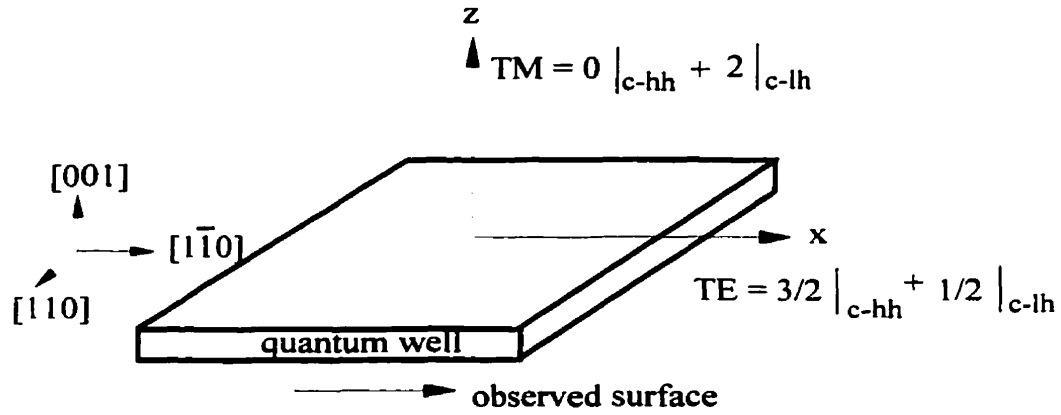


Figure 3.8 Relative band edge transition strengths for quantum wells.

In quantum wells, since the motion of the carriers is quantized along the direction of growth (\hat{z}), the electron \mathbf{k} is predominantly along \hat{z} . Hence, assuming $\theta=0$ gives a reasonable estimate of the polarization dependence of the matrix element. The above equations demonstrate that the c-hh transitions result predominantly in TE polarized luminescence and c-lh transitions result predominantly in TM polarized luminescence. For a given pumping, the number of c-hh and c-lh transitions depend on the density of states available for transitions in each energy level ($\rho_{red} f_c(1-f_v)$). For small carrier densities, the luminescence mainly corresponds to the first quantized energy level. The intensity of TE and TM polarized luminescence can be given by

$$L_{TE} \propto \int_0^{k_{max}} \sum_{i=hh, lh} |M_{TE}|_{c-i}^2(k_1) \rho(k_1) f_c(E(k_1))(1-f_v(E(k_1))) dk_1$$

$$L_{TM} \propto \int_0^{k_{max}} \sum_{i=hh, lh} |M_{TM}|_{c-i}^2(k_1) \rho(k_1) f_c(E(k_1))(1-f_v(E(k_1))) dk_1$$

The integration accounts for all possible energy transitions between all subbands. The degree of polarization of edge emission can be calculated from

$$DOP = \frac{L_{TE} - L_{TM}}{L_{TE} + L_{TM}}$$

As the thickness of the epilayers enters into the quantization regime, the degeneracy at the zone centre (Γ) is lifted by the quantum size effect [9]. The light hole energy level shifts to a higher energy with respect to the heavy hole. This gives rise to a larger transition matrix element for a conduction band to heavy hole (C-HH) transition than for a conduction band to light hole (C-LH) transition and also an enhanced probability of occupation of the heavy hole energy levels over the light hole energy (LH) levels. Since the C-HH transitions are predominantly TE polarized, quantum size effects result in an increased TE polarized luminescence relative to TM polarized luminescence [84,92] leading to a higher DOP_{110} as is seen in Figs. 3.3 and 3.5. As the thickness is reduced, the HH-LH energy level separation increases leading to a further increase in DOP_{110} .

Strain destroys the cubic symmetry of the crystal and lifts the degeneracy at the Γ point [22]. When the crystal is under compression, the shift of the heavy hole energy levels with respect to the light holes is in the same direction as that of the introduction of quantum size effects discussed earlier. Hence, one would expect an increase in TE polarized luminescence as the layer is under compression. This is observed as an increase in DOP_{110} as shown in Figs. 3.3 and 3.5. When the strain in the layer moves toward tension, the heavy

hole and the light hole energy levels approach each other and under large tension, the levels cross resulting in an enhanced TM polarized luminescence. This gives rise to a decrease in the observed DOP_{110} .

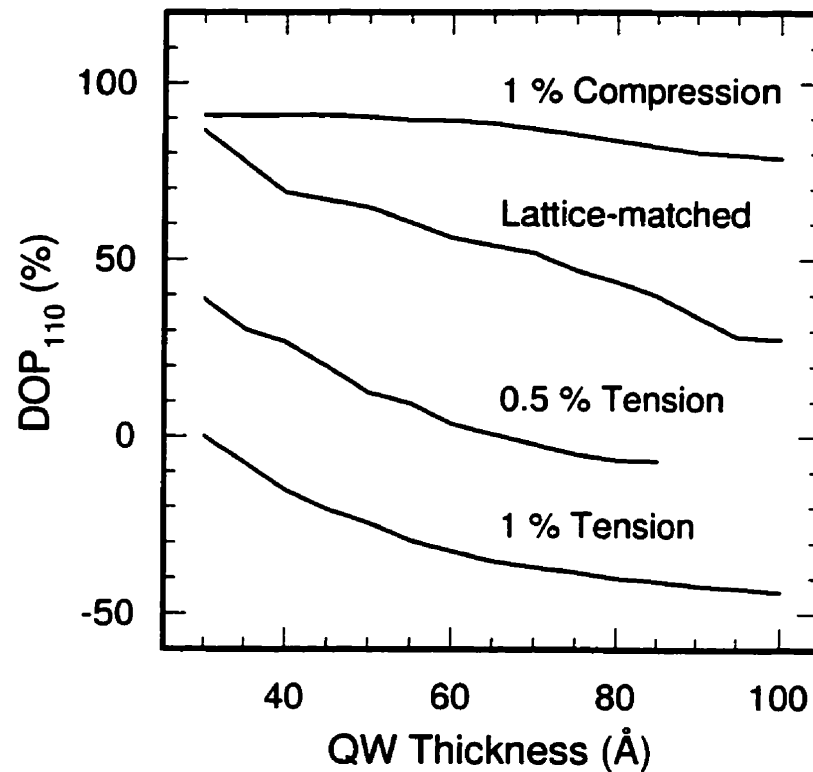


Figure 3.9 Theoretical prediction of variation of DOP_{110} with quantum well thickness for four different strain conditions.

A theoretical calculation has been performed with an effective-mass approximation and an envelope function approach. The effect due to the split-off band was neglected and the electron wave vector was taken to be along \hat{z} . The trend of the calculated DOP_{110} with strain and thickness, shown in Fig 3.9, matches well with that of the experimental results

(Fig. 3.4) though not the absolute values. The factors that would reduce the accuracy of the theoretical predictions include the simplicity of the model, band-offset ratio, effective masses of the electrons and the holes, the effect of the split-off band [95,89] and the exclusion of the structural details of the quantum well, including interfaces.

3.5 TE and TM spectral measurements

Standard methods to confirm the material composition and thickness of wells are either photoluminescence (PL) spectra or polarization-resolved photoluminescence spectra (PPL). It has been shown in sample Set II that DOP_{110} measurements are more sensitive than the PPL spectral measurements to small variations (of the order of 10^{-3}) in strain. However, in sample Set I, the strain and thickness variations are large. Hence, we use PPL spectra to confirm the characteristics of the materials under study and to compare with the DOP_{110} results presented in Section III.

Figure 3.10 shows the room-temperature PPL spectra for a 100\AA thick quantum well for the three strain conditions of sample Set I. $\Delta\lambda$ corresponds to the relative shift of the peak of the TE and TM polarized edge emission luminescence and is in agreement with the expected splitting of the heavy hole and light hole energy levels as discussed in the previous section [96,22].

Figure 3.11 depicts the PPL spectra for lattice-matched layers of thicknesses of 300, 100 and 30\AA . The results indicate that as the thickness is reduced $\Delta\lambda$ increases. However,

the increase in $\Delta\lambda$ is not very obvious in the 30Å well. The broad peak and the line shape of the TM luminescence is reported to be the result of the strong mixing of the heavy hole and the light hole character in the valence band and many body effects [19]. It is worth noting the tremendous reduction in the amount of TM polarized luminescence as the thickness of the well is reduced. This confirms the increased separation between HH and LH energy levels. As the separation of the HH and LH energy levels increases, an increase in the DOP_{110} of the luminescence is expected, as discussed in the previous section. Indeed, a sharp increase in the DOP_{110} is observed as the thickness is reduced from 100Å to 30 Å. Hence, room-temperature PPL spectral technique may not be an obvious choice to characterise thin wells where the TM luminescence is very small compared to TE and hence it is difficult to locate the peak energy of the TM spectra. Reliable DOP_{110} values can be obtained for thin wells as shown in Fig.3.4, once again proving the sensitivity of the technique. The results of simulation, in Fig. 3.9, agree well with the trend observed in the PPL spectral data for both strain and thickness of single quantum wells.

3.6 Summary

The degree of polarization of edge emission photoluminescence (DOP_{110}) is shown to be a sensitive function of the strain and thickness of a quantum well. For lattice-matched conditions, an increase in the DOP_{110} of 35 percentage points (i.e, from 27% to 62%) is observed for a thickness change from 100Å to 30Å. A variation of DOP_{110} on a 50Å thick sample is about 70 percentage points as the strain varies from about 1% compression to 1%tension. The predictions of a simple theory are consistent with the observed dependence

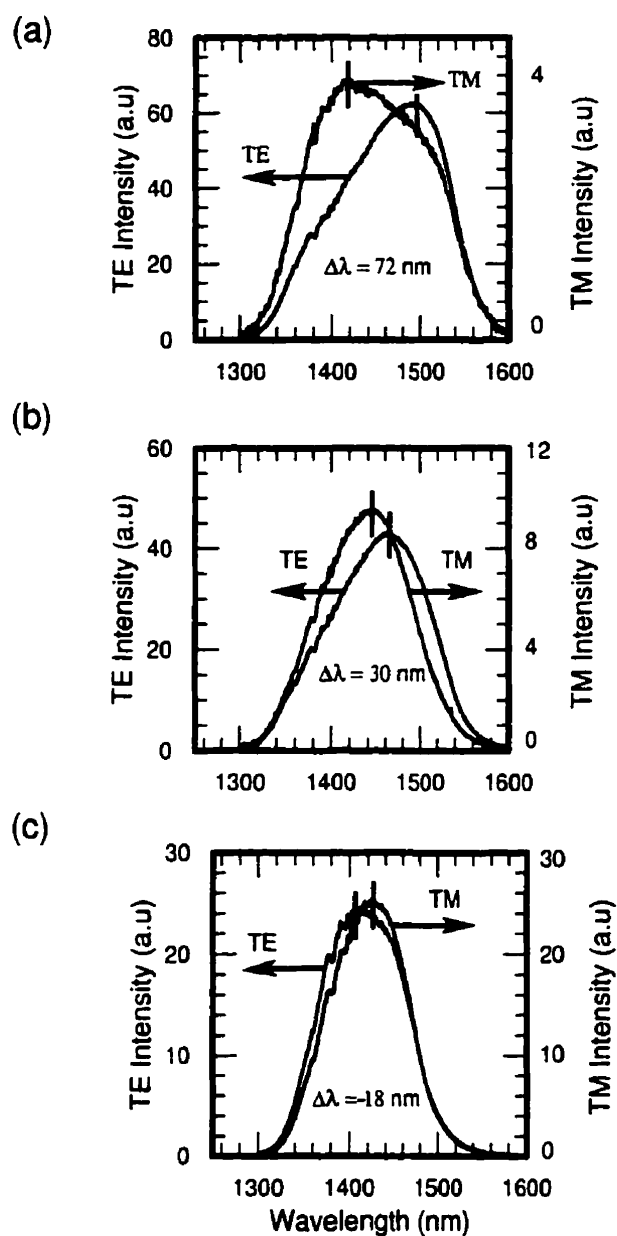


Figure 3.10 Room-temperature polarization-resolved photoluminescence spectra on a 100 Å-thick quantum well for three strain conditions: **(a)** 1% compression; **(b)** lattice-matched; **(c)** 1% tension

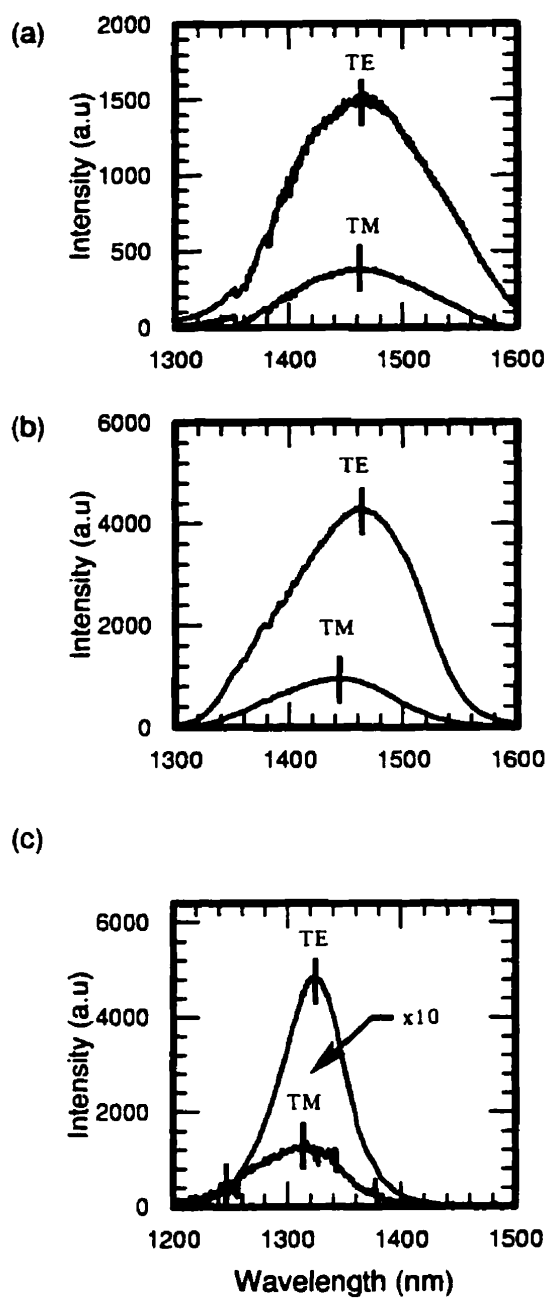


Figure 3.11 Room-temperature polarization-resolved photoluminescence spectra on three lattice-matched layers of thickness 30, 100, and 300 Å: (a) 300 Å; (b) 100 Å; (c) 30 Å. The TM intensity in (c) is scaled by a factor of 10.

of the DOP_{110} on thickness and strain, although the absolute values do not agree with the observations. DOP_{110} results are in agreement with the polarization-resolved photoluminescence spectral measurements. However, measurement of the DOP_{110} is substantially faster, and at room temperature, more sensitive than the spectral technique.

Chapter 4. Anisotropic Interfacial Strain

4.1 Introduction

Zinc-blende semiconductors belong to the D_{2d} symmetry group. From considerations of symmetry and for quantum wells grown on (001) oriented substrates, the luminescence that is emitted normal to the plane of the quantum well is not expected to show an anisotropy of polarization of luminescence in the in-plane of the quantum well (i.e., between [110] and $[1\bar{1}0]$ directions). To quantify the anisotropy of polarization of luminescence between [110] and $[1\bar{1}0]$ directions, we define a parameter Degree of polarization of luminescence, DOP_{001} , as

$$DOP_{001} = \frac{\int_0^{\infty} [L_{110}(E) - L_{1\bar{1}0}(E)] R(E) dE}{\int_0^{\infty} [L_{110}(E) + L_{1\bar{1}0}(E)] R(E) dE} \quad (4.1)$$

where L_{110} and $L_{1\bar{1}0}$ are the magnitudes of the luminescence polarized in the [110] and $[1\bar{1}0]$ directions respectively and propagating near the [001] direction. $R(E)$ is the responsivity of the detector. Room-temperature polarization-resolved photoluminescence measurements from (001) surface of bulk InP material show a DOP_{001} of less than 0.2 percentage points, which is of the order of the rms noise of the measurement system. However, DOP_{001} from the (001) surface of InP/InGaAs/InP quantum wells were in the range of 3 to 28 percentage points depending on the thickness, composition (strain) in the well, and the conditions of the

growth interruption at the interfaces. In this chapter, I present the measured observations of room-temperature, polarization-resolved photoluminescence from the (001) surface, i.e., [001] growth direction, of InP/InGaAs/InP quantum wells and attribute the observations to anisotropic structures at the interfaces of the quantum wells.

4.2. Experimental Details

The apparatus used to measure DOP_{001} is shown in Fig 4.1. The samples were excited by a He-Ne laser that was passed through a chopper. Both the excitation and collection were

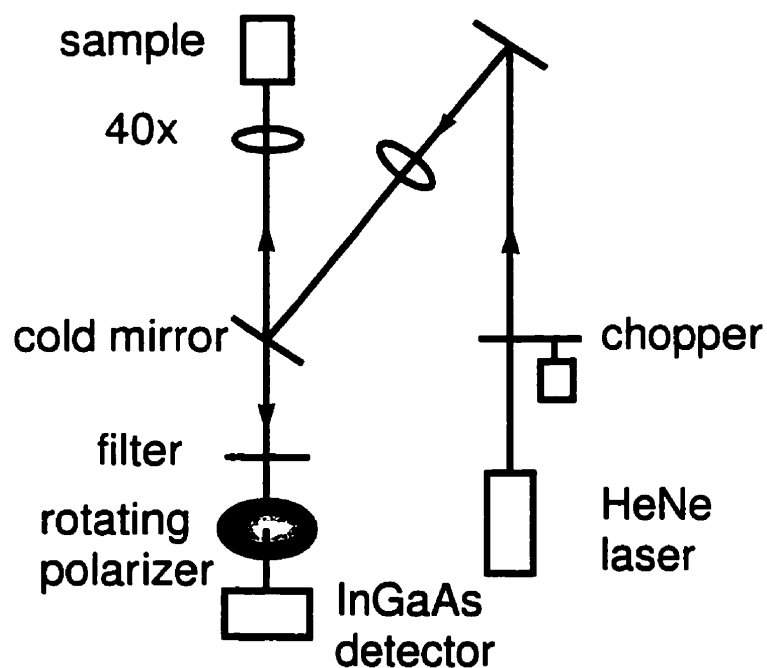


Figure 4.1 Experimental Apparatus

along the [001] direction. A polarizer beam splitter cube can be used to separate the luminescence polarized along [110] and $[1\bar{1}0]$ directions (i.e. L_{110} and $L_{1\bar{1}0}$) and measured simultaneously using two photodiodes. However, we used a rotating linear polarizer instead of a polarizer beam splitter cube to measure DOP_{001} . Demodulation of the output of the photodiode, by phase sensitive detectors, at the frequency of the chopper and at twice the rate of rotation of the polarizer enables simultaneous measurement of $(L_{110}+L_{1\bar{1}0})$ and $(L_{110}-L_{1\bar{1}0})$ summed over all the energy transitions. The details of the measurement technique are given in chapter 2. A 1.0 μm long pass filter was used to block the luminescence from InP.

All the samples used for this study were grown by gas source molecular beam epitaxy at typically 460°C. The group V fluxes consisted primarily of dimers, P_2 and As_2 , derived from the pyrolysis of phosphine and arsine in a dual filament cracker. A typical sample structure is shown in Fig. 4.2a. Two interfaces are marked in the figure. The bottom interface (I_1) corresponds to the end of the InP buffer and the start of the InGaAs quantum well, where the gas switching is from phosphine to arsine. The top interface (I_2) corresponds to the InGaAs quantum well and InP cap layer interface, where the switching is from arsine to phosphine. A typical gas switching sequence is shown in Fig. 4.2b. In a normal growth sequence, growth is interrupted (by shuttering group III sources) at the interfaces and the required gas flow is established before resuming the growth. We define dwell time or growth interruption time as the time for which the new gas is switched on before resuming the growth of the next layer. Group III composition (i.e. Ga or In fraction) in the quantum wells is based on the flux versus temperature calibration of the effusion cells which in turn is

determined from double crystal x-ray diffraction, growth rate, and photoluminescence measurements of thick InGaAs epilayers on InP.

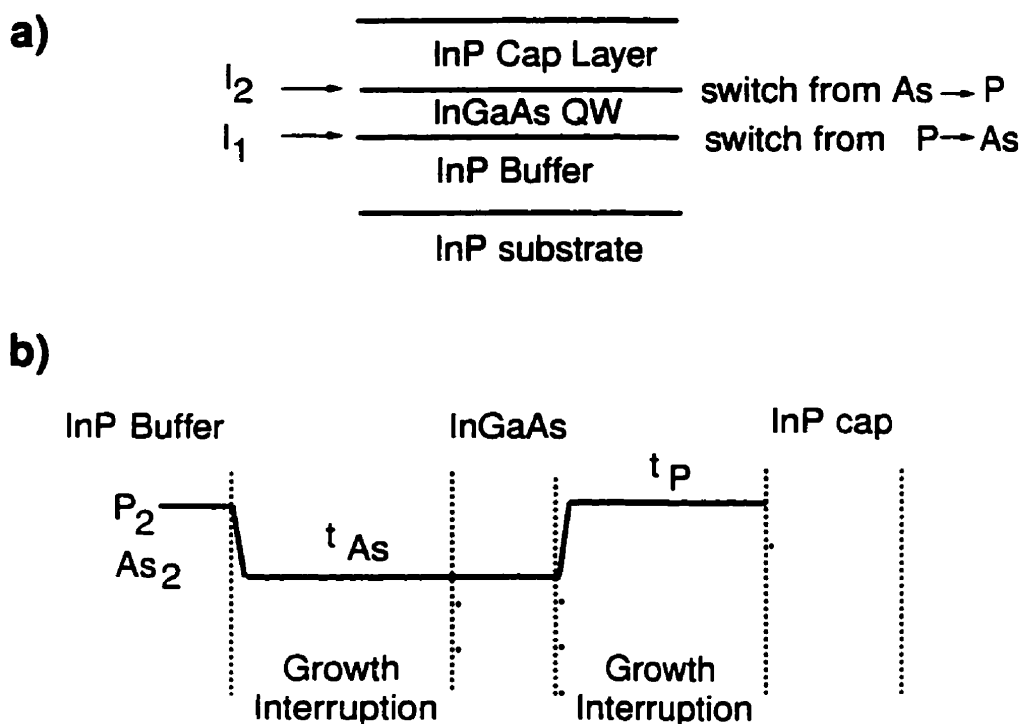


Figure 4.2 Typical a) Material Structure, and b) Growth sequence

4.3 Results

Figure 4.3 is a plot of the measured DOP_{001} versus the reciprocal of the quantum well thickness (L) for nominally lattice-matched InP/InGaAs/InP quantum wells. The thickness of the quantum well was varied from 300Å to 20Å. A fixed growth interruption time of 120 seconds was used in these samples. An increase in DOP_{001} of 16 percentage points is observed for a thickness change from 100Å to 20Å. This is in contrast with the DOP_{001} of 0.2

percentage points measured for the luminescence from bulk InP sample. A least-square fit to the data gives

$$DOP_{001} = [(-0.96 \pm 0.023) + (407 \pm 0.78)/L] \quad (4.2)$$

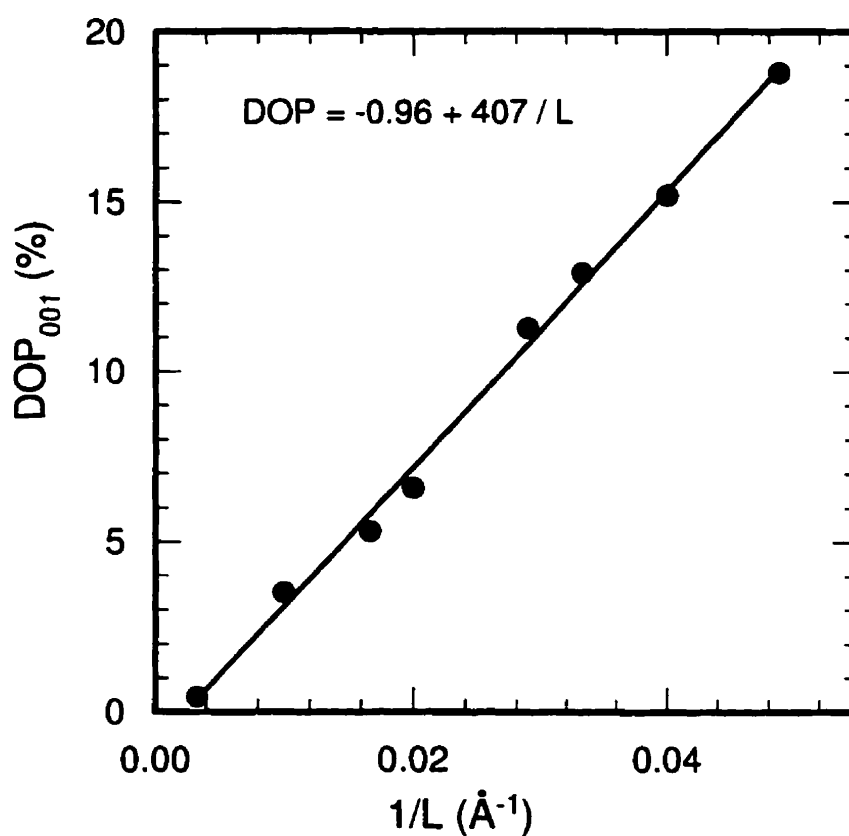


Figure 4.3 Variation of degree of polarization of photoluminescence from a (001) surface (DOP_{001}) with the reciprocal of the quantum well thickness ($1/L$). L is varied from 300\AA to 20\AA .

Within the experimental precision (1σ , σ is the standard deviation) of ± 0.25 percentage points, all eight data points fall within 1.2σ of the fitted curve. The linear relationship of DOP_{001} with the reciprocal of the quantum well thickness suggests that the anisotropy of polarization may be purely an interface phenomena.

Table 1 shows the dependence of DOP_{001} of the luminescence from the quantum well on the growth interruption time, at I_1 and I_2 interfaces for 20Å-thick, lattice-matched InGaAs quantum wells. The most significant dependence of DOP_{001} on growth interruption times occurs at the top interface.

	Growth Interruption Time		DOP_{001} (%)
	(seconds)		
	I_1	I_2	
a)	5	5	10.3
b)	80	80	18.8
c)	660	870	23.2
d)	240	5	13.4
e)	5	240	21.6

Table 4.1 Variation of DOP_{001} with growth interruption time. I_1 is the buffer/QW interface and I_2 is the QW/cap layer interface.

When the growth interruption time (i.e., dwell time) at the bottom interface was varied from 5 to 240 seconds, the change in the DOP_{001} was measured to be 3 percentage points [53] (c.f. row 'd' and 'a' in Table 1). Whereas, when the growth interruption was varied from 5 to 240 seconds at the the top interface I_2 , DOP_{001} increased by 11 percentage points (c.f. row 'e' in Table 4.1).

The dependence of DOP_{001} with the growth interruption time at the interface I_2 was studied in detail by keeping the growth interruption time at I_1 fixed. Figure 4.4 shows the variation of DOP_{001} with the dwell time in phosphorous at the top interface (t_p) for 20Å thick, nominally lattice-matched InGaAs quantum wells. The growth interruption at the bottom interface was kept fixed at 60 seconds while the dwell time at the top interface was changed. The DOP_{001} increased from 12 to 23 percentage points as t_p was varied from 0 to 600 seconds. The inset shows an magnified version over 150 seconds. For very long gas switching times DOP_{001} appears to approach a saturation value. Low-temperature photoluminescence spectra at 14K on samples a,b and c, marked in Fig. 4.4, are presented in Fig. 4.5. The data indicate a blue shift [44] as the growth interruption time is increased and the FWHM (≈ 10.0 meV) does not show a significant variation. Changes in the line shape due to growth interruption have been attributed to the interface roughness by other groups [25,26,97]. Since the line width does not appear to depend on the time of growth interruption, we believe that interface roughness does not account for the observed changes in DOP_{001} shown in Fig. 4.4.

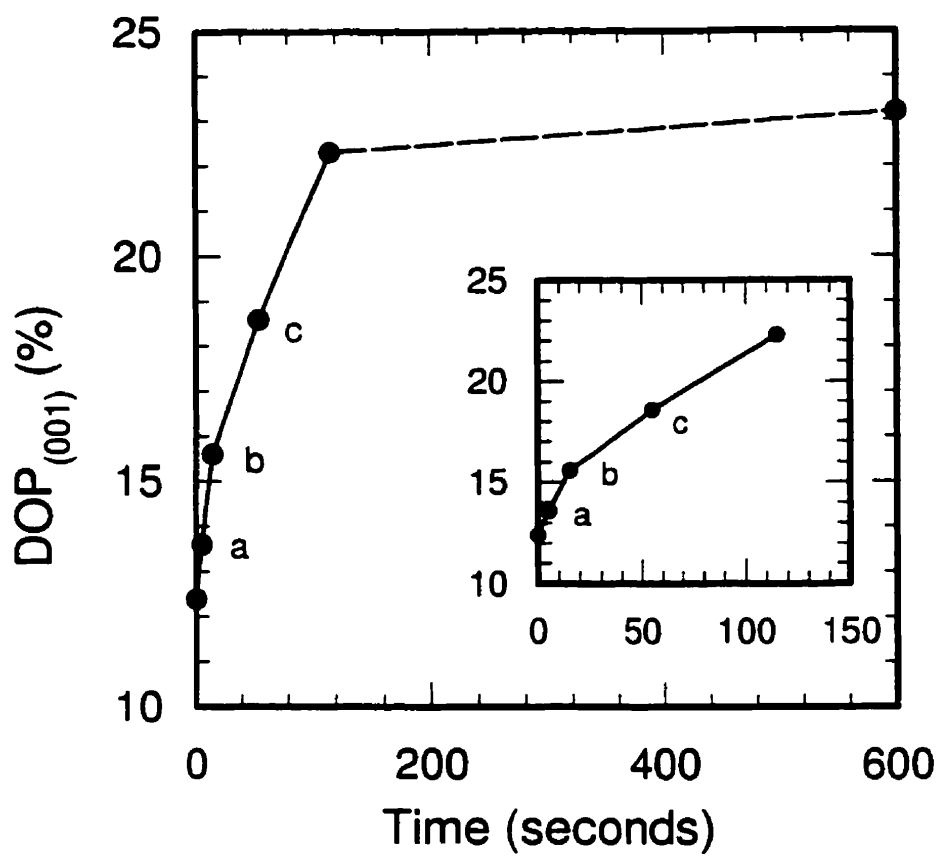


Figure 4.4 Variation of degree of polarization of photoluminescence from a (001) surface (DOP_{001}) with the dwell time in phosphorous.

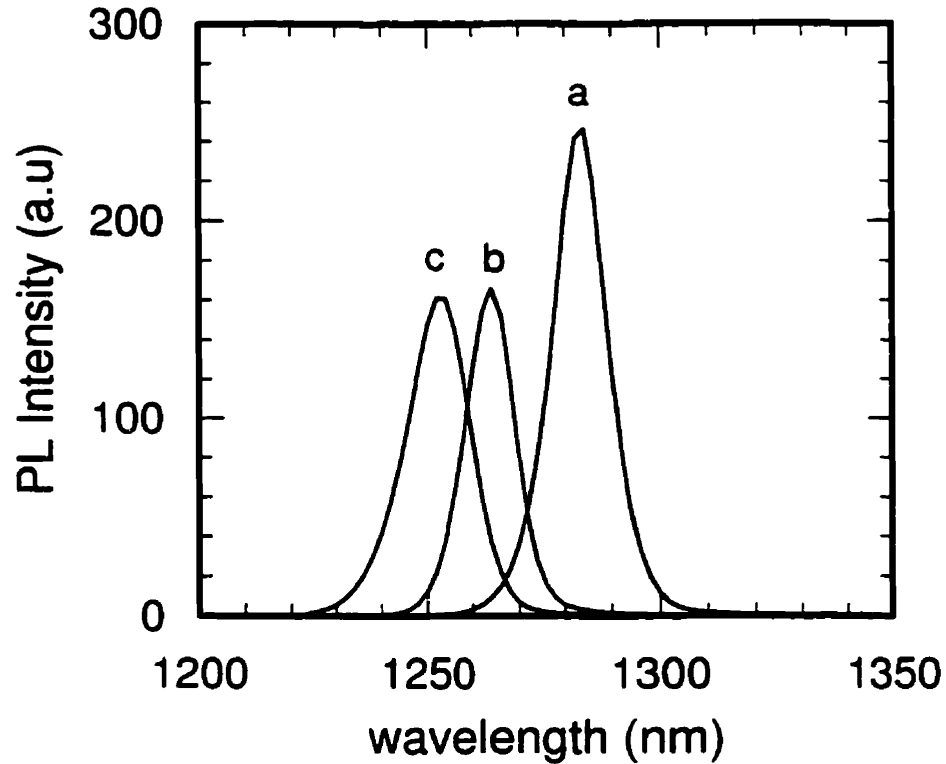


Figure 4.5 14K PL spectra for three cases of dwell time in phosphorous (t_p):
a) $t_p = 5$ sec., **b)** $t_p = 15$ sec., and **c)** $t_p = 55$ sec.

The dependence of DOP_{001} on the Ga mole fraction (x) in the quantum well is shown in Fig. 4.6 for wells of thickness 20\AA . A fixed gas switching time of 60 seconds was used at the top interface. DOP_{001} increased from 10 to 28 percentage points as the Ga composition was increased from 0.32 to 0.60. This observation, coupled with the data of Fig. 4.4, indicates that the Ga and P content at the interfaces play a significant factor in DOP_{001} .

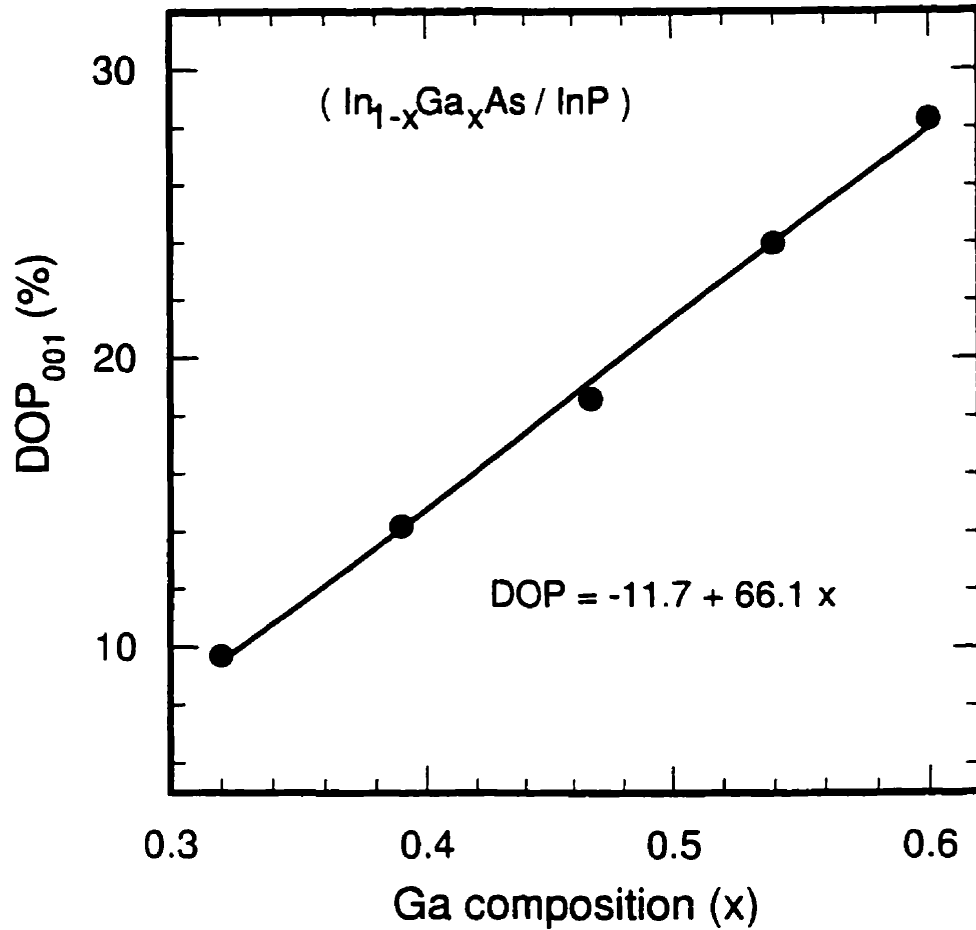


Figure 4.6 Variation of degree of polarization of photoluminescence from a (001) surface (DOP_{001}) with the Ga composition in the well.

4.4 Discussion

DOP is the measure of the anisotropy of polarization of luminescence in two orthogonal directions and is proportional to the difference in the strain components along the two directions. From previous calibration experiments¹⁹ using a beam-bending technique

described in chapter 2, the degree of polarization of luminescence along a $[110]$ direction, ρ_{110} (which is equal to $[\int(L_{1\bar{1}0} - L_{001})R(E)dE / \int(L_{1\bar{1}0} + L_{001})R(E)dE]$), is given by

$$\rho_{110} = -C_{\epsilon} (\epsilon_{1\bar{1}0} - \epsilon_{001}) \quad (4.3)$$

where $\epsilon_{1\bar{1}0}$ and ϵ_{001} are the components of strain along the $[1\bar{1}0]$ and $[001]$ directions respectively; C_{ϵ} is a constant obtained from polarization resolved photoluminescence measurements performed along $[110]$ direction in bulk InP material with V-groove structures. A compressive strain along $[1\bar{1}0]$ direction enhances the amount of light polarized along the $[1\bar{1}0]$ direction and results in a positive ρ_{110} .

In the case of InP/InGaAs/InP quantum wells, we attribute the DOP_{001} to the effect of an anisotropic strain field that is associated with the strained bonds at the top and the bottom interfaces of the quantum well. The anisotropic strain field, we believe, is due to the combination of two factors: a) the partial As surface coverage at the growth-interrupted, surface-reconstructed top interface leading to a mixed As/P interface upon introducing the P_2 flux and resuming the growth of InP, and b) the amount of Ga at the interfaces.

Under typical growth conditions, the surface tends to reconstruct into a Group V terminated surface which contains missing dimer rows. For example, the InP surface reconstructs to form a 2×4 or $c(2 \times 8)$ structure, presumably with 75% phosphorous coverage [69,98,99,100] as discussed in section 2.4. Arsenic rapidly replaces phosphorous during the

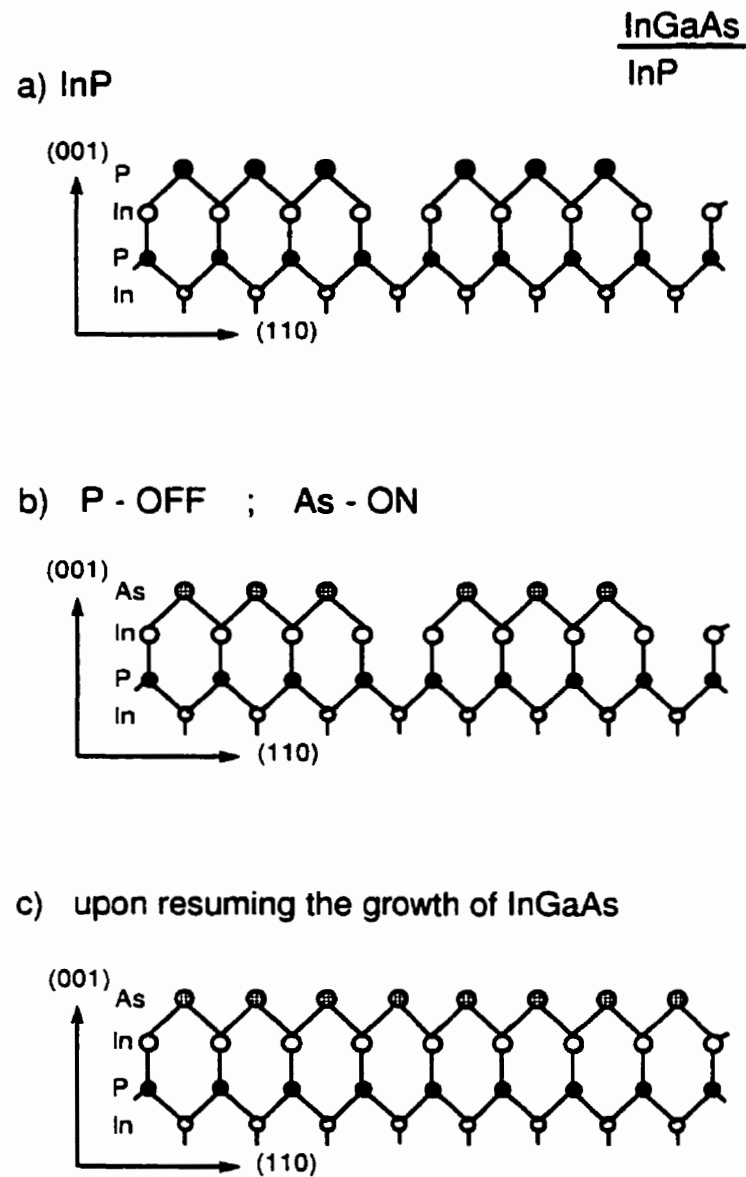


Figure 4.7 Ball-and-stick model showing three stages of reconstruction at the bottom interface a) P-terminated, (2×4)-reconstructed surface; b) Replacement of P by As when As was switched ON; c) Upon resuming the growth of InGaAs

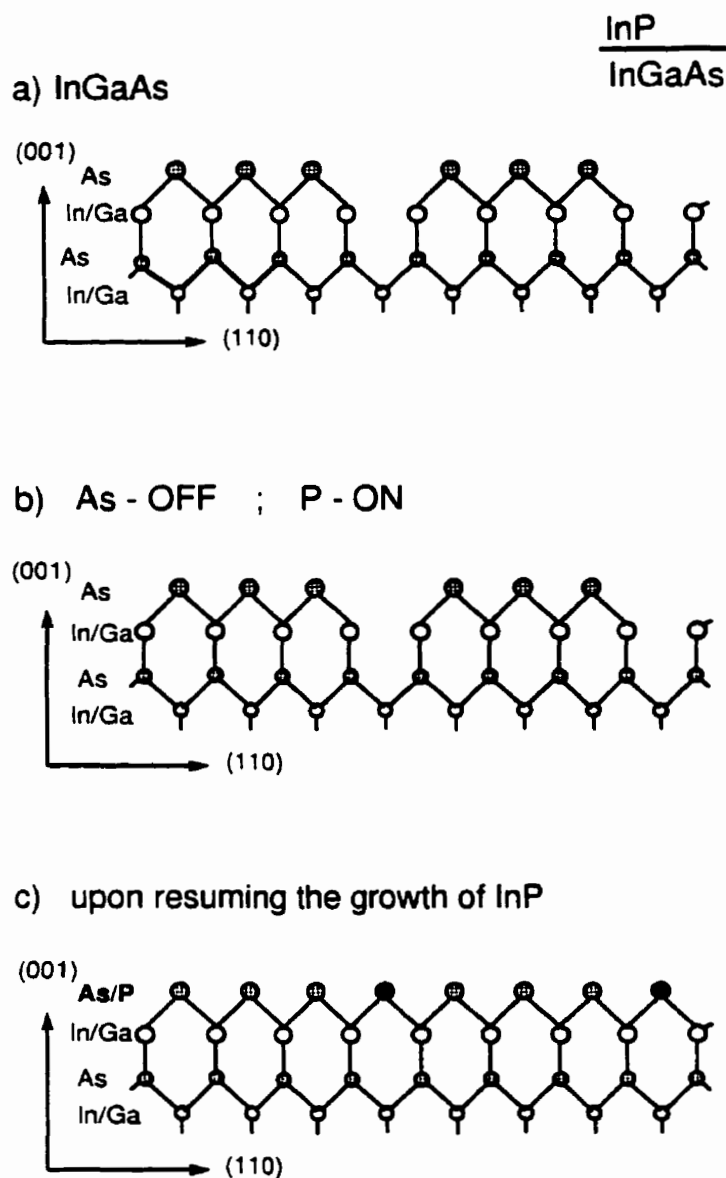


Figure 4.8 Ball-and-stick model showing three stages of reconstruction at the top interface **a)** As-terminated, (2×4) -reconstructed surface; **b)** When P was switched ON, the surface is still As-terminated; **c)** Upon resuming the growth of InP.

Group V flux change [101,102,103] from P to As during the growth interruption. This results in a reconstructed, As-terminated surface at the bottom interface I1. Upon resuming the growth at the start of the InGaAs quantum well, the missing dimers in the As-terminated surface are filled with As and this results in strained In-As bonds which are directed along [110] and strained In-As and Ga-As bonds along $[1\bar{1}0]$ direction. The situation at the bottom interface is depicted in Fig. 4.7 in three different stages. However, P does not readily replace As during the Group V flux change from As to P during the growth interruption. Upon resuming growth at the start of the cap layer (InP), the phosphorous flux fills the sites not occupied by As dimer rows as shown in Fig. 4.8. This results in a mixed As/P monolayer at the top interface, I2, with strained In-As, Ga-P and Ga-As bonds, directed along the [110] direction, and strained In-As bonds directed along $[1\bar{1}0]$. Figure 4.9 is schematic diagrams of the bonding at both the interfaces and for two orthogonal directions.

An estimate of the DOP_{001} of the luminescence from the quantum well may be obtained by calculating an effective strain field ϵ due to the stress arising from the lattice-mismatched In-As, Ga-As, and Ga-P bonds at the interfaces. Referring to Fig. 4.7 and using a force balance equation of the form, $-Y\epsilon = \sum n_i Y_i \epsilon_i$ (where ϵ and Y are the strain and stiffness of the InGaAs quantum well and n_i , Y_i , and ϵ_i are the number, stiffness and mismatch of the interfacial lattice-mismatched bonds where 'i' refers to Ga-As, In-As, and Ga-P bonds), the effective strains due to each interface, I1 and I2, along two orthogonal directions, [110] and $[1\bar{1}0]$, can be computed from the following equations: .

$$-Y [\epsilon_{11}]^{(110)} = [\epsilon_{\text{In-As}} Y_{\text{In-As}}] \quad (4.4)$$

$$-Y [\epsilon_{11}]^{(1\bar{1}0)} = [(1-x) (\epsilon_{\text{In-As}} Y_{\text{In-As}}) + x(\epsilon_{\text{Ga-As}} Y_{\text{Ga-As}})] \quad (4.5)$$

$$\begin{aligned} -Y [\epsilon_{12}]^{(110)} = f [(1-x) (\epsilon_{\text{In-As}} Y_{\text{In-As}}) + x (\epsilon_{\text{Ga-As}} Y_{\text{Ga-As}})] \\ + x(1-f)[(\epsilon_{\text{Ga-P}} Y_{\text{Ga-P}})] \end{aligned} \quad (4.6)$$

$$-Y [\epsilon_{12}]^{(1\bar{1}0)} = f [\epsilon_{\text{In-As}} Y_{\text{In-As}}] \quad (4.7)$$

The superscript refers to the direction of the bond, f is the fraction of As atoms, and x is the Ga content.

The DOP_{001} arises due to the anisotropy in the strain, that is, the difference between the strains in the $[110]$ and $[1\bar{1}0]$ directions. In general, the DOP_{001} of luminescence from a biaxially strained material is zero since the luminescence from the two orthogonal directions is equivalent. In the quantum well away from the interfaces, the In-As and Ga-As bonds occur in each direction resulting in biaxial symmetry and hence no contribution to DOP_{001} . However, the total strain in the quantum well is anisotropic and the difference in the strain between the $[110]$ and $[1\bar{1}0]$ directions is obtained by rearranging Eqs. 2,3,4, and 5.

$$-Y (\epsilon_{110} - \epsilon_{1\bar{1}0}) = x (1-f) [(\epsilon_{\text{Ga-P}} Y_{\text{Ga-P}}) - (\epsilon_{\text{Ga-As}} Y_{\text{Ga-As}}) + (\epsilon_{\text{In-As}} Y_{\text{In-As}})] \quad (4.8)$$

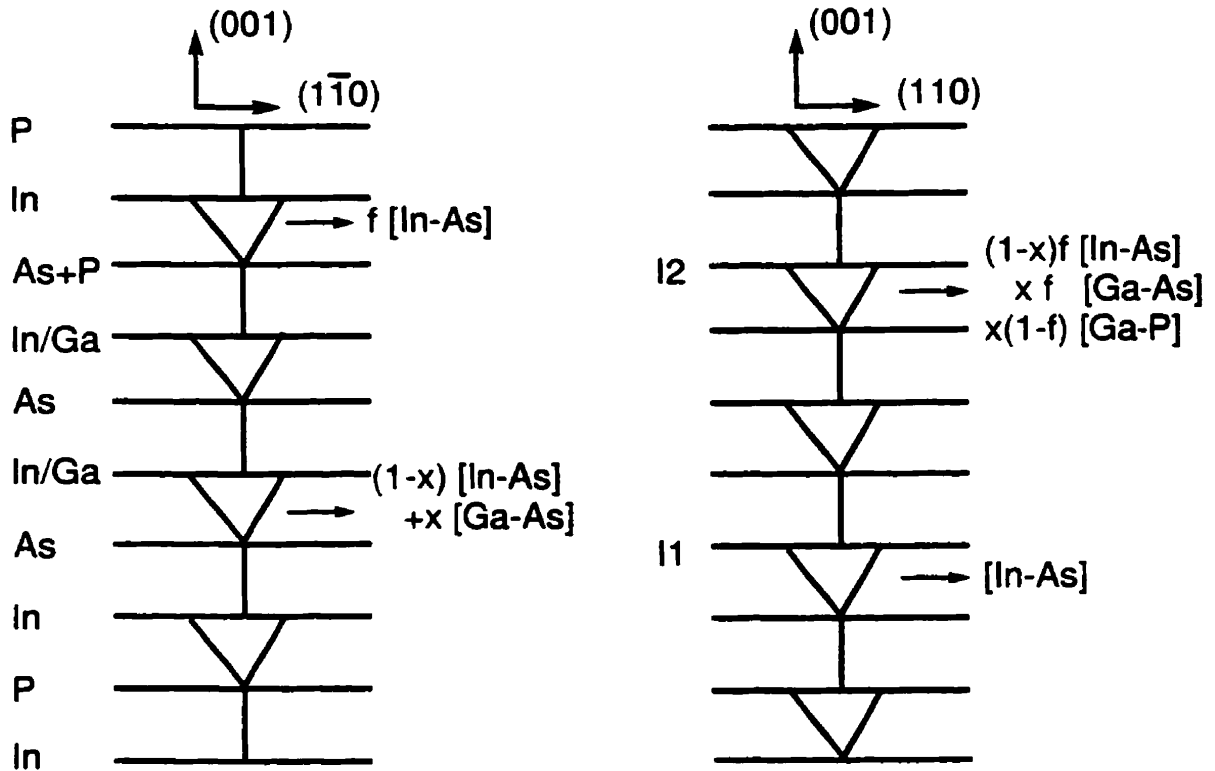


Figure 4.9 Bonding schematic along $[110]$ and $[1\bar{1}0]$ directions. 'f' is the fraction of As atoms, and 'x' is the Ga content.

Evaluation of Eq. 8 using the mismatches with respect to InGaAs (which is nominally lattice-matched to InP) for the strains ($\epsilon_{\text{InAs}} = -0.0313$, $\epsilon_{\text{GaAs}} = 0.0381$, $\epsilon_{\text{GaP}} = 0.0767$) [104] and the stiffness factors as the ratios of the Young's modulus to that of InGaAs ($Y_{\text{InAs}}/Y = 0.752$, $Y_{\text{GaAs}}/Y = 1.2479$, $Y_{\text{GaP}}/Y = 1.5042$) [104], gives a net difference in strain of

$$-(\epsilon_{110} - \epsilon_{1\bar{1}0}) = \{ x(1-f) [0.0442]^{(110)} \} \quad (4.9)$$

The Young's modulus for InGaAs, Y , was obtained as a weighted sum of the moduli for

InAs and GaAs. We believe that this net anisotropic tensile strain in the interfaces produces an effective compressive strain in the quantum well along the [110] direction. This results in a nonzero DOP_{001} with the luminescence from the quantum wells more polarized along the [110] direction than the $[1\bar{1}0]$ direction. The dependence of DOP_{001} on the reciprocal of the quantum well thickness, (c.f. Fig. 4.3), agrees qualitatively with the above model which attributes the source of the anisotropic strain to the interfaces. Thus, the impact of the anisotropic strain is larger for the thinner wells where the relative volume of the interfacial perturbation with respect to the total quantum well is larger.

More quantitatively, the maximum value of the DOP_{001} may be estimated from Eq. 4.9 using the linear relationship between DOP and the difference in strain, given in Eq. 4.3. Taking $C_\epsilon = 37.9$, $x = 0.5$, and $f = 0.33$ for a surface reconstruction of 2×3 (The surface reconstruction of InGaAs, i.e., interface I2, was observed to be a fuzzy 2×3 in Reflection High Energy Electron Diffraction. There is an experimental evidence [100] that for GaAs, a 2×3 reconstruction corresponds to 33% surface coverage) yields a value for DOP_{001} of 58 percentage points (corresponding to a strain of 1.5×10^{-2}). Extrapolating the experimental data of Figure 3 to a DOP_{001} of 58 percentage points gives a thickness for the quantum well of about 7\AA . This value for thickness is not inconsistent with the implicit assumptions in the above calculation that the strain required for force balance resides in a quantum well consisting of a single monolayer. Taking $f = 0.75$ for a surface reconstruction of 2×4 as in the case of InP surface, yields a DOP_{001} of 21 percentage points (corresponding to a strain of 6×10^{-3}). Hence, we expect the strain in the quantum well due to partial surface

coverage to be in the range of 6×10^{-3} to 1.5×10^{-2} . A quantitative explanation of the thickness dependence of DOP_{001} would require a model for the strain propagation away from the interfaces and into the quantum well material and InP barriers. A numerical simulation based on valence force field has been done to explain the trend of DOP_{001} with thickness of the quantum well, and the results are presented in chapter 5. It is important to note that the evaluation is sensitive to the assumed value for 'f' and the stiffness factors. If the stiffness of the bonds is assumed to be the same for all the bonds, the calculated DOP_{001} corresponding to a 2×3 reconstructed surface is about 9 percentage points (corresponding to a strain of 2.4×10^{-3}). Hence, it appears that the stiffness of the bonds is an important factor to be considered.

4.4.1 Contribution to DOP_{001} from Ga and P content

Ga-P, being the strongest bond (with largest Y and shortest equilibrium bond length), contributes the most to the strain field. Eq. 4.7 suggests that an increase in either the incorporation of P_2 [i.e., (1-f)] or the Ga content (x) can enhance the net interfacial tensile strain resulting in a larger DOP_{001} . The data of Figs. 4.4 and 4.6 qualitatively agree with the dependence of Eq. 4.7 on 'f' and 'x'.

Figure 4.4 shows that DOP_{001} increases as the dwell time in phosphorous at the top interface increases. As t_p increases, incorporation of P atoms at the interface increases as more arsenic atoms are replaced. This gives rise to an increase in the number of Ga-P bonds thereby increasing the anisotropic strain field and hence the DOP_{001} . Also, the blue shift of

31 nm in the spectral data (c.f. Fig. 4.5) is suggestive of an increase in the P content (Ref. Fig. 1.1) as t_p is increased from 5 to 115 seconds.

Finally, the data of Fig. 4.6, depicting the linear dependence of DOP_{001} on the Ga fraction (x) in the quantum well, is in agreement with the dependence of the anisotropic strain on x expressed in Eq. 4.7. It may be important to note that extrapolating the curve to $x = 0$ results in a DOP_{001} of -12 percentage points. This is not consistent with the model of Eq. 7. Measurements on thin samples (4 and 5 monolayers) of InP/InAs/InP quantum wells ($x = 0$) yielded a DOP_{001} of -2 percentage points. This suggests that the dependence of the net effective strain on Ga composition (x) may not be a true linear function for small values of x .

Hence, from the above arguments, one should not expect these anisotropic features in a material where both the well and the barrier materials contain the same Group V species or the difference in the amount of gallium content across the interfaces is negligible. Indeed, we have not observed any appreciable value of DOP_{001} (<0.5 percentage points) from GaAs/InGaAs/GaAs and GaAs/AlGaAs/GaAs quantum wells.

Another possible contributor to the DOP_{001} could be the anisotropic surface morphology in the quantum well [43]. However, we do not believe that the surface morphology anisotropy offers a major contribution to DOP_{001} in this work because we do not observe a significant DOP_{001} in GaAs/InGaAs/GaAs (or in AlGaAs/GaAs/AlGaAs) quantum

wells where any surface morphology effects would also be expected to be present. Also, two additional growths were performed at growth temperatures 435 °C and 485 °C. This change in the growth temperatures might be expected to alter the surface morphology anisotropy; however, no significant change in DOP_{001} was observed from the results reported in this work.

Other Related Experiments

If DOP_{001} is an undesirable feature, is it possible to reduce DOP_{001} by other experimental techniques apart from varying the growth conditions? There have been numerous studies in GaAs/InGaAs/GaAs and InP/InGaAsP/InP systems related to interdiffusion of group III and group V atoms across the interface between barrier and well due to ion-implantation and thermal annealing. Under interdiffusion process, we expected the interface to get smeared out and reduce the anisotropic features at the interface.

Thermal annealing of the samples did not alter the values of DOP_{001} . However, Ar-implantation of the samples tremendously changed the value of DOP_{001} . Table 4.2 shows how DOP_{001} decreases with the increase in implantation dosage from 1.5×10^{11} to 3×10^{12} /cm². The data for two samples are presented. The structure of the samples is given in Fig. 4.2a. The growth interruption times at the interfaces are given in Table 4.1. Sample 1 corresponds to row 'e' and sample 2 corresponds to row 'd' in Table 4.1. Along with the change in DOP_{001} , variation in the peak wavelength was also observed. PL spectra were measured at 14K. The blue shift is consistent with other ion-implantation experiments performed on similar type

sample No.	Ar-implant											
	Dose : 0 Energy : 0			Dose : 1.5E11/cm ² Energy : 15 keV			Dose : 5E11/cm ² Energy : 15 keV			Dose : 3E12/cm ² Energy : 20 keV		
	DOP (%)	λ_{peak} (nm)	FWHM (meV)	DOP (%)	λ_{peak} (nm)	FWHM (meV)	DOP (%)	λ_{peak} (nm)	FWHM (meV)	DOP (%)	λ_{peak} (nm)	FWHM (meV)
1	21.6	1174	10.4	20.08	1172	10.4	15.04	1161	13.8	2.11	1114	42
2	13.4	1290	11.2	13.4	1289	11.95	8.48	1280	18.2	0.5	1246	34.8

Table 4.2 Variation of DOP₀₀₁, PL peak wavelength, and FWHM with the increase of the ion-implantation dose

of materials. However, one should note that the decrease in λ_{peak} as DOP_{001} decreases is not consistent with the red shift observed in Fig. 4.5. Hence, it may be possible that reduction in DOP_{001} due to ion-implantation may not be related to the change in the P content at the interface but rather due to interdiffusion phenomenon. I would like to add that these set of measurements and analysis are only preliminary; but they add another method to alter the polarization properties of quantum wells.

4.5. Summary

The incomplete group V surface coverage due to surface reconstruction introduces anisotropic microstructural features at the interfaces of InP/InGaAs/InP quantum wells. The linear dependence of DOP_{001} with the inverse of quantum well thickness suggests that DOP_{001} arises mainly from an interface phenomena. We believe that the DOP_{001} results from the effect of an anisotropic strain field associated with strained bonds at the interfaces of the quantum well. The anisotropic strain field appears to be due to the combination of two factors: (a) the partial As surface coverage at the growth-interrupted, surface-reconstructed interface leading to a mixed As/P interface upon resuming growth of InP and (b) the difference in the amount of Ga across the interfaces. DOP is a sensitive, easy-to-implement technique to probe the interaction of carriers confined in the quantum well with such anisotropic strain. Results indicate that the measured DOP_{001} is strongly dependent on the growth interruption time at the interface requiring an As to P flux change, the quantum well composition and thickness. The observations may be qualitatively understood in terms of a

simple bond counting model. More rigorous numerical simulation has been done to study the propagation of strain into the quantum well due to strained bonds at the interfaces. The model and the simulation results are discussed in the next chapter.

Chapter 5 Valence force field model

5.1 Introduction

The bond-counting model presented in the previous chapter, to analyse the results of anisotropic polarization of photoluminescence, could not explain the linear relationship of DOP_{001} with the reciprocal of the thickness of the quantum well. To understand the experimental results of DOP_{001} , simulations based on a valence force field (VFF) [105] model have been performed by introducing strained bonds at the interfaces of a single quantum well. The simulations predict the difference in the normal components of strain (i.e., $\epsilon_{110} - \epsilon_{\bar{1}\bar{1}0}$, where ϵ_{110} and $\epsilon_{\bar{1}\bar{1}0}$ are the components of strain along [110] and [$\bar{1}\bar{1}0$] directions respectively) in the quantum well and also a shear strain, ($\epsilon_{100} - \epsilon_{010}$), which is two orders of magnitude smaller than $\epsilon_{110} - \epsilon_{\bar{1}\bar{1}0}$. Room-temperature polarization-resolved measurements on thin ($<100\text{\AA}$) quantum wells were used to measure shear strain in quantum wells. In this chapter, details of the numerical simulation and some of the details related to the measurement of shear strain are presented.

From an explanation based on surface-reconstruction, detailed in chapter 4, there is believed to be an asymmetry in the number of strained bonds between the top and bottom interfaces of the quantum well. The bottom interface is thought to consist of In-As bonds, which are directed along [110], and strained In-As and Ga-As bonds along the [$\bar{1}\bar{1}0$]

direction. The top interface is thought to have Ga-As, In-As, and Ga-P bonds directed along $[110]$ direction and In-As bonds along $[1\bar{1}0]$ direction. It has been suggested in the previous chapter that the net effect due to all the strained bonds at the top and bottom interfaces of the quantum well is an anisotropic strain field and that this leads to an anisotropic polarization of luminescence from the quantum well. The total number of strained bonds at the two interfaces can be counted and used in the simulation to compute the net strain in the quantum well.

It has been shown in chapter 2, using a simply-supported beam-bending experiment, that DOP_{001} is proportional to the difference in the strain components along two orthogonal directions.

$$DOP_{001} = -C_{\epsilon} (\epsilon_{110} - \epsilon_{1\bar{1}0}) \quad (5.1)$$

where ϵ_{110} and $\epsilon_{1\bar{1}0}$ are the components of strain along $[110]$ and $[1\bar{1}0]$ directions respectively; $C_{\epsilon} = 37.9 \pm 1.7$ is a calibration constant. Assuming that the model based on partial surface coverage is correct, an estimate of the DOP_{001} of the luminescence from the quantum well may be obtained from Eq. 2 and knowledge of the strain field owing to lattice-mismatched In-As, Ga-As, and Ga-P bonds at the interfaces.

5.2 The Model

A simplified VFF model has been used to compute the distortion of the lattice due

to strained bonds at the interface and investigate the strain field in the quantum well. The model includes only the nearest neighbour interactions. Since the first neighbour interactions are the dominant mechanism affecting the macroscopic photoelastic effect in the material, the second neighbour interactions and the Coloumb forces in zinc-blende structures [106] arising due to cation and anion sublattices have been neglected in this simulation. The VFF approach has been widely used to study phonons in semiconductors, to obtain elastic constants of zinc-blende and wurtzite structures in terms of the force constants [107,108,109]. Recently, an extensive study on the distribution of bond lengths in random semiconductor alloys has been done by Y. Cai & M.F. Thorpe in a series of papers [110,111,112]. Also, the VFF model seems to predict the bond-length distortion in the monolayer limit which is consistent with the x-ray standing wave (XSW) and extended x-ray absorption fine-structure (EXAFS) measurements [113].

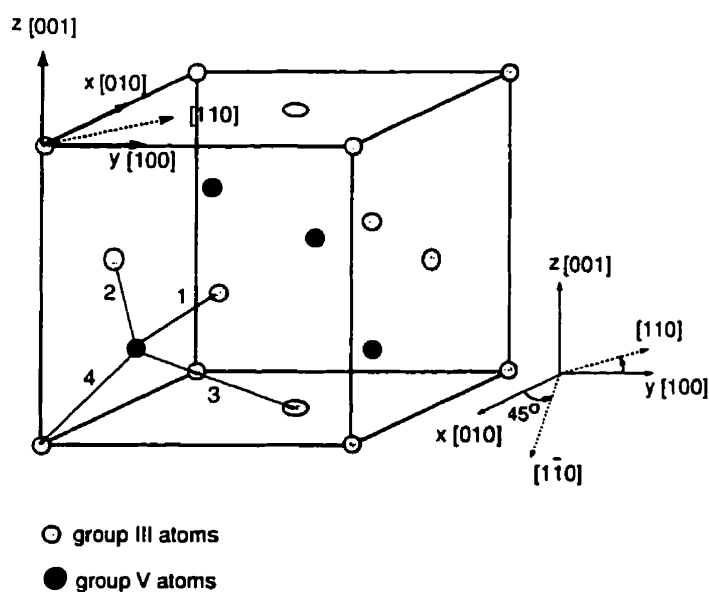


Figure 5.1 Zinc-blende crystal structure showing crystallographic orientations

We considered a three-dimensional zinc-blende structure. The crystal consists of two interpenetrating face-centered cubic lattices with two atoms in a unit cell. The unit cell is considered to be of unit length so that the nearest neighbour distance between two atoms in the undistorted lattice is $\sqrt{3}/4$. Each atom is bonded to four nearest neighbours as shown in Fig. 5.1. The crystallographic orientations are also indicated in Fig. 5.1. In a Cartesian coordinate system, the position of any atom in a unit cell can be described by the x,y,z coordinates of the atom. The total interaction force on any given atom A(x_j, y_j, z_j) due to all the neighbouring atoms should be equal to zero for equilibrium. Hence, in response to any perturbation in the lattice, the atoms tend to move toward an equilibrium position to minimize the energy owing to distortion. Forces on a jth atom due to the four nearest neighbour atoms can be written as

$$F_x(j) = -\sum_{i=1}^4 k_{ji} (\vec{X}_{ji} - \vec{x}_{ji}) \cdot \hat{x} \quad (5.2)$$

$$F_y(j) = -\sum_{i=1}^4 k_{ji} (\vec{Y}_{ji} - \vec{y}_{ji}) \cdot \hat{y} \quad (5.3)$$

$$F_z(j) = -\sum_{i=1}^4 k_{ji} (\vec{Z}_{ji} - \vec{z}_{ji}) \cdot \hat{z} \quad (5.4)$$

where k_{ji} is the force constant of each bond. To a first order approximation, the force constants in all three directions are assumed to be the same and are obtained from the α -parameters for the Kirkwood model [114] tabulated by Cai [112] ($\alpha_{\text{GaP}}/\alpha_{\text{InP}} = 1.15$; $\alpha_{\text{GaAs}}/\alpha_{\text{InP}} = 1.06$; $\alpha_{\text{InAs}}/\alpha_{\text{InP}} = 0.84$). $\mathbf{X}_{ji} = \mathbf{X}_j - \mathbf{X}_i$, $\mathbf{Y}_{ji} = \mathbf{Y}_j - \mathbf{Y}_i$, $\mathbf{Z}_{ji} = \mathbf{Z}_j - \mathbf{Z}_i$ where \mathbf{X}_j , \mathbf{Y}_j , \mathbf{Z}_j are the position vectors of the j th atom after deformation. $\bar{\mathbf{x}}_{ji} = \bar{\mathbf{x}}_j - \bar{\mathbf{x}}_i$, $\bar{\mathbf{y}}_{ji} = \bar{\mathbf{y}}_j - \bar{\mathbf{y}}_i$, $\bar{\mathbf{z}}_{ji} = \bar{\mathbf{z}}_j - \bar{\mathbf{z}}_i$ where $\bar{\mathbf{x}}_j$, $\bar{\mathbf{y}}_j$, $\bar{\mathbf{z}}_j$ are the position vectors of the j th atom in the undistorted lattice. $\hat{\mathbf{x}}$, $\hat{\mathbf{y}}$, $\hat{\mathbf{z}}$ are the unit vectors directed along the edges of the unit cells and $\hat{\mathbf{z}}$ ([001]) is the growth direction. A description of the atomic forces as given in Eqs. 3-5 yields a pocket or well in three dimensional space where the atoms are located in equilibrium. Hence there exists a restoring force to return atoms to equilibrium positions when the radial or angular distances between the central atom and nearest neighbours are perturbed. Also writing forces in terms of the difference between position vectors of two atoms ensures that the structure is invariant under any arbitrary translation or rotation of the crystal as a whole.

To simulate propagation of strain in an InP/InGaAs/InP quantum well we considered a crystal of size ($N_x=2$, $N_y=3$, $N_z=14$) where N_x , N_y , and N_z are the number of unit cells along the x , y , and z directions respectively. Periodic boundary conditions were applied along the x and y directions to create a crystal of infinite size (i.e., if an atom at $x=0$ moves by $\Delta\bar{\mathbf{r}}$, then the corresponding atom at $x=N_x$ must, owing to the assumed symmetry, move by $\Delta\bar{\mathbf{r}}$. A similar condition is imposed in the 'y' direction as well.). Choosing $N_x = 2$ and $N_y = 3$ results in a surface that is large enough to encompass a 2×4 reconstructed interface. The atoms in

the top and bottom surfaces of the crystal were required to remain stationary. This boundary condition is valid in a situation where the thickness of the substrate and the cap layer are many times larger than that of the quantum well. The number of unit cells along the growth direction was increased until no significant change was observed in the strain field within the quantum wells due to the fixing of the positions of the atoms at the top and bottom surfaces of the crystal.

In general, the DOP_{001} of luminescence from a biaxially strained material is zero since the amount of luminescence polarized in two orthogonal directions is equal. For an InP/InGaAs/InP quantum well away from the interfaces, the In-As and Ga-As bonds occur in each direction resulting in a biaxially symmetric strain field and hence no contribution to DOP_{001} . This suggests a simplification that can be used in the simulation. Wherever there is an equal contribution to strain due to In-As and Ga-As bonds along $[110]$ and $[1\bar{1}0]$ directions, the bonds are treated as unstrained InP bonds. Hence, all the bonds within the quantum well are assumed to be In-P bonds. The strained Ga-P, Ga-As and In-As bonds are introduced at the top and bottom interfaces of the quantum well. The strain in each bond is computed from the mismatch in the lattice constant of the corresponding bulk material with reference to InP ($\epsilon_{GaP} = .076$; $\epsilon_{GaAs} = .037$; $\epsilon_{InAs} = -.031$). For small deformation, the net effect of elastic strain on the polarization of luminescence is a linear superposition of the effect of strain on luminescence due to individual strained bonds. Hence, we considered the situation of simulating the strained bonds one at a time at the interface and the effects were added

together in a weighted average depending on the composition of the interface. An iterative numerical procedure was done using Newton's technique to find equilibrium position vectors for all the atoms [115,116]. The simulations were performed on a 133 MHz Pentium machine with 32 MB RAM memory. Each iteration took about 10 minutes to solve and 6 iterations were typically required to obtain the strain field.

5.3 Anisotropy between $[110]$ and $[1\bar{1}0]$ directions

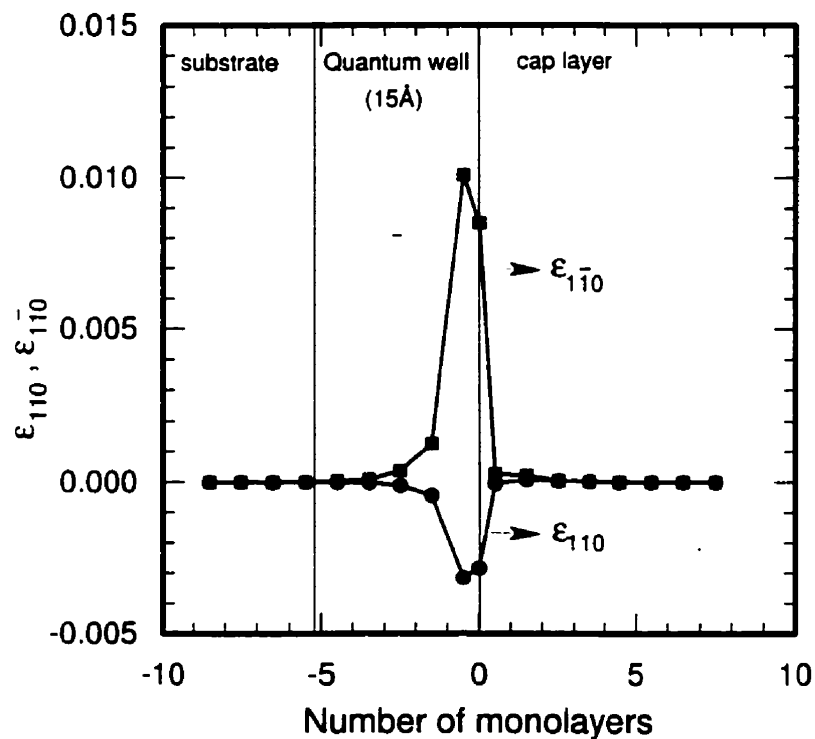


Figure 5.2 Propagation of strain field along $[110]$ and $[1\bar{1}0]$ directions into the quantum well due to a single Ga-P bond per $(N_x \times N_y)$ periodic structure at the interface. The origin for the abscissa corresponds to the group V atomic layer at I_2 .

From the simulation, the propagation of ϵ_{110} and $\epsilon_{1\bar{1}0}$ along the direction of growth due to a single Ga-P bond per $(N_x \times N_y)$ periodic structure at the I_2 interface is plotted in Fig. 5.2. The origin for the x-axis corresponds to the group V atomic layer at the I_2 interface which is the mixed As/P layer. Introducing one Ga-P bond corresponds to an As surface coverage of 92% at the I_2 interface. ϵ_{110} and $\epsilon_{1\bar{1}0}$ are the strains along $[110]$ and $[1\bar{1}0]$ directions respectively. ϵ_{110} and $\epsilon_{1\bar{1}0}$ were calculated by first computing ϵ_{xx} , ϵ_{yy} and ϵ_{zz} . The strain along the 'x' direction due to all the bonds was defined as [64]

$$\epsilon_{xx}(\alpha) = \frac{1}{4(N_x \times N_y)} \sum_{i=1}^{N_m} \sum_{\substack{j=1 \\ i \neq j}}^{N_n} \frac{\hat{x} \cdot (\vec{X}_{ji} - \vec{x}_{ji})}{|\vec{x}_{ji}|}, \quad \alpha = 1 \dots N_a \quad (5.5)$$

where N_n (=4), N_m , N_a are the number of nearest neighbours, number of atoms in an atomic layer and number of atomic layers respectively below the interface and within the quantum well. Similar equations can be written for the strain along the 'y' and 'z' directions. From knowledge of the principal components of strain along the x,y,z directions, the strain along $[110]$ and $[1\bar{1}0]$ directions can be calculated by a coordinate transformation. The anisotropic strain due to a strained bond appears to be mainly an interface phenomenon. The strain decreases rapidly on either side of the interface. The strain decreases from the top (I_2) interface into the quantum well and becomes insignificant (less than $\pm 10^{-6}$) beyond four monolayers (i.e., 8 atomic layers) from the I_2 interface. Similarly, strain becomes insignificant beyond four monolayers from the interface, I_2 , into the cap layer.

The calculations were repeated by introducing In-As and Ga-As strained bonds at the I_1 and I_2 interfaces and the net strain in the material is obtained from the linear superposition of the effects due to Ga-P, Ga-As, and In-As bonds. Based on the explanation given in section II, the InP/ $\text{In}_{0.5}\text{Ga}_{0.5}\text{As}$ interface (I_2), with 75% As surface coverage, consist of 3 Ga-P, 3 In-P, 9 In-As, and 9 Ga-As bonds directed along $[110]$ and 6 In-P and 18 In-As bonds

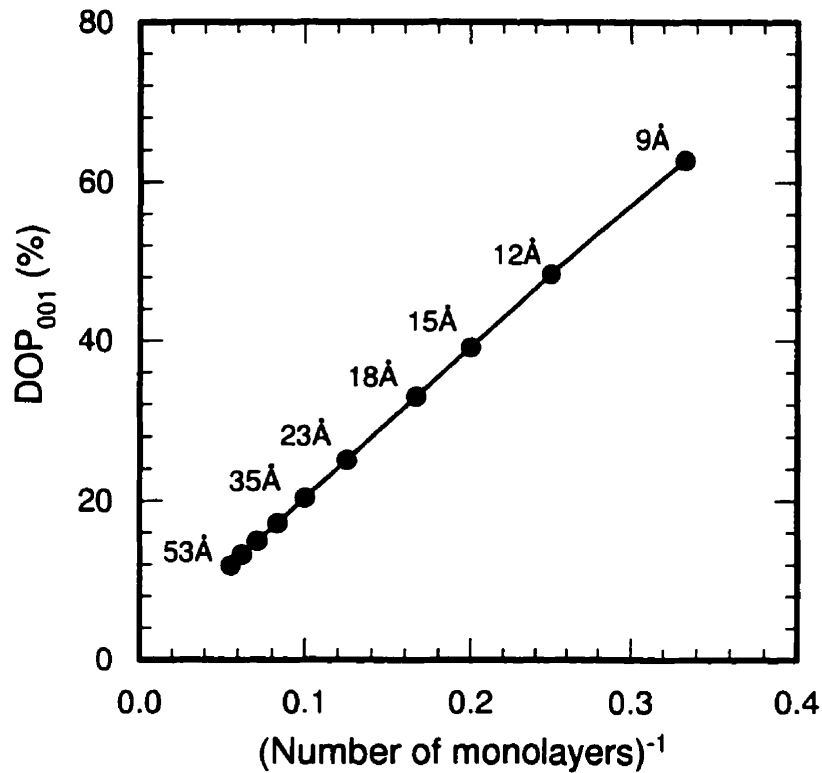


Figure 5.3 Theoretical prediction of variation of DOP_{001} with the inverse of number of monolayers in the quantum well. The thickness of the well shown in the figures is calculated from the distance between two atomic layers = 1.46\AA ($a_{\text{InP}}/4$, where a_{InP} is the lattice constant of InP).

along $[1\bar{1}0]$. The $\text{In}_{0.5}\text{Ga}_{0.5}\text{As}/\text{InP}$ interface (I_1), with 100% As surface coverage, consist of 24 In-As bonds along $[110]$ and 12 Ga-As and 12 In-As bonds along $[1\bar{1}0]$ direction. Assuming the photoluminescence is produced uniformly from the entire quantum well, the effect of strain on the photoluminescence from the quantum well can be computed from the weighted average of strain over the number of atomic layers within the quantum well. DOP_{001} can be estimated by substituting the calculated net strain into Eq. 5.2. Figure 5.3 is a plot of the calculated DOP_{001} versus the reciprocal of the number of monolayers below the interface. The data indicates that the impact of this anisotropic strain is larger for the thinner wells where the strength of the perturbation from the interfaces on the electron and hole wavefunction is larger due to the fact that the relative volume of the interfacial perturbation with respect to the quantum well increases. This results in a linear increase in the calculated DOP_{001} as the inverse of the thickness of the quantum well ($1/L$) increases. The sign of the calculated DOP_{001} and the trend of the calculated DOP_{001} with $1/L$ are in agreement with our observations using polarization-resolved photoluminescence.

The simulations also indicate that the effects due to Ga-As and In-As bonds directed along $[110]$ and $[1\bar{1}0]$ directions at both the interfaces almost cancel each other and that the major contribution to the DOP arises from the Ga-P bonds which have the largest mismatch in bond length and force constant with reference to InP. It is also important to mention that the value of the calculated DOP_{001} for a quantum well of thickness of 22\AA (distance between two atomic layers is taken as 1.46\AA) due to a single Ga-P bond per $(N_x \times N_y)$ periodic

structure is 5.7% if the force constants are assumed to be the same for all the bonds. This is approximately 50% smaller than when the force constant for Ga-P was taken to be 1.15 times that of In-P. Hence, the polarization anisotropy seems to be sensitive to the value of the force constants. These results confirm the qualitative predictions of the bond-counting model (c.f. Eq. 4.9 in chapter 4) that DOP_{001} may be sensitive to the stiffness of the bond and the contribution from the Ga-P bonds may be the dominant factor.

5.4 Anisotropy between [100] and [010] directions

An anisotropy between [100] and [010] directions (referred as shear strain) was calculated at each atomic layer using the numerical simulation and was defined [64] as

$$\gamma_{xy}(\alpha) = \frac{1}{4(N_x \times N_y)} \sum_{i=1}^{N_m} \sum_{\substack{j=1 \\ i \neq j}}^{N_n} \left(\frac{\hat{x} \cdot (\vec{X}_{ji} - \vec{x}_{ji})}{|\vec{y}_{ji}|} + \frac{\hat{y} \cdot (\vec{Y}_{ji} - \vec{y}_{ji})}{|\vec{x}_{ji}|} \right), \quad \alpha = 1 \dots N_a \quad (5.6)$$

where γ_{xy} is the shearing strain between the planes xz and yz. Similar to ϵ_{110} and $\epsilon_{1\bar{1}0}$, γ_{xy} is also an interfacial effect as illustrated in Fig.5.4. The propagation of shear strain along the direction of growth due to a single Ga-P bond per $(N_x \times N_y)$ periodic structure at the interface I_2 is plotted in Fig. 5.4. This corresponds to an As coverage of 92% at the I_2 interface. The shear strain diminishes on either side of the interface and becomes less than 1×10^{-6} beyond 4 monolayers (i.e., 8 atomic layers). The shear strain summed over all atoms in the quantum well is approximately equal to the value at the interface owing to a single strained bond per $(N_x \times N_y)$ periodic structure at the interface. Also, comparing Figs. 5.2 and 5.4, it should be

noted that $(\epsilon_{100} - \epsilon_{010})$ is two orders of magnitude smaller than $(\epsilon_{110} - \epsilon_{\bar{1}\bar{1}0})$. Hence, we believe that the principal axes for the stress owing to the strained bonds at the interfaces are along $[110]$ and $[\bar{1}\bar{1}0]$ directions. This shear strain may be due to an inherent anisotropic structure, $[(N_x \times N_y) = (2 \times 3)]$, that is considered in the model.

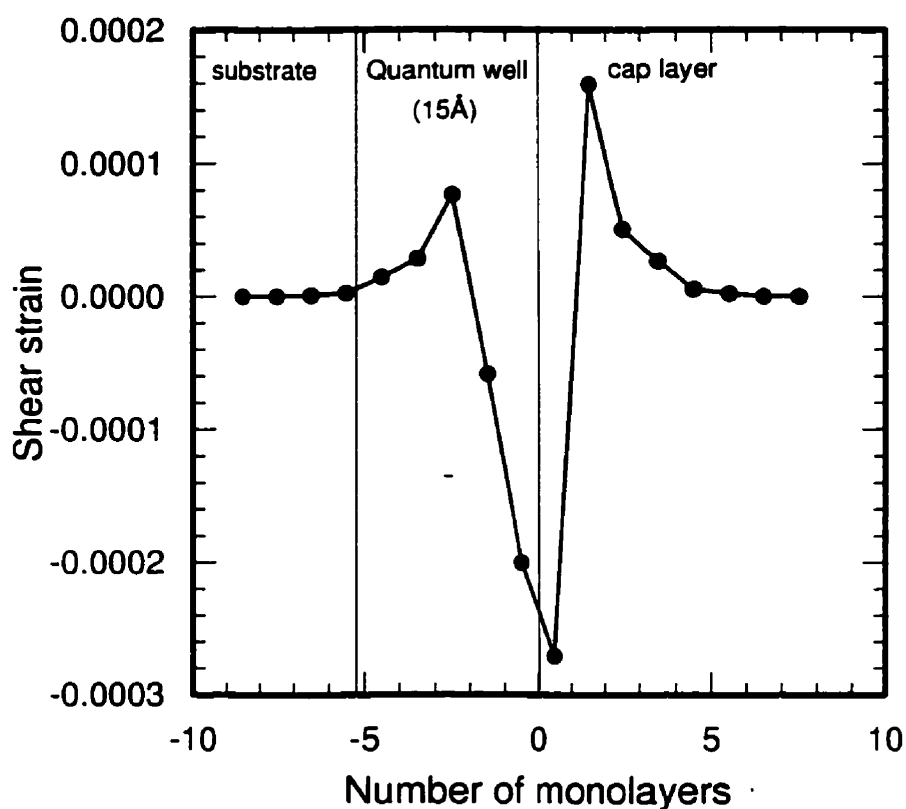


Figure 5.4 Propagation of shear strain into the quantum well and the cap layer due to a single Ga-P bond per $(N_x \times N_y)$ periodic structure at the well/cap layer interface. The origin for the abscissa corresponds to the group V atomic layer at I_2 interface.

It is possible to measure rotated degree of polarization of luminescence, which quantifies shear strain in the material, using polarization-resolved photoluminescence measurements on quantum wells [34]. From the calibration experiments using a beam-bending technique on bulk InP samples with etched V-Grooves, ROP_{001} can be related to the shear strain in the material and is given by

$$ROP_{001} = 2C_{\gamma} \gamma_{xz} \quad (5.8)$$

where γ_{xz} is the shear strain between the planes 'xy' and 'zy' and C_{γ} ($= -11.5 \pm 1.0$) is a

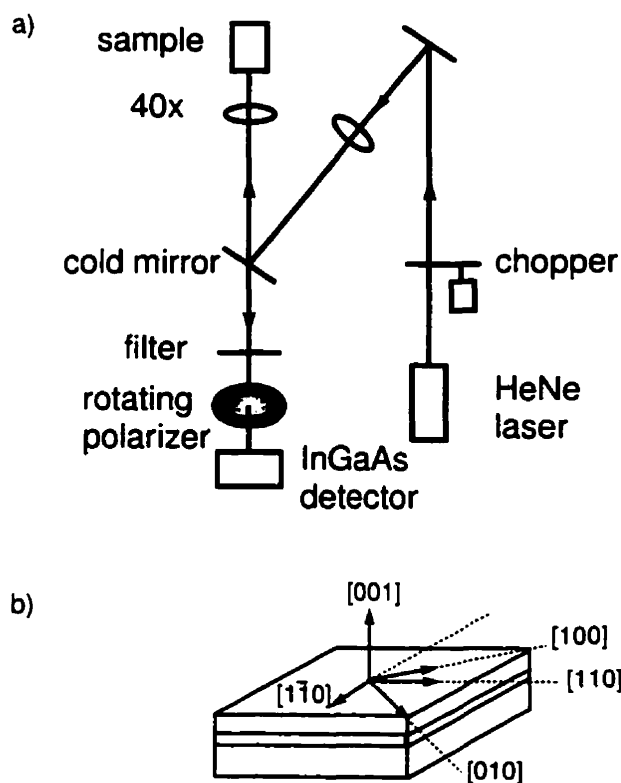


Figure 5.5 a) Experimental apparatus for polarization-resolved photoluminescence measurements. b) The crystallographic orientations of the sample.

calibration parameter. Figure 5.5a is a schematic of the experimental apparatus used for the polarization-resolved photoluminescence measurements. The samples were excited by a He-Ne laser that was passed through a chopper. Both the excitation and collection were along a [001] direction. A rotating linear polarizer was used to separate L_{110} , $L_{\bar{1}\bar{1}0}$, L_{100} , and L_{010} . The crystallographic orientations of the sample are indicated in Fig.5.5b. Care was taken to align the [110] direction of the sample to be parallel to the polarization axis of the polarizer within a fraction of a degree using a clinometer [117]. Demodulation of the output of the photodiode by phase sensitive detectors at the frequency of the chopper yields $(L_{110} + L_{\bar{1}\bar{1}0})$ and at twice the rate of rotation of the polarizer gives $(L_{110} - L_{\bar{1}\bar{1}0})$, and $(L_{100} - L_{010})$, for the in-phase and quadrature components. We define a parameter rotated degree of polarization of luminescence, ROP_{001} , as

$$ROP_{001} = \frac{\int_0^{\infty} [L_{100}(E) - L_{010}(E)] R(E) dE}{\int_0^{\infty} [L_{100}(E) + L_{010}(E)] R(E) dE} \quad (5.7)$$

where L_{100} and L_{010} are the magnitudes of the luminescence polarized along the [100] and [010] directions respectively. The maximum ROP_{001} of 1.5 percentage points was observed for the case of a 20Å-thick, 1% tensile strained InP/InGaAs/InP quantum well with a growth interruption time of 2 minutes at the top interface. The details of the structure of the sample and the growth conditions are given in the previous chapter. An ROP_{001} of 1.5 percentage points corresponds to a shear strain of 6.0×10^{-4} . This small magnitude of shear strain is consistent with the prediction from the model suggesting that the principal components of

stress are along $[110]$ directions. However, this anisotropy may be an important factor in quantum wells grown on mis-oriented substrates.

5.5 Summary

The results of the simulations indicate a net anisotropic strain between $[110]$ and $[1\bar{1}0]$ directions due to strained bonds at the interface and that the strain is mainly an interface phenomenon. The strain decreases rapidly into the quantum well and is less than $\pm 10^{-6}$ beyond 4 monolayers below the interface. This confirms the linear relationship of the anisotropic strain and hence DOP_{001} with the inverse of the number of monolayers within the quantum well. The model also predicts the propagation of shear strain into the quantum well due to strained bonds at the interface. A typical shear strain of the order of 10^{-4} was measured using polarization-resolved photoluminescence technique. Hence measurements of DOP_{001} and ROP_{001} combined with VFF modelling suggest that these degree of polarization techniques will be useful quantitative probes of anisotropic features at the interfaces of InP/InGaAs/InP quantum wells.

Chapter 6. Future Work and Conclusion

6.1 Suggested future work

The work on characterization of quantum wells using DOP has opened up an interesting area of research in the field of analyzing and characterizing strained quantum wells.

It was demonstrated in chapter 3 that the parameter degree of polarization of luminescence is a measure of the relative strength of TE and TM polarized luminescence. I believe that DOP may be analyzed to give information about the in-plane band dispersion especially in the case of thin quantum wells where c-hh is the dominating transition. By varying λ , the wavelength of the source of excitation, $DOP(\lambda)$ may be a measure of the overlap of the heavy hole and light hole wavefunction at an electron \mathbf{k} vector away from the zone center. This can be achieved by changing the source of excitation from He-Ne to a tunable wavelength source. This extension of the present apparatus will improve the sensitivity of the measurements while retaining its simplicity. Since our present knowledge of the valence band mixing in quantum wells is limited to theory, this may be a useful exercise. Also, the overlap function is an important factor for lower dimensional structures even at $\mathbf{k} = 0$ and in strained materials.

The capability to probe smaller dimensions of the order of 10\AA suggests a vast potential usage of this technique for analyzing and characterizing lower-dimensional structures. In chapter 3, it was demonstrated that the introduction of quantum confinement in one dimension increased the DOP of edge emission from 0.2 percentage points in bulk material to values up to 70 percentage points in quantum wells. This concept can be extended to higher-dimensional quantum confined structures such as quantum wires and quantum dots. Measurement of DOP of photoluminescence emitted near different crystallographic orientations can give information regarding the confinement of the motion of carriers in each direction. However, it is important to filter the effects due to anisotropic strain in the material. It may be possible to separate the effect due to size and strain by taking the calibration of DOP for known uniaxial strain presented in chapter 2 and the variation of DOP with thickness of the quantum wells presented in chapter 3 as a guideline for higher-dimensional quantum confined structures.

Another factor which is important for quantum wells is the effect of guiding associated with heterostructures. Calculations based on a ray tracing approach for guided modes can explain the effect of wave-guiding on the degree of polarization of luminescence.

It is very interesting to note that the macroscopic luminescence technique is very sensitive to atomic scale variations at the interfaces. The observation of an anisotropy in the polarization of photoluminescence between $[110]$ and $[1\bar{1}0]$ directions suggests many possibilities for future work. This may have a bearing on the performances of ridge

waveguide lasers with ridges oriented along $[110]$ or $[1\bar{1}0]$ directions. As a first step, the effect can be tested by fabricating waveguides in two orthogonal directions.

It is not clear whether there is an anisotropy in the electrical conductance even though initial measurements on resistivity did not show any anisotropy. A detailed electrical measurement is necessary to test this concept which can be done by i) fabricating Hall bar configuration oriented along two orthogonal directions and ii) fabricating Metal-semiconductor field-effect transistors (MESFETs) with gate oriented along the two directions and measuring the transconductance of the transistors. A difference in the mobility of 15% between $[110]$ and $[1\bar{1}0]$ directions has been reported by Ramvall et. al.[118] in $\text{Ga}_{0.25}\text{In}_{0.75}\text{As}/\text{InP}$ quantum wells. They have speculated that the anisotropy may be due to a spontaneous ordering forming a CuPt crystal structure (similar to GaInP) or In-rich stripes. It will be interesting to measure the mobility in our samples to test our hypothesis.

Since the measurement of DOP appears to be a sensitive measure of the interfacial features, the technique can be used to study the electric field at the interfaces. The electric field at the interfaces may arise owing to doping, asymmetric heterostructures, or an external electric field. Probing of the effects of electric field at the interfaces is an important phenomena to obtain information regarding the band offset in heterostructures.

Initial experiments were done to reduce DOP_{001} using ion-implantation (section 4.5). However, the results presented in this thesis have not been analyzed in detail. It can be a

separate project by itself to understand what may be going on due to ion-implantation. Another growth-related experiment that can be tried to reduce the DOP_{001} is to grow a monolayer of Indium at the interfaces thereby reducing the formation of Ga-P and Ga-As bonds. It has been reported that growth of a monolayer of In reduces the interfacial strain. However, the effect on anisotropic strain field is not yet known which can be tested using our technique.

The capability to measure shear strain in quantum wells brings in new features that can be studied using this technique. Eventhough, the shear strain measured in the set of samples reported in this thesis is small, it may be an important factor in quantum wells grown on vicinal substrates where higher values of shear strain is expected [119]. However, I feel that a better theoretical understanding on the effect of shear strain on the band structure, electrical, and optical properties of quantum wells can guide us for future work.

Finally, the code for the valence force field model is not an optimum one. Solving a system of N linear equations requires a storage space of $(N \times N)$. This puts a restriction on the number of unit cells that can be simulated. However, as mentioned in chapter 5, each atom is connected to only four other atoms. Hence the $(N \times N)$ matrix is a sparse matrix. An ordered numbering scheme on atoms (nodes) as it is done in a Finite Element technique, can result in a banded matrix. Also, the matrix is symmetric in our problem. The bandedness, sparseness, and symmetry of the matrix can be utilized to the advantage of efficient storing which will increase the speed as well as the possibility of increasing the thickness of the

material under consideration.

6.2 Conclusion

The results reported in this thesis have clearly demonstrated how a simple and easy-to-perform technique has the potential to be a versatile characterization tool for probing semiconductor heterostructures.

It is well known that the polarization properties of edge emission from quantum wells are highly anisotropic. This specific property can be utilized to characterize quantum wells for their thickness and strain using two methods. It is mainly the polarization-resolved spectral technique that is commonly used by many groups [refs. From Ch.3] and not the integrated polarization-resolved photoluminescence (DOP). However, there is a convincing evidence from this project work that the parameter Degree of polarization of luminescence (DOP) is more sensitive to the relative strength of c-hh and c-lh transitions compared to the spectral shift that can be observed at room-temperature. To my knowledge, this is the first time a room-temperature, polarization-resolved integrated photoluminescence technique has been used to characterize quantum wells.

An interesting observation in this work is the anisotropic polarization of photoluminescence between $[110]$ and $[1\bar{1}0]$ directions (DOP_{001}) for InP/InGaAs/InP quantum wells grown on (001) oriented substrates. The observations were related to an anisotropic strain field that is associated with the anisotropic strained bonds at the interfaces of the

quantum wells. Initially, it was difficult to believe that the atomic scale interfacial features were being probed using a macroscopic technique. However, as we proceeded with our systematic approach in designing the experiments, it was possible for us to predict the trend of DOP_{001} with the variation in the conditions of growth.

It is well-known that in zinc-blende structures, the bonds below and above any (001) plane are directed along two orthogonal directions (i.e., $[110]$ and $[1\bar{1}0]$). Hence, we expected that the introduction of even a single strained bond along one direction can result in an anisotropic strain field and hence to DOP_{001} . A simple bond-counting model presented in chapter 4 and a numerical simulation based on valence force field presented in chapter 5 predict an anisotropic strain field in the quantum wells due to strained bonds at the interfaces.

Eventhough both optical anisotropy between $[110]$ and $[1\bar{1}0]$ directions and interfacial strain have been observed in InP/InGaAs/InP quantum wells, they have not been correlated to each other. I believe that our measurement of anisotropic polarization of photoluminescence and its correlation to the strain field are important observations since the strain field alters the electrical and optical properties of devices.

The measurement of shear strain in quantum wells is an important step towards understanding the effect of interfaces on the optical properties of quantum wells. The simultaneous measurement of DOP and ROP clearly demonstrates that the technique is an efficient tool to characterize low-dimensional features even at room-temperature.

Chapter 7. Appendices

7.1 Appendix A

Program to calculate strained quantum well confined energy levels.

Calculates C and V confined energy levels. Both Van Wijngaarden-Dekker-Brent and secant methods work equally well. The following is for secant method. For Brent, refer to my old programs. The strain includes the in-built strain arising due to lattice-mismatch as well as an additional external biaxial/uniaxial strain. This 'QWCEL.EXE' includes 'define.for', 'initiate.for', 'Readin.for' (for inputs), 'FBCEL.for' (computes Finite Barrier Confined Energy Levels—Use either secant or Zbrent -ref. [116] and 'Matpar.for' (Material parameters for InGaAsP/InGaAsP/InGaAsP strained layers.

```
-----  
      program QWCEL  
      implicit none  
      Include 'define.for'  
      open(1, file='bandpar.dat',access='sequential', status='unknown')  
      call READIN  
      call INITIATE  
      call MATPAR(xw,yw,xb,yb,eV_meV, H,S,St,epar,GapW,GapB,bar,massIn,massOut,G1,G2,G3)  
      call Energies      ! get confined energy states in the conduction and valence bands  
      close(1)  
      end  
-----
```

```
-----  
      SUBROUTINE Energies  
      implicit none  
      include 'Define'  
      real*8  Estart  
      integer n,limit  
      Estart=0d0  
      limit=0  
      do n=1,maxCdim      !Conduction band ; In-in the well; Out- barrier  
  
      call FBCEL(n,massIn(3),massOut(3),Lz,bar(3),Estart,0)  
      Ec(n)=Estart  
      if (Ec(n).ne.-1d6) then  
        write(*,*) n,real(Ec(n)),'(meV)'  
        numC=n  
      else  
        limit=1  
        exit  
      endif  
      end do  
      if (limit.eq.0) then  
        write(*,*) 'If necessary, increase maxCdim'  
      endif  
-----
```

```

Estart=0d0
numHH=0
limit=0
do n=1,maxHHdim           ! Heavy Hole energy levels

  CALL FBCEL(n,massIn(1),massOut(1),Lz,bar(1),Estart,0)

  Ehh(n,1)=Estart
  if (Ehh(n,1).ne.-1d6) then
    write(*,*) n,real(Ehh(n,1)),'(meV)'
    numHH=n
  else
    limit=1
    exit
  endif
end do

if (limit.eq.0) then
  write(*,*) 'If necessary, increase maxHHdim'
endif

Estart=0d0
numLH=0
limit=0
do n=1,maxLHdim           ! Light Hole energy levels

  CALL FBCEL(n,massIn(2),massOut(2),Lz,bar(2),Estart,0)

  Elh(n,1)=Estart
  if (Elh(n,1).ne.-1d6) then
    Elh(n,1)=Elh(n,1) + St    ! correct for strain
    write(*,*) n,real(Elh(n,1)),'(meV)'
    numLH=n
  else
    limit=1 ! if flag not set, maxLHdim has been reached
    exit
  endif

end do

if (limit.eq.0) then
  write(*,*) 'If necessary, increase maxLHdim '
endif
return
end

```

```

include 'FBCEL'
include 'READIN'

```

```
include 'PARAM'
include 'INITIATE'
```

```
-----
SUBROUTINE MATPAR(xw,yw,xb,yb,eV_meV,
& Htot,S,St,epar,GapW,GapB,bar,
& massIn,massOut,G1,G2,G3)
-----
```

c Strained InGaAsP/InGaAsP QW Band Parameter Subroutine
c Calculates band parameters for $\text{In}(1-x)\text{Ga}(x)\text{As}(y)\text{P}(1-y) / \text{In}(1-x)\text{Ga}(x)\text{As}(y)\text{P}(1-y)$ strained quantum wells.

```
xw  Gallium mole fraction in well;      yw  As mole fraction in well
xb  Ga mole fraction in the barrier     yb  As mole fraction in the barrier
Temp temperature (not used)           eV_meV  0-output in eV, 1-output in meV
epar  In-built biaxial strain + external strain
```

```
Htot  hydrostatic component of band gap shift;   S  splitting energy for valence band
St    total split between HH and LH band; e    percent mismatch of well compared to bar
GapW  strained InGaAsP band gap (in well)
GapB  LM/strained InGaAsP band gap in the barrier (out of well)
bar(1,2,3) potential barrier in hh,lh,c band
massIn(1,2,3) masses in well: 1-hh, 2-lh, 3-c
massOut(1,2,3) masses in barrier: 1-hh, 2-lh, 3-c
g1(1,2), g2(1,2), g3(1,2) Luttinger Parameters: 1-in well,2-barrier
```

```
implicit none
real*8  xw,yw,xb,yb
real*8  Htot,S,St,epar,GapW,GapB,bar(3)
real*8  massIn(3),massOut(3)
real*8  G1(2),G2(2),G3(2)
integer eV_meV
real*8  Hc,Hv,atot,ac,b
real*8  C11,C12,abar,aw,D
integer error
real*8  equ1,equ2,equ3,equ4,equ5,equ1a,equ3a
real*8  equ11,equ21,equ31,equ41,equ51,equ11a,equ31a
real*8  delec,delev
```

! If xw, and yw are known then compute aw, abar and epar

```
aw= ((1d0-xw)*yw*6.0583d0)+((1d0-xw)*(1d0-yw)*5.8688d0)+
* (xw*yw*5.6533d0)+(xw*(1d0-yw)*5.4512d0)
```

```
abar= ((1d0-xb)*yb*6.0583d0)+((1d0-xb)*(1d0-yb)*5.8688d0)+
* (xb*yb*5.6533d0)+(xb*(1d0-yb)*5.4512d0)
```

```

write(*,*)'Lattice constants(barrier,well)=' , real(abar),real(aw)

! I have used the Lattice constant of InP (5.8688 A) instead of abar. Evenif the barrier is strained, if the layer
is not relaxed, then the in-plane lattice parameter is the same as that of the substrate. Hence, the strain in the
well can be computed w.r.to the substrate lattice parameter. If the barrier is thick and is relaxed, then compute
abar. For example, GaAs/Si where a thick GaAs is grown that is completely relaxed and use that buffer layer
as the virtual substrate.

epar = epar + (5.8688-aw)/aw      ! Total strain

! If composition of the well is not given, but the PI wavelength and the strain in the well are known, then
CALL det_comp

call eff_mass(xb,yb,mcB,mlhb,mhhb,G1,G2,G3)
    massOut(1)= mhhb      ! heavy hole mass in the barrier
    massOut(2)= mlhb      ! light hole mass in the barrier
    G1(2) = G1
    G2(2) = G2
    G2(3) = G3
call eff_mass(xw,yw,mcw,mlhw,mhhw,G1,G2,G3)
    massIn(1)= mhhw      ! heavy hole mass in the well
    massIn(2)= mlhw      ! light hole mass in the well
    G1(1) = g1
    G1(2) = G2
    G1(3) = G3
call band_offset(xw,yw,vo,vov1,vov2)
    Bar(1) = vov1
    Bar(2) = vov2
    Bar(3) = vo
call band_gap(xw,yw,gapW)
call band_gap(xb,yb,gapB)
Call def_coef(x,y,Htot,S,Vc,Vhh,Vlh,St)

! Convert energies from eV to meV (if desired)
if (eV_meV.eq.1) then
    Htot = Htot*1d3
    S = S*1d3
    St= St*1d3
    GapW = GapW*1d3
    GapB = GapB*1d3
    bar(1)=bar(1)*1d3
    bar(2)=bar(2)*1d3
    bar(3)=bar(3)*1d3
endif

epar = 100d0*epar      ! convert strain mismatch to percent
print *,'strain(%)=' ,epar

```

```

return
end

```

```

-----
SUBROUTINE eff_mass(x,y,mc,mlh,mhh,G1,G2,G3)
real mc,mlh,mhh
! Calculate Luttinger Parameters for well region (from Landolt-Bornstein)
! (From Jack's thesis-high-lighted numbers in the table)

G1=((1d0-x)*y*(19.67d0))+((1d0-x)*(1d0-y)*(6.28d0))+ (x*y*(7.65d0))+ (x*(1d0-y)*(4.2d0))
G2=((1d0-x)*y*(8.37d0))+((1d0-x)*(1d0-y)*(2.08d0))+ (x*y*(2.41d0))+ (x*(1d0-y)*(0.98d0))
G3=((1d0-x)*y*(9.29d0))+((1d0-x)*(1d0-y)*(2.76d0))+ (x*y*(3.28d0))+ (x*(1d0-y)*(1.66d0))

mhh = 1d0/(G1-2d0*G2)      ! heavy hole mass
mlh = 1d0/(G1+2d0*G2)      ! light hole mass
mc=((1-x)*y*0.027)+((1-x)*(1-y)*0.08)+(x*y*0.067)+ (x*(1-y)*0.17) ! Electron mass
! fit using mc(InAs)=0.027, mc(InP)=0.08, mc(GaAs)=0.067; mc(GaP)=0.17 (from Adachi, 1992)
return
end

```

```

-----
SUBROUTINE elastic_const(x,y,c11,c12)
real c11,c12
c11=((1-x)*y*8.329)+((1-x)*(1-y)*10.22)+(x*y*11.81)+ (x*(1-y)*14.12)
c12=((1-x)*y*4.526)+((1-x)*(1-y)*5.76)+(x*y*5.32)+ (x*(1-y)*6.253)
return
end

```

```

-----
SUBROUTINE press(x,y,av,ac,b,D)
real ep,ip
real epar,eg,lz
common /coefs/ lz,xb,yb,epar,eg
ep=((1-x)*y*10.2)+((1-x)*(1-y)*7.5)+(x*y*12.6)+(x*(1-y)*9.7)
ip=((1-x)*y*2.9)+((1-x)*(1-y)*2.3)+(x*y*2.5)+ (x*(1-y)*2.1)
a=((1-x)*y*(-6.0))+((1-x)*(1-y)*(-8.0))+ (x*y*(-9.43))+ (x*(1-y)*(-9.9))

call elastic_const(x,y,c11,c12)
c a=(c11+2*c12)*ep/3
stress=((c11-c12)/c11)*epar
c av=(2*ip*stress)/3
c ac=a-av
ac=2*a/3
av=a/3
b=((1-x)*y*(-1.8))+((1-x)*(1-y)*(-1.55))+ (x*y*(-1.7))+ (x*(1-y)*(-1.5))
D=((1d0-x)*y*(0.41d0))+((1d0-x)*(1d0-y)*(0.1d0))+ (x*y*(0.384d0))+ (x*(1d0-y)*(0.13d0))
return
end

```

```

-----
SUBROUTINE def_coef(x,y,deltaeh,deltaes,vc,vhh,vlh,St)
common /coefs/ lz,xb,yb,epar,eg

```

```

real lz,epar,eg
real vc,vhh,vlh
call elastic_const(x,y,c11,c12)
call press(x,y,av,ac,b)
deltaech=2*ac*((c11-c12)/c11)*epar
deltaevh=2*av*((c11-c12)/c11)*epar
deltaeh=deltaech+deltaevh      ! Total Hydrostatic
deltaes=-2*b*((c11+2*c12)/c11)*epar ! So called shear
S = deltaes
vc=deltaech
vhh=deltaevh+deltaes/2        !HH bandgap shift
vvh=deltaevh-deltaes/2       !LH bandgap shift
St=S + (S+D)/2d0 - (D/2d0)*dsqrt(1d0 - 2d0*S/D + 9d0*S**2/D**2)
!total HH-LH energy split including SO-- Refer--Thesis of Corzine

return
end

```

```

SUBROUTINE band_offset(x,y,p1,p2,p3)
common /coefs/ lz,xb,yb,epar,eg
common /comp/ xw,yw
real lz,epar,eg
real ebgap,ewgap
call band_gap(xb,yb,ebgap)
call band_gap(xw,yw,ewgap)
call def_coef(x,y,deltaeh,deltaes,vc,vhh,vlh)
! Assume Band-offset ratio between CB and VB to be 40:60
delec=0.4*(ebgap-ewgap)
delev=0.6*(ebgap-ewgap)
p1=delec-vc      ! Conduction band
p2=delev-vhh     ! Heavy Hole
p3=delev-vlh     ! Light Hole
return
end

```

```

FUNCTION f7(x)
real epar,eg,xw,yw,lz
common/lattice/abarrier
common /comp/ xw,yw
common /coefs/ lz,xb,yb,epar,eg
aw=5.8688/(1+epar)
f7=0.4176*x-0.01255*x*yw-0.1895*yw-5.8688+aw
return
end

```

```

SUBROUTINE band_gap(x,y,bgap)
c Det. unstrained bulk band gap by the interpolation of
c four ternary alloys
real equ1,equ2,equ3,equ4,equ5

```

```

if (x.eq.0.and.y.eq.0)then
  bgap=1.35-0.72*y+0.12*y**2
else
  equ1=x*(1-x)*(1-y)*(1.35+0.643*x+0.786*x**2)
  equ2=x*(1-x)*y*(0.36+0.505*x+0.555*x**2)
  equ3=y*(1-y)*(1-x)*(1.35-1.083*y+0.091*y**2)
  equ4=y*(1-y)*x*(2.74-1.473*y+0.146*y**2)
  equ5=(x*(1-x))+(y*(1-y))
  bgap=(equ1+equ2+equ3+equ4)/equ5
endif
return
end

```

SUBROUTINE READIN

c The inputs are Lz,xw,yw,epar(ext strain),xb,yb,Temp

```

implicit none
include 'Define'

integer      numData,i
parameter    (numData=7)
real*8      v(numData)
open(7,file='read.dat',action='read')
  ! read material parameters

do i=1,6
  read(7,*)
end do

do i=1,7
  v(i)=-1d6
  read(7,*)
  read(7,*,end=10) v(i)
  read(7,*)
  if (v(i).eq.-1d6) then
    print *, 'error reading data item ',i
    pause
  endif
end do

Lz =v(1)
xw =v(2)
yw =v(3)
xb =v(4)

```

```

yb =v(5)
Epar =v(6)
Temp =v(7)

write(*,*) 'Well width (A):      ',real(Lz)
write(*,*) 'Gallium mole fraction: ',real(xw)
write(*,*) 'Arsenic mole fraction: ',real(yw)
write(*,*) 'Barrier Ga mole fraction: ',real(xb)
write(*,*) 'Barrier As mole fraction: ',real(yb)
write(*,*) 'Strain :              ',real(epar)
101 format(a,E10.4,a1,$)
    goto 20

20  close(7)
    return
    end

```

c-----
DOP.FOR

Only the subroutine to compute DOP is given. Call this routing from the main program. For calculating the matrix elements, followed the same approach as that of Ref. [92] and Ph.d Thesis of Corzine

Calculates TE and TM components of spon. emission and then DOP

Assumes that electron k vector is along 'z' direction. (Ref. Section 3.4)

The gain is first found as a function of k and then is converted to a dependence on energy using linear extrapolation to calculate spon. Emission (Used the method described by Corzine...used the routine from his files)

SUBROUTINE DOP

implicit none

include 'Define'

```

real*8  E(maxEdim),kT,E1,strength
real*8  dEc,dEv,fermiC,fermiV,DOS,kPL
real*8  dEcdk,dEvdk
real*8  HHmassIn,HHmassOut,LHmassIn,LHmassOut
real*8  mR,mHH,mLH,mC,confRatio
integer  i,j,k,m
real*8  ATE,ATM,MaxErr
real*8  PLTE,PLTM
real*8  E2
Double precision PL(2,1001)
Double precision DOP

```

open(14,file='PLE.dat')

strength = mass*(19.7d3+5.6d3*yAs)/2d0 ! Matrix element for InGaAsP

```

do j=1,maxGdim
  do i=1,2      ! 1 and 2 for TE and TM
    Pl(i,j)=0d0    ! Spon. Emission as a function of k
    pl(i,j)=0d0    ! Spon. Emission as a function of E
  end do
  E(j)=-1d6
end do

do i=1,numC      ! calculate c-HH emission
  do j=1,numHH
    print *, 'numC=',i, 'numHH=',j
    kT=0d0

    do k=1,maxEdim-1

      dEc = Ec(i) + (kT**2)*normalize/massC(i)
      dEv = Ehh(j,k)
      E(k) = GapW + dEc + dEv

      if (( (dEv+dEc).gt.(Estop-Ebegin) ).or.(dEv.eq.-1d6)) then
        Pl(1,k)=-1d6
        pl(2,k)=-1d6
        E(k)=-1d6
        exit
      endif

      if ((MtHH(1,i,j,k).eq.0d0).and.(MtHH(2,i,j,k).eq.0d0)) then
        pl(1,k)=pl(2,k) = 0d0
        goto 50
      endif

      fermiC = 1d0/( 1d0 + dexp((dEc-Efc)/kTemp) )
      fermiV = 1d0/( 1d0 + dexp(-(dEv-Efv)/kTemp) )
      if (k.eq.1) then
        dEvdk = ( Ehh(j,k+1) - Ehh(j,k) )/kinc
      else
        dEvdk = ( Ehh(j,k+1) - Ehh(j,k-1) )/(2d0*kinc)
      endif
      dEcdk = 2d0*kT*normalize/massC(i)

      if ( kT.eq.0d0 .and. dEvdk.eq.0d0 ) then
        DOS = 1d0/(2d0*pi*Lz)/(2d0*normalize/massC(i))
      else
        DOS = kT/(2d0*pi*Lz)/(dEcdk + dEvdk)
      endif

      Pl(1,k)= (E(k))*DOS*strength*MtHH(1,i,j,k)*fermiC* (1d0-fermiV)
      pl(2,k)= (E(k))*DOS*strength*MtHH(2,i,j,k)*fermiC* (1d0-fermiV)
    end do
  end do
end do

```

! Prefactors not included. They get cancelled while calculating DOP

```

50      kT=kT+kinc
      end do
      CALL Linearize(E)      !For transformation from k-space to E-space, ref. Corzine, Ph.d Thesis
      end do

      do j=1,numLH          ! C-LH transitions
      kT=0d0
      do k=1,maxEdim-1

          dEc = Ec(i) + (kT**2)*normalize/massC(i)
          dEv = Elh(j,k)
          E(k) = GapInd + dEc + dEv

          if (( (dEv+dEc).gt.(Estop-Ebegin) ).or.(dEv.eq.-1d6)) then
              PL(1,k)=-1d6
              PL(2,k)=-1d6
              E(k)=-1d6
              exit
          endif

          if ((MtLH(1,i,j,k).eq.0d0).and.(MtLH(2,i,j,k).eq.0d0)) then
              PL(1,k)=PL(2,k) = 0d0
              goto 60
          endif

          fermiC = 1d0/( 1d0 + dexp((dEc-Efc)/kTemp) )
          fermiV = 1d0/( 1d0 + dexp(-(dEv-Efv)/kTemp) )

          if (k.eq.1) then
              dEvdk = ( Elh(j,k+1) - Elh(j,k) )/kinc
          else
              dEvdk = ( Elh(j,k+1) - Elh(j,k-1) )/(2d0*kinc)
          endif
          dEcdk = 2d0*kT*normalize/massC(i)

          if ( kT.eq.0d0 .and. dEvdk.eq.0d0 ) then
              DOS = 1d0/(2d0*pi*Lz)/(2d0*normalize/massC(i))
          else
              DOS = kT/(2d0*pi*Lz)/(dEcdk + dEvdk)
          endif

          Pl(1,k)= (E(k))*DOS*strength*MtHH(1,i,j,k)*fermiC* (1d0-fermiV)
          pl(2,k)= (E(k))*DOS*strength*MtHH(2,i,j,k)*fermiC* (1d0-fermiV)

60      kT=kT+kinc
      end do

```

```

CALL Linearize(E)
end do
end do

Est=Ebegin
do m = 1,numG
  SponTE(m) = PLE(1,m)
  SponTM(m) = PLE(2,m)
  Est=Est+Einc
end do

call area2(SponTE,numG,Einc,ATE,MaxErr) ! Gets the area under the curve
call area2(SponTM,numG,Einc,ATM,MaxErr)
print *,'Area before 3D',ATE,ATM
DOP = (ATE-ATM)/(ATE+ATM)
print *,'DOP before 3D and before convolution',DOP

close(14)
return
end

```

```

SUBROUTINE Linearize(E)

```

```

implicit none
include 'Define'

real*8 E(1),E1,w
integer i,j
E1=Ebegin
i=1
j=1

if (E(1).eq.-1d6) goto 100

while (E1.lt.E(1)) do
  E1=E1+Einc
  j=j+1
end while

while (j.lt.numG) do

  while (E1.gt.E(i+1)) do
    if (E(i+1).eq.-1d6) exit
    i=i+1
  end while
  if (E(i+1).eq.-1d6) exit

  w=(E1-E(i))/(E(i+1)-E(i))

```

```
PLE(1,j)=PLE(1,j) + (1d0-w)*PL(1,i) + w*PL(1,i+1)
PLE(2,j)=PLE(2,j) + (1d0-w)*PL(2,i) + w*PL(2,i+1)

write(14,11)real(Est),PLE(1,m),PLE(2,m)
11 format(G10.4,2x,G10.4,2x,G10.4)
E1=E1+Einc
j=j+1
end while
100 return
end
```

7.2 Appendix B

program vff model

This program is for a diamond/zinc-blende structure with periodic boundary conditions on LEFT-RIGHT and FRONT-BACK of the crystal and TOP & BOTTOM surfaces fixed. Each atom is bonded to four nearest neighbour atoms. Bonds are treated like springs and at equilibrium, the force on each atom should be equal to zero. Newton-Raphson method was used to solve the set of non-linear systems of equations.

```

PARAMETER (Nr = 1651)
Integer Atom
c Dimension A(Nr,Nr),Alu(Nr,Nr)
Dimension A(Nr,Nr)
Dimension X(Nr), y(Nr), z(Nr)
Double Precision xyz(Nr),xyzold(Nr),B(Nr)
Dimension r(Nr),copyr(Nr)
Dimension bondL(Nr,4),bondS(Nr,4)
Dimension EvenIII(Nr),OddIII(Nr)
Dimension ang(Nr,3,6)
Integer Ic(Nr,4),Icon(4)
real jhold,xd,yd,zd
COMMON /initial1/x,y,z
COMMON /initial2/xyz,xyzold
COMMON /connect/Ic,bondL,bondS,BondK
COMMON /atom/Np,Npts,NTotalC,NtotalBT,NTotalLR,NGIII,NGV
COMMON /out/B
COMMON Nci,Ncj,Nck
c COMMON /Jac/A,Alu
COMMON /Jac/A
COMMON /tetra/ ang
Integer At1,At2,At3,At4,At
Integer Ant1,Ant2,Ant3,IAD

open (unit = 3,file = 'strain.dat')

c      Number of unit cell in x,y,z directions = (Nci-1), (Ncj-1), and (Nck-1) respectively
Nci = 4;   Nck = 3;   Ncj = 15      ! Ncj corresponds to the thickness of the layer
c      Projection of Equilibrium Bond lengths in all three directions of an undistorted lattice and Stiffness
      constants

BL1 = BL2 = 0.25   ! 1,2 refer to In-As and Ga-As bonds; But treated here as InP (Refer chapter 5 for
                  an explanation)
sc1 = sc2 = 1.0

c      Construct a 3D zinc-blend lattice

```

- c Define Group III atoms
 $At1 = Nci$
 $At2 = 1 + (Ncj-1)*Nci$
 $At3 = 1 + (Nck-1)*Ncj*Nci$
 $At4 = Nci*Ncj*Nck$
- c Define corner atoms
do k = 1,Nck
do j = 1,Ncj
do i = 1,Nci
 $Atom = (j-1)*Nci + (k-1)*Nci*Ncj + i$
 $x(Atom) = float(i)$
 $y(Atom) = float(j)$
 $z(Atom) = float(k)$
end do
end do
end do
NTotalC = Atom
- c Define Bottom/Top face-centered atoms
do k = 1,(Nck-1)
do j = 1,Ncj
do i = 1,(Nci-1)
 $Atom = NTotalC + (j-1)*(Nci-1) + (k-1)*(Nci-1)*Ncj + i$
 $x(Atom) = float(i) + 0.5$
 $y(Atom) = float(j)$
 $z(Atom) = float(k) + 0.5$
end do
end do
end do
NtotalBT = Atom
- c Define Left/Right face-centered atoms
do k = 1,(Nck-1)
do j = 1,(Ncj-1)
do i = 1,Nci
 $Atom = NTotalBT + (j-1)*Nci + (k-1)*Nci*(Ncj-1) + i$
 $x(Atom) = float(i)$
 $y(Atom) = float(j) + 0.5$
 $z(Atom) = float(k) + 0.5$
end do
end do
end do
NtotalLR = Atom
- c Define Front/Back face-centered atoms
do k = 1,Nck
do j = 1,(Ncj-1)

```

do i = 1,(Nci-1)
  Atom = NtotalLR + (j-1)*(Nci-1) + (k-1)*(Nci-1)*(Ncj-1) + i
  x(Atom) = float(i) + 0.5
  y(Atom) = float(j) + 0.5
  z(Atom) = float(k)
end do
end do
end do

```

```

NGIII = Atom

```

c Define Gr. V atoms

```

do i = 1,NGIII
  xd = x(i) + 0.25
  yd = y(i) + 0.25
  zd = z(i) + 0.25
  if ((xd .le. float(Nci)).and. (yd .le. float(Ncj)) .and. (zd .le. float(Nck)))then
    Atom = Atom + 1
    x(Atom) = xd
    y(Atom) = yd
    z(Atom) = zd
  end if
end do

```

```

Np = Atom
Npts = 3*Np
NGV = Np - NGIII

```

```

do i = 1, Np
  xyz(i) = x(i)
  xyz(i+Np) = y(i)
  xyz(i+2*Np) = z(i)
end do
print*, 'Npts=', Npts

```

c Store the Equilibrium distances

```

do i = 1, Npts
  xyzold(i) = xyz(i)
end do

```

c find the nearest neighbour distance

c Atoms [1 to Np] correspond to Gr.III and [(Np+1) to 2*Np] correspond to Gr. V

c Find the distance between one Gr. V atom to all the Gr.III atoms and

c Introduce connectivity (Bonds) between Gr. V and 4 nearest neighbour Gr.III atoms

```

do i = 1, Np
  do L = 1, 4
    Ic(i, L) = 0
  end do
end do

```

```

    end do
  end do

  do i = 1,Np
    execute findNN

c   sort the bonds as 'Bonds looking up' and 'down'

    do L = 1,4
      Na = Icon(L)
      if (Na .ne.0) then
        x1 = x(i) - x(Na)
        y1 = y(i) - y(Na)

c   Ic(i,m), m=1-->Top right; 2-->Top left;3-->Bottom right;4-->Bottom left

        if ((x1.lt.0.) .and. (y1.lt.0.))then
          Ic(i,1) = Na
        else if ((x1.gt.0.) .and. (y1.lt.0.))then
          Ic(i,2) = Na
        else if ((x1.lt.0.) .and. (y1.gt.0.))then
          Ic(i,3) = Na
        else if ((x1.gt.0.) .and. (y1.gt.0.))then
          Ic(i,4) = Na
        end if
      end if
    end do
  end do

-----
remote block findNN
c   Compute the distance between atom 'i'(Gr.V) and all other Np (Gr. III) atoms

    do j = 1,Np
      if (j .eq. i) goto 15
      x1 = x(i) - x(j)
      y1 = y(i) - y(j)
      z1 = z(i) - z(j)
      r(j) = sqrt(x1**2 + y1**2 + z1**2)
      copyr(j) = r(j)
15    continue
    end do

c   Sort the distance computed above in ascending order
    do j = 1,Np-1
      m = j+1
25    if (r(j) .le. r(m) .and. r(j) .gt. 0.0) then
        continue
      else

```

```

    jhold = r(j)
    r(j) = r(m)
    r(m) = jhold
  end if
  m = m+1
  if (m .le. Np) goto 25
end do

```

- c define connectivity between ith atom and first 4 nearest neighbour 'j' atoms
 c $Ic(i,m=1,4)$ suggests the bond between atom 'i' and atom $Ic(i,m)$

```

do m = 1,4
  Icon(m) = 0
end do

m = 1
do k = 1,Np
  if(copyr(k) .eq. r(m) .and. copyr(k) .lt. 0.5) then
    Icon(m) = k
    m = m + 1
  end if
  if (m .gt. 4) quit
end do
end block

```

c-----
 c Boundary conditions

- c I. Corner 8 atoms are identical; Therefore assigned same neighbours

```

At1 = 1
At2 = Nci + (Nck-1)*Nci*Ncj
At3 = 1 + (Ncj-1)*Nci + (Nck-1)*Nci*Ncj
At4 = Nci + (Ncj-1)*Nci
At5 = Nci
At6 = 1 + (Ncj-1)*Nci
At7 = 1 + (Nck-1)*Ncj*Nci
At8 = Nci*Ncj*Nck

```

```

Ic(At1,2) = Ic(At2,2)
Ic(At1,3) = Ic(At3,3)
Ic(At1,4) = Ic(At4,4)

```

```

do k = 1,Nck,(Nck-1)
  do j = 1,Ncj,(Ncj-1)
    do i = 1,Nci,(Nci-1)
      At = i + (j-1)*Nci + (k-1)*Nci*Ncj
      do L = 1,4
        Ic(At,L) = Ic(At1,L)
      end do
    end do
  end do
end do

```

```

end do
end do
end do

```

c II. Atoms in the outer faces having two bonds; Periodic condition

c a) Atoms in the Front and Back faces

```

do j = 2,(Ncj-1)
do i = 2,(Nci-1)
  At1 = i + (j-1)*Nci
  At2 = i + (j-1)*Nci + (Nck-1)*Nci*Ncj
  Ic(At1,2) = Ic(At2,2)
  Ic(At1,3) = Ic(At2,3)
  Ic(At2,1) = Ic(At1,1)
  Ic(At2,4) = Ic(At1,4)
end do
end do

```

c b) Atoms in the Left and Right faces

```

do k = 2,(Nck-1)
do j = 2,(Ncj-1)
  At1 = 1 + (j-1)*Nci + (k-1)*Nci*Ncj
  At2 = Nci + (j-1)*Nci + (k-1)*Nci*Ncj
  Ic(At2,1) = Ic(At1,1)
  Ic(At2,3) = Ic(At1,3)
  Ic(At1,2) = Ic(At2,2)
  Ic(At1,4) = Ic(At2,4)
end do
end do

```

c c) Atoms in the Bottom and Top Faces

```

do k = 2,(Nck-1)
do i = 2,(Nci-1)
  At1 = i + (k-1)*Nci*Ncj
  At2 = i + (Ncj-1)*Nci + (k-1)*Nci*Ncj
  Ic(At2,1) = Ic(At1,1)
  Ic(At2,2) = Ic(At1,2)
  Ic(At1,3) = Ic(At2,3)
  Ic(At1,4) = Ic(At2,4)
end do
end do

```

c III. Atoms on the faces having single bonds; Periodicity is introduced by comparing

c the atoms in planes perpendicular to three axes

c a) planes perpendicular to 'j' axis

```

do j = 2,(Ncj-1)
  At1 = 1 + (j-1)*Nci
  At2 = Nci + (j-1)*Nci + (Nck-1)*Nci*Ncj

```

```

At3 = 1 + (j-1)*Nci + (Nck-1)*Nci*Ncj
At4 = Nci + (j-1)*Nci
Ic(At1,2) = Ic(At2,2)
Ic(At1,3) = Ic(At3,3)
Ic(At1,4) = Ic(At4,4)

do L = 1,4
  Ic(At2,L) = Ic(At3,L) = Ic(At4,L) = Ic(At1,L)
end do
end do

```

c b) planes perpendicular to 'k' axis

```

do k = 2,(Nck-1)
  At1 = 1 + (k-1)*Nci*Ncj
  At2 = Nci + (k-1)*Nci*Ncj
  At3 = 1 + (Ncj-1)*Nci + (k-1)*Nci*Ncj
  At4 = Nci + (Ncj-1)*Nci + (k-1)*Nci*Ncj
  Ic(At1,2) = Ic(At2,2)
  Ic(At1,3) = Ic(At3,3)
  Ic(At1,4) = Ic(At4,4)

  do L = 1,4
    Ic(At2,L) = Ic(At3,L) = Ic(At4,L) = Ic(At1,L)
  end do
end do

```

c c) planes perpendicular to 'i' axis

```

do i = 2,(Nci-1)
  At1 = i
  At2 = i + (Nck-1)*Nci*Ncj
  At3 = i + (Ncj-1)*Nci + (Nck-1)*Nci*Ncj
  At4 = i + (Ncj-1)*Nci
  Ic(At1,2) = Ic(At2,2)
  Ic(At1,3) = Ic(At3,3)
  Ic(At1,4) = Ic(At4,4)

  do L = 1,4
    Ic(At2,L) = Ic(At3,L) = Ic(At4,L) = Ic(At1,L)
  end do
end do

```

c IV. The face-centered atoms are periodic

c Bottom/Top face-centered atoms

```

do k = 1,(Nck-1)
  do i = 1,(Nci-1)
    NBott = Ntotalc + i + (k-1)*(Nci-1)*Ncj
    NTop = Ntotalc + i + (Ncj-1)*(Nci-1) + (k-1)*Ncj*(Nci-1)
    Ic(NBott,3) = Ic(NTop,3)
  end do
end do

```

```

    Ic(NBott,4) = Ic(NTop,4)
    Ic(NTop,1) = Ic(NBott,1)
    Ic(NTop,2) = Ic(NBott,2)
  end do
end do

c Left/Right face-centered atoms
do k = 1,(Nck-1)
do j = 1,(Ncj-1)
  Nleft = NtotalBT + 1 + (j-1)*Nci + (k-1)*Nci*(Ncj-1)
  Nright = NtotalBT + Nci + (j-1)*Nci + (k-1)*Nci*(Ncj-1)
  Ic(Nleft,2) = Ic(Nright,2)
  Ic(Nleft,4) = Ic(Nright,4)
  Ic(Nright,1) = Ic(Nleft,1)
  Ic(Nright,3) = Ic(Nleft,3)
end do
end do

c Front/Back face-centered atoms
do j = 1,(Ncj-1)
do i = 1,(Nci-1)
  Nfront = NtotalLR + i + (j-1)*(Nci-1)
  Nback = NtotalLR + i + (j-1)*(Nci-1) + (Nck-1)*(Nci-1)*(Ncj-1)
  Ic(Nback,1) = Ic(Nfront,1)
  Ic(Nback,4) = Ic(Nfront,4)
  Ic(Nfront,2) = Ic(Nback,2)
  Ic(Nfront,3) = Ic(Nback,3)
end do
end do

c The top and bottom surfaces of the structure are fixed
do i = 1,Np
  if (y(i) .eq. 1.0 .or. y(i) .eq. Ncj) then
    Ic(i,3) = -Ic(i,1)
    Ic(i,4) = -Ic(i,2)
  end if
end do

```

Stiffness parameters BONDS(i,L) refer to the spring constants of the springs connected between Atom 'i' and the neighbouring atom 'Na = Ic(i,L)'

sc1-->stiffness of InAs bond; sc2---> stiffness of GaAs

Define Even # of Gr.III atoms to be In and Odd # of Gr. III atoms to be Ga; all Gr. V are 'As'. This sets the composition to be In_{0.5}Ga_{0.5}As. I have treated all bonds to be equivalent to In-P bonds wherever there are equal # of bonds looking up and looking down.

```

do k = 1,NGIII
  if(mod(k,2) .eq.0) then
    i = i+1
  end if
end do

```

```

EvenIII(i) = k
do L = 1,4
  BondL(k,L) = BL1
  BondS(k,L) = sc1
end do
else
j = j+1
OddIII(j) = k
do L = 1,4
  BondL(k,L) = BL2
  BondS(k,L) = sc2
end do
end if
end do

do k = (NGIII+1),Np
do L = 1,4
  Na = abs(Ic(k,L))
  do i = 1,NGIII
    if (Na .eq. EvenIII(i)) then
      BondL(k,L) = BL1
      BondS(k,L) = sc1
    else
      BondL(k,L) = BL2
      BondS(k,L) = sc2
    end if
  end do
end do
end do

```

c Introduce a single strained bond at the interface

IAD = 380

```

ant1 = Ic(IAD,3)
ant2 = Ic(ant1,4)
do k = 1,Np
do L=1,4
  if (k.eq.IAD .and. L.eq.3) then
    bondL(k,L) = 0.258
    bondS(k,L) = 0.8411
  elseif (k.eq.ant1 .and. L.eq.2) then
    bondL(k,L) = 0.258
    bondS(k,L) = 0.8411
  end if
end do
end do

```

```

2  CALL newton

21  FORMAT (i3,3(F10.6,2x))
    do i = 1,Np
      write(3,21)i,xyz(i),xyz(i+Np),xyz(i+2*Np)
    end do
    CALL STRAIN
    CLOSE (2)
    CLOSE(3)
    end

c-----
      SUBROUTINE length(k,L,warn,x1,y1,z1)
c-----
    PARAMETER (Nr = 1651)
    Dimension X(Nr),Y(Nr),Z(Nr)
    Double Precision xyz(Nr),xyzold(Nr)
    Dimension coord(Nr)
    Integer Ic(Nr,4)
    Dimension BondL(Nr,4),BondS(Nr,4),BondK(Nr,4)
    Common /connect/Ic,bondL,bondS,BondK
    Common /initial1/x,y,z
    COMMON /initial2/xyz,xyzold
    COMMON /atom/ Np,Npts,NTotalC,NtotalBT,NtotalLR,NGIII,NGV
    COMMON Nci,Ncj,Nck
    Integer At1,At2,At
    Integer warn

    NN = Ic(k,L)
    Na = abs(NN)
    kcop = k

    if (warn .eq. 1) then
      do i = 1,Npts
        coord(i) = xyzold(i)
      end do
    else if (warn .eq.0) then
      do i = 1,Npts
        coord(i) = xyz(i)
      end do
    end if

    x1 = coord(k) - coord(Na)
    y1 = coord(k+Np) - coord(Na+Np)
    z1 = coord(k+2*Np) - coord(Na+2*Np)

c  I. Corner 8 atoms are identical; Therefore assigned same neighbours
do k1 = 1,Nck,(Nck-1)
do j1 = 1,Ncj,(Ncj-1)

```

```

do il = 1,Nci,(Nci-1)
  At = il + (j1-1)*Nci + (k1-1)*Nci*Ncj
if (k .eq. At) then

  SELECT CASE (L)
  CASE (1)
    x1 = coord(At) - (coord(Na) + (i1-1))
    y1 = coord(At+Np) - (coord(Na+Np) + (j1-1))
    z1 = coord(At+2*Np) - (coord(Na+2*Np) + (k1-1))
  CASE (2)
    x1 = coord(At) - (coord(Na) - (Nci -i1))
    y1 = coord(At+Np) - (coord(Na+Np) + (j1-1))
    z1 = coord(At+2*Np) - (coord(Na+2*Np) - (Nck - k1))
  CASE (3)
    x1 = coord(At) - (coord(Na) + (i1-1))
    y1 = coord(At+Np) - (coord(Na+Np) - (Ncj - j1))
    z1 = coord(At+2*Np) - (coord(Na+2*Np) - (Nck - k1))
    if (NN .lt. 0) then
      y1 = -coord(At+Np) + (coord(Na+Np) + (j1-1))
      z1 = -coord(At+2*Np) + (coord(Na+2*Np) + (k1-1))
    end if
  CASE (4)
    x1 = coord(At) - (coord(Na) - (Nci - i1))
    y1 = coord(At+Np) - (coord(Na+Np) - (Ncj -j1))
    z1 = coord(At+2*Np) - (coord(Na+2*Np) + (k1-1))
    if (NN .lt. 0) then
      y1 = -coord(At+Np) + (coord(Na+Np) + (j1-1))
      z1 = -coord(At+2*Np) + (coord(Na+2*Np)-(Nck - k1))
    end if
  END SELECT

end if
end do
end do
end do

```

c II. Atoms in the outer faces having two bonds; Periodic condition

c a) Atoms in the Front and Back faces

```

do j1 = 2,(Ncj-1)
do il = 2,(Nci-1)
  At1 = il + (j1-1)*Nci
  At2 = il + (j1-1)*Nci + (Nck-1)*Nci*Ncj
if (k .eq. At1 .or. k.eq. At2) then
  z1 = coord(k+2*Np) - coord(Na+2*Np)
if (k .eq. At1) then

  if (L.eq.2 .or. L.eq.3)
$      z1 = coord(At1+2*Np) - (coord(Na+2*Np)-(Nck-1))

```

```

else if (k .eq. At2) then

    if (L.eq.1 .or. L.eq.4)
$       z1 = coord(At2+2*Np) - (coord(Na+2*Np)+(Nck-1))
    end if
    x1 = coord(k) - coord(Na)
    y1 = coord(k+Np) - coord(Na+Np)
    end if
end do
end do

c) b) Atoms in the Left and Right faces
do k1 = 2,(Nck-1)
do j1 = 2,(Ncj-1)
    At1 = 1 + (j1-1)*Nci + (k1-1)*Nci*Ncj
    At2 = Nci + (j1-1)*Nci + (k1-1)*Nci*Ncj

    if (k.eq.At1 .or. k.eq.At2) then
        x1 = coord(k) - coord(Na)
        if (k.eq.At1) then
            if (L.eq.2 .or. L.eq.4) x1 = coord(At1) - (coord(Na) - (Nci-1))
        else if (k.eq.At2) then
            if(L.eq.1 .or. L.eq.3) x1 = coord(At2) - (coord(Na) + (Nci-1))
        endif
        y1 = coord(k+Np) - coord(Na+Np)
        z1 = coord(k+2*Np) - coord(Na+2*Np)
    end if
end do
end do

c) c) Atoms in the Bottom and Top Faces
do k1 = 2,(nck-1)
do i1 = 2,(Nci-1)
    At1 = i1 + (k1-1)*Nci*Ncj
    At2 = i1 + (Ncj-1)*Nci + (k1-1)*Nci*Ncj

    if (k.eq.At1 .or. k.eq.At2) then
        x1 = coord(k) - coord(Na)
        y1 = coord(k+Np) - coord(Na+Np)
        z1 = coord(k+2*Np) - coord(Na+2*Np)
        if (k.eq.At1) then
            if (L.eq.3 .or. L.eq.4) then
                y1 = -coord(k+Np) + coord(Na+Np)
                z1 = -coord(k+2*Np) + coord(Na+2*Np)
            end if
        else if (k.eq.At2) then
            if (L.eq.1 .or. L.eq.2) then
                y1 = coord(k+Np) - (coord(Na+Np) + (Ncj-1))
            end if
        end if
    end if
end do
end do

```

```

else if (L.eq.3 .or. L.eq.4) then
  y1 = -coord(k+Np) + (coord(Na+Np) + (Ncj-1))
  z1 = -coord(k+2*Np) + coord(Na+2*Np)
end if
end if
end if
end do
end do

c III. Atoms on the faces having single bonds; Periodicity is introduced by comparing
c the atoms in planes perpendicular to three axes
c a) planes perpendicular to 'j' axis
do j1 = 2,(Ncj-1)
do k1 = 1,Nck,(Nck-1)
do i1 = 1,Nci,(Nci-1)
At = i1 + (j1-1)*Nci + (k1-1)*Nci*Ncj
if (k .eq. At) then
y1 = coord(k+Np) - coord(Na+Np)

SELECT CASE(L)
CASE(1)
x1 = coord(k) - (coord(Na)+(i1-1))
z1 = coord(k+2*Np) - (coord(Na+2*Np) + (k1-1))
CASE(2)
x1 = coord(k) - (coord(Na) - (Nci-i1))
z1 = coord(k+2*Np) - (coord(Na+2*Np) - (Nck-k1))
CASE(3)
x1 = coord(k) - (coord(Na)+(i1-1))
z1 = coord(k+2*Np) - (coord(Na+2*Np) - (Nck-k1))
CASE (4)
x1 = coord(k) - (coord(Na) - (Nci-i1))
z1 = coord(k+2*Np) - (coord(Na+2*Np) + (k1-1))
END SELECT
end if
end do
end do
end do

c b)planes perpendicular to 'k' axis
do k1 = 2,(Nck-1)
do j1 = 1,Ncj,(Ncj-1)
do i1 = 1,Nci,(Nci-1)
At = i1 + (j1-1)*Nci + (k1-1)*Nci*Ncj

if (k .eq. At) then
z1 = coord(k+2*Np) - coord(Na+2*Np)

SELECT CASE(L)

```

```

CASE(1)
  x1 = coord(k) - (coord(Na) + (i1-1))
  y1 = coord(k+Np) - (coord(Na+Np) + (j1-1))
CASE(2)
  x1 = coord(k) - (coord(Na) - (Nci - i1))
  y1 = coord(k+Np) - (coord(Na+Np) + (j1-1))
CASE(3)
  x1 = coord(k) - (coord(Na) + (i1-1))
  y1 = -coord(k+Np) + (coord(Na+Np) + (j1-1))
  z1 = -coord(k+2*Np) + coord(Na+2*Np)
c   y1 = coord(k+Np) - (coord(Na+Np) - (Ncj-j1))
CASE (4)
  x1 = coord(k) - (coord(Na) - (Nci-i1))
  y1 = -coord(k+Np) + (coord(Na+Np) + (j1-1))
  z1 = -coord(k+2*Np) + coord(Na+2*Np)
c   y1 = coord(k+Np) - (coord(Na+Np) - (Ncj-j1))
END SELECT

  end if
end do
end do
end do

c c) planes perpendicular to 'i' axis
do i1 = 2,(Nci-1)
do k1 = 1,Nck,(Nck-1)
do j1 = 1,Ncj,(Ncj-1)
  At = i1 + (j1-1)*Nci + (k1-1)*Nci*Ncj

  if (k .eq. At) then
    x1 = coord(k) - coord(Na)

  SELECT CASE(L)
  CASE(1)
    y1 = coord(k+Np) - (coord(Na+Np) + (j1-1))
    z1 = coord(k+2*Np) - (coord(Na+2*Np) + (k1-1))
  CASE(2)
    y1 = coord(k+Np) - (coord(Na+Np) + (j1-1))
    z1 = coord(k+2*Np) - (coord(Na+2*Np) - (Nck-k1))
  CASE(3)
    y1 = -coord(k+Np) + (coord(Na+Np) + (j1-1))
    z1 = -coord(k+2*Np) + (coord(Na+2*Np) + (k1-1))
c   y1 = coord(k+Np) - (coord(Na+Np) - (Ncj-j1))
c   z1 = coord(k+2*Np) - (coord(Na+2*Np) - (Nck-k1))
  CASE (4)
    y1 = -coord(k+Np) + (coord(Na+Np) + (j1-1))
    z1 = -coord(k+2*Np) + (coord(Na+2*Np) - (Nck-k1))

```

```

c          y1 = coord(k+Np) - (coord(Na+Np) - (Ncj-j1))
c          z1 = coord(k+2*Np) - (coord(Na+2*Np) + (k1-1))
          END SELECT

          end if
        end do
      end do
    end do

c IV. The face-centered atoms are periodic
c Bottom/Top face-centered atoms
do k1 = 1,(Nck-1)
do i1 = 1,(Nci-1)
do j1 = 1,Ncj,(Ncj-1)
  At = NtotalC + i1 + (j1-1)*(Nci-1) + (k1-1)*Ncj*(Nci-1)
  if (k .eq. At) then
    x1 = coord(k) - coord(Na)
    z1 = coord(k+2*Np) - coord(Na+2*Np)

    if (L.eq.1 .or. L.eq.2) y1 = coord(k+Np) - (coord(Na+Np) + (j1-1))
    if (L.eq.3 .or. L.eq.4) then
      y1 = -coord(k+Np) + (coord(Na+Np) + (j1-1))
      z1 = -coord(k+2*Np) + coord(Na+2*np)
    end if
  end if
end do

end do
end do
end do

c Left/Right face-centered atoms
do k1 = 1,(Nck-1)
do j1 = 1,(Ncj-1)
do i1 = 1,Nci,(Nci-1)
  At = NtotalBT + i1 + (j1-1)*Nci + (k1-1)*Nci*(Ncj-1)

  if (k.eq.At) then
    y1 = coord(k+Np) - coord(Na+Np)
    z1 = coord(k+2*Np) - coord(Na+2*Np)

    if (L.eq.2 .or. L.eq.4) then
      x1 = coord(k) - (coord(Na) - (Nci-i1))
    else if (L.eq.1 .or. L.eq.3) then
      x1 = coord(k) - (coord(Na) + (i1-1))
    end if
  end if

end if
end do

```

```

end do
end do

c Front/Back face-centered atoms
do j1 = 1,(Ncj-1)
do i1 = 1,(Nci-1)
do k1 = 1,Nck,(Nck-1)
  At = NtotalLR + i1 + (j1-1)*(Nci-1) + (k1-1)*(Nci-1)*(Ncj-1)
  if (k .eq. At) then
    x1 = coord(k) - coord(Na)
    y1 = coord(k+Np) - coord(Na+Np)

    if (L.eq.2 .or. L.eq.3) z1 = coord(k+2*Np) - (coord(Na+2*Np) - (Nck-k1))
    if (L.eq.1 .or. L.eq.4) z1 = coord(k+2*Np) - (coord(Na+2*Np) + (k1-1))

  end if
end do
end do
end do
return
end

```

SUBROUTINE FORCE

```

c Computes Total Force on each atom in all three directions

PARAMETER (Nr = 1651)
c Dimension A(Nr,Nr),Alu(Nr,Nr)
Dimension A(Nr,Nr)
Dimension x(Nr),y(Nr),z(Nr)
Double Precision xyz(Nr),xyzold(Nr),B(Nr)
Integer Ic(Nr,4)
Dimension BondL(Nr,4),BondS(Nr,4),ang(Nr,6,3),BondK(Nr,4)
COMMON /initial1 /x,y,z
COMMON /initial2/ xyz,xyzold
COMMON /connect /Ic,bondL,bondS,BondK
COMMON /atom/ Np,Npts,NtotalC,NtotalBT,NtotalLR,NGIII,NGV
COMMON /out/B
COMMON Nci,Ncj,Nck
c COMMON /Jac/A,Alu
COMMON /Jac/A
COMMON /tetra/ang

tetrang = DACOS(dble(-1.0/3.0))

do k = 1,Np
  Tx = Ty = Tz = 0.
  TXtheta = TYtheta = TZtheta = 0.0

```

```

do L = 1,4
  NN = Ic(k,L)
  Na = abs(NN)

  if(Na .ne.0) then
    CALL length(k,L,0,x1N,y1N,z1N)
    execute findF
    Tx = Tx + Fx
    Ty = Ty + Fy
    Tz = Tz + Fz
  end if
end do
B(k) = Tx
B(k+Np) = Ty
B(k+2*Np) = Tz
end do
remote block findF
Be = bondL(k,L)
Bk = bondS(k,L)
BeL = sqrt(3*(Be**2))
Bex = sign(1.0,x1N)*Be
Bey = sign(1.0,y1N)*Be
Bez = sign(1.0,z1N)*Be

tN = x1N**2 + y1N**2 + z1N**2
t2N = sqrt(tN)
t3 = Be/t2N
Fx = (x1N - t3*x1N)*Bk
Fy = (y1N - t3*y1N)*Bk
Fz = (z1N - t3*z1N)*Bk

end block
return
end

```

SUBROUTINE JACOB

c Computes dF/dx, dF/dy, and dF/dz

PARAMETER (Nr = 1651)

c Dimension A(Nr,Nr),Alu(Nr,Nr)

Dimension A(Nr,Nr)

Dimension x(Nr),y(Nr),z(Nr)

Double Precision xyz(Nr),xyzold(Nr),B(Nr)

Integer Ic(Nr,4)

Dimension BondL(Nr,4),BondS(Nr,4),BondK(Nr,4)

COMMON /initial1 /x,y,z

COMMON /initial2/ xyz,xyzold

```

COMMON /connect /Ic,bondL,bondS,BondK
COMMON /atom/ Np,Npts,NtotalC,NtotalBT,NtotalLR,NGIII,NGV
COMMON /out/B
COMMON Nci,Ncj,Nck
c   COMMON /Jac/A,Alu
COMMON /Jac/A
c   Integer ant1,ant2,ant3

do k = 1,Np
  do L = 1,Npts
    A(k,L) = 0.0
    A(k+Np,L) = 0.0
    A((k+2*Np),L) = 0.0
  end do

  dTx = dTy = dTz = dTxy = dTyx = dTyz = dTzx = dTzy = 0.

  do L = 1,4
    NN = Ic(k,L)
    Na = abs(NN)

    if(Na .ne.0) then
      CALL length(k,L,0,x1N,y1N,z1N)
      execute finddF

      dTx = dTx + dFx
      dTy = dTy + dFy
      dTz = dTz + dFz
      dTxy = dTxy + dFxy
      dTxz = dTxz + dFxz
      dTyx = dTyx + dFyx
      dTyz = dTyz + dFyz
      dTzx = dTzx + dFzx
      dTzy = dTzy + dFzy

      A(k,Na) = -(dFx)
      A(k,Na+Np) = -(dFxy)
      A(k,Na+2*Np) = -(dFxz)

      A(k+Np,Na) = -(dFyx)
      A(k+Np,Na+Np) = -(dFy )
      A(k+Np,Na+2*Np) = -(dFyz)

      A(k+2*Np,Na) = -(dFzx)
      A(k+2*Np,Na+Np) = -(dFzy)
      A(k+2*Np,Na+2*Np) = -(dFz)

    if (NN .lt. 0) then

```

```

    A(k,Na) = A(k,Na+Np) = A(k,Na+2*Np) = 0.0
    A(k+Np,Na) = A(k+2*Np,Na) = 0.0
    A(k+Np,Na+2*Np) = A(k+2*Np,Na+Np) = 0.0
    A(k+Np,Na+Np) = A(k+2*Np,Na+2*Np) = 0.0
  end if

end if
end do

A(k,k) = dTx
A(k,k+Np) = dTxy
A(k,k+2*Np) = dTxz

A(k+Np,k) = dTyx
A(k+Np,k+Np) = dTy
A(k+Np,k+2*Np) = dTyz

A(k+2*Np,k) = dTzx
A(k+2*Np,k+Np) = dTzy
A(k+2*Np,k+2*Np) = dTz
end do

remote block finddF
Be = bondL(k,L)
Bk = bondS(k,L)
BeL = sqrt(3*(Be**2))

Bex = sign(1.0,x1N)*Be
Bey = sign(1.0,y1N)*Be
Bez = sign(1.0,z1N)*Be

tN = x1N**2 + y1N**2 + z1N**2
t2N = sqrt(tN)
t3 = Be/t2N

dFx = -(1.0 - t3*(y1N**2 + z1N**2)/tN)*Bk
dFy = -(1.0 - t3*(x1N**2 + z1N**2)/tN)*Bk
dFz = -(1.0 - t3*(x1N**2 + y1N**2)/tN)*Bk
dFxy = -(t3*(x1N*y1N)/tN)*Bk
dFxz = -(t3*(x1N*z1N)/tN)*Bk
dFyx = -(t3*(y1N*x1N)/tN)*Bk
dFyz = -(t3*(y1N*z1N)/tN)*Bk
dFzx = -(t3*(z1N*x1N)/tN)*Bk
dFzy = -(t3*(z1N*y1N)/tN)*Bk
end block
return
end

```

SUBROUTINE LUDCMP(INDX)

c A is the input matrix from JACOB and is overwritten by ALU; A & INDX are returned. Alu is the LU decomposition of matrix A. INDX is required by LUBKSB. Do the computation in double precision;

PARAMETER (Nr = 1651, TINY = 1.0E-20)

c Dimension A(Nr,Nr),Alu(Nr,Nr)
 Dimension A(Nr,Nr)
 Double Precision INDX(Nr),VV(Nr)
 COMMON /atom/ Np,Npts,ntotalc,ntotalbt,ntotalr,NGIII,NGV

c COMMON /jac/A,Alu
 COMMON /jac/A
 double precision DSUM,DUM,Alumax

Source code (Ref. 116; page # 38)

SUBROUTINE LUBKSB(B,INDX,DER)

LU back substitution to solve $Ax = B$. Alu is the LU decomposition of A.
 The matrix is from FORCE. INDX is created in LUDCMP; Answer is in X.
 Use double precision

PARAMETER(Nr = 1651)
 Double Precision B(Nr),DER(Nr),INDX(Nr)

c Dimension A(Nr,Nr),Alu(Nr,Nr)
 Dimension A(Nr,Nr)
 DOUBLE PRECISION DSUM
 COMMON /atom/ Np,Npts,ntotalc,ntotalbt,ntotalr,NGIII,NGV

c COMMON /jac/A,Alu
 COMMON /jac/A

Source code (Ref. 116; page # 39)

SUBROUTINE MPROVE(INDX,B,X,RES)

c Iterative improvement of $Ax = B$. Alu is the LU decomposition of A.
c On output X is improved. RES is a residue that is the difference
c between the the improvement and the single precision accuracy.

PARAMETER (Nr = 1651)
 Double Precision R(Nr)

c Dimension A(Nr,Nr),Alu(Nr,Nr)
 Dimension A(Nr,Nr)
 Double Precision B(Nr),X(Nr),INDX(Nr)

```

Double precision DSUM,RES
COMMON /atom/Np,Npts,nTotalC,NtotalBT,NtotalLR,NGIII,NGV
c  COMMON /jac/A,Alu
COMMON /jac/A

```

```

DO J=1,Npts
  DSUM=-B(J)
  DO K=1,Npts
    DSUM=DSUM+(dble(A(J,K))*X(K))
  END DO
R(J)=DSUM
END DO

```

```
CALL LUBKSB(R,INDX,R)
```

```

RES=0.0
DO J=1,Npts
  RES=RES+ABS(R(J))-(1.0E-6)*ABS(X(J))
  X(J)=X(J)-R(J)
END DO
RETURN
END

```

```

SUBROUTINE NEWTON

```

```

c  solves for the equilibrium position of the atoms from SUM F = 0 using Newton-Raphson technique
    for solving non-linear set of equations

```

```

PARAMETER (Nr = 1651)
Logical check
COMMON /atom/ Np,Npts,ntotalc,ntotalbt,ntotallr,NGIII,NGV
COMMON /out/B
c  COMMON /jac/A,Alu
COMMON /jac/A
COMMON /initial2/xyz,xyzold

```

```

Double Precision B(Nr),DER(Nr),INDX(Nr)
c  Dimension A(Nr,Nr),Alu(Nr,Nr)
Dimension A(Nr,Nr)
Double Precision xyz(Nr),xyzold(Nr)
Real*8 errx,erf,chi2,chi2old,alam,tolx1,tolf1
integer nt

```

```

chi2old = 0.0
check = .false.
nt = 0
c  tolx1 = (1.e-4)*sqrt(float(Npts))
c  tofl1 = (5.e-5)*sqrt(float(Npts))

```

```

tolx1 = .008
tolf1 = 1.e-4
alam = .001
print*, 'Npts,tolx,tolf',Npts,tolx1,tolf1

do i = 1,Npts
  DER(i) = 1.e-5
end do

do j = 1,20
  nt = j
  errx = errf = chi2 = 0.0
  CALL FORCE
c   if (mod(j,2).eq.0 .or. j.eq.1) then   ! In some cases, it is not necessary to compute A for every
                                         ! iteration.
  CALL JACOB
c   end if

do k = 1,Npts
  A(k,k) = (1.0 + alam)*dble(A(k,k)) ! Followed Marquardt method for convergence (Ref. P.R.
                                     ! Bevington, and D.K. Robinson, 'Data Reduction and error
                                     ! analysis for the physical sciences', Chapter 8, McGraw Hill,
                                     ! 1992)
end do

CALL LUDCMP(INDX)
CALL LUBKSB(B,INDX,DER)

imp = 0
LOOP
  CALL MPROVE(INDX,B,DER,RES)
  imp = imp + 1
  UNTIL (RES .lt. 0.0 .or. imp .gt. 4)
  print*, 'res',res

do i = 1,Npts
  errx = errx + abs(DER(i))
  errf = errf + abs(B(i))
  chi2 = chi2 + (B(i))**2
end do
print*, 'errx',errx,'errf',errf,'chi2',chi2

if ((errx .lt. tolx1) .or. (errf .lt. tolf) .or. (Chi2 .lt. 1.e-12)) then
  goto 10
end if

do i = 1,Npts
  xyz(i) = xyz(i) + DER(i)

```

```

end do

if (chi2 .gt. chi2old)then
  alam = alam*15.0
  do i = 1,Npts
    xyz(i) = xyz(i) - DER(i)
  end do
else
  alam = alam/15.0
end if
CHI2old = chi2
end do

10  do i = 1,Npts
    print*,i,B(i),DER(i)
  end do
write(3,*)'ntrial=',nt
write(3,*)'Chi2,errx,errf values'
write(3,*)chi2,errx,errf
return
end

```

SUBROUTINE STRAIN

```

PARAMETER (Nr=1651)
Double Precision xyz(Nr),xyzold(Nr)
Dimension BondL(Nr,4),BondS(Nr,4),BondK(Nr,4)
Integer Ic(Nr,4)
REAL exx,eyy,ezz,gammaxy,gammaxz,gammayz
COMMON /initial2/xyz,xyzold
COMMON /atom/ Np,Npts,NTotalC,NtotalBT,NtotalLR,NGIII,NGV
COMMON /connect /Ic,bondL,bondS,BondK
Real E11,E22,E33,E12,E13,E23
Dimension st11(Nr),st22(Nr),st33(Nr)
Dimension st12(Nr),st13(Nr),st23(Nr)
Real Fst11,Fst22,Fst33,Fst12,Fst13,Fst23
Real Ist11,Ist22,Ist33,Ist12,Ist13,Ist23

```

Pi = 3.1415927

- c Direction cosine of the New Axes (rotated 45 deg w.r. to original X,Y,Z are:
c (cos(A),sin(A),0),(-sin(A),cos(A),0) and (0,0,1).....for the new axes X',Y',Z'
c For us the angle A = 45 deg.

```

Theta = Pi/4
DL = cos(Theta)
DM = sin(Theta)

```

```

DN = 1

do k = 1,Np
  st11(k) = st22(k) = st33(k) = 0.0
  st12(k) = st13(k) = st23(k) = 0.0
end do

do k = 1,Np
  E11 = E22 = E33 = 0.0
  E12 = E13 = E23 = 0.0

do L = 1,4
  CALL LENGTH(k,L,0,x1N,y1N,z1N)
  Be = bondL(k,L)
  Bk = bondS(k,L)
c   BeL = sqrt(3.*(Be**2))
  Bex1 = sign(1.0,x1N)*Be
  Bey1 = sign(1.0,y1N)*Be
  Bez1 = sign(1.0,z1N)*Be
  tN = x1N**2 + y1N**2 + z1N**2
c   t2N = sqrt(tN)
c   t3N = Be/t2N

  exx = (x1N - Bex1)/Bex1
  eyy = (y1N - Bey1)/Bey1
  ezz = (z1N - Bez1)/Bez1
  gammaxy = (x1N-Bex1)/Bey1 + (y1N-Bey1)/Bex1
  gammaxz = (x1N-Bex1)/Bez1 + (z1N-Bez1)/Bex1
  gammayz = (y1N-Bey1)/Bez1 + (z1N-Bez1)/Bey1

c  1 -> X'(110); 2 -> Z'(11b0); 3 -> Y'(001)
c  X1' of saada is (11b0); x1 = z; x2' = (110); x2 = x; x3 = x3' = Y
c  E11 = E110 ; E22 = E1-10 ; E12 = shear

  E11 = E11 + (exx*(DL)**2) - (2*DL*DM*gammaxz) + (ezz*(DM)**2)
  E22 = E22 + (exx*(DM)**2) + (2*DL*DM*gammaxz) + (ezz*(DL)**2)
  E33 = E33 + eyy
  E12 = E12 + ((exx-ezz)*DL*DM) + (gammaxz*(DL**2 - DM**2))
  E13 = E13 + (-gammayz*DM) + gammaxy*DL
  E23 = E23 + gammayz*DL + gammaxy*DM

end do

st11(k) = E11
st22(k) = E22
st33(k) = E33
st12(k) = E12
st13(k) = E13

```

```

    st23(k) = E23

end do

c compute net principal and shear strains

Fst11 = Fst22 = Fst33 = 0.0
Fst12 = Fst13 = Fst23 = 0.0

do k = 1,Np
    Fst11 = Fst11 + st11(k)
    Fst22 = Fst22 + st22(k)
    Fst33 = Fst33 + st33(k)
    Fst12 = Fst12 + st12(k)
    Fst13 = Fst13 + st13(k)
    Fst23 = Fst23 + st23(k)
end do

write(3,*)'principal and shear components of strain at each node'

write(3,*) k stxx stzz styy stxz stxy styz'
write(3,*)
do k = 1,Np
    write(3,31)k,st11(k),st22(k),st33(k),st12(k),st13(k),st23(k)
end do
31 FORMAT (I4,1x,6(F10.6,1x))
return
end

```

program vff DOP calculation

c April 21, 1997..Reads the output STRAIN.DAT files (due to all four different bonds) from VFFNEW.for and computes total strain layer by layer and then DOP and ROP.

```

PARAMETER (Nr = 1651)
Integer Atom
Dimension X(Nr), y(Nr), z(Nr)
Dimension gp11(Nr),gp22(Nr),gp33(Nr),gp12(Nr),gp13(Nr),gp23(Nr) ! Due Ga-P (110)
Dimension ga11(Nr),ga22(Nr),ga33(Nr), ga12(Nr),ga13(Nr),ga23(Nr) ! Due to Ga-As (110)
Dimension s11(Nr),s22(Nr),s33(Nr), s12(Nr),s13(Nr),s23(Nr) ! Due to In-As (110)
Dimension sa11(Nr),sa22(Nr),sa33(Nr), sa12(Nr),sa13(Nr),sa23(Nr) ! Due to In-As (110)
Dimension st11(Nr),st12(Nr),st22(Nr)
Real Qst11,Qst22,Qst12
Dimension DOP(101),ROP(101),QLz(101),ystep(101)
integer NoMI(101)

```

```

do k = 1,Np                                ! Np = total # of atoms
  gp11(k) = gp22(k) = gp33(k) = gp12(k) = gp13(k) = gp23(k) = 0.0
  ga11(k) = ga22(k) = ga33(k) = ga12(k) = ga13(k) = ga23(k) = 0.0
  s11(k) = s22(k) = s33(k) = s12(k) = s13(k) = s23(k) = 0.0
  sa11(k) = sa22(k) = sa33(k) = sa12(k) = sa13(k) = sa23(k) = 0.0
end do

```

- c Read 4 files corresponding to Four strained bonds:
c GaP, GaAs and InAs along [110] and InAs along [1-10].

```

open (unit=1, file='c:\watcom\lak\stcalg.txt', status='unknown', form='formatted')
j=1
loop
  read(1,5) k, gp11(j), gp22(j), gp33(j), gp12(j), gp13(j), gp23(j)
5  FORMAT (I4, 1x, 6(F10.6, 1x))
  at end, quit
  j = j+1
end loop
close (1)
Neps = j-1
print*, 'N=', Neps, Np
print*, 'Finished reading StcalG.txt -- GaP'

open (unit=2, file='c:\watcom\lak\stcall.txt', status='unknown', form='formatted')
j=1
loop
  read(2,5) k, ga11(j), ga22(j), ga33(j), ga12(j), ga13(j), ga23(j)
6  FORMAT (I4, 1x, 6(F10.6, 1x))
  at end, quit
  j = j+1
end loop
close (2)
Neps = j-1
print*, 'N=', Neps, Np
print*, 'Finished reading Stcall.txt -- GaAs'

open (unit=3, file='c:\watcom\lak\stcalK.txt', status='unknown', form='formatted')
j=1
loop
  read(3,7) k, sa11(j), sa22(j), sa33(j), sa12(j), sa13(j), sa23(j)
7  FORMAT (I4, 1x, 6(F10.6, 1x))
  at end, quit
  j = j+1
end loop
close (3)
Neps = j-1
print*, 'N=', Neps, Np
print*, 'Finished reading StcalK.txt -- InAs (1-10)'

```

```

open (unit=4, file='c:\watcom\lak\stcalL.txt', status='unknown', form='formatted')
j = 1
loop
read(4,8) k,s11(j),s22(j),s33(j),s12(j),s13(j),s23(j)
8  FORMAT (I4,1x,6(F10.6,1x))
at end, quit
j = j+1
end loop
close (4)
Neps = j-1
print*,N='Neps,Np
print*, 'Finished reading StcalL.txt --lnAs(110)'

```

- c The strained bond is between $y = 10.25$ and 10.0
- c DOP is calculated for bonds below the interface (i.e. below $y = 10.0$);
- c whereas shear is obtained including the two monolayers at the interface
- c The calibration constants to compute DOP and ROP are obtained from the V-groove expts. The max. DOP measured during these expts. was only 0.54. This factor is also taken into account while computing the calibration constant. For more details, look at VGROOVE.FOR.

```

do i = 1,34
  ystep(i) = ((i-1)*0.25) + 0.75
c  ystep(i) = (i*0.5) + 0.5
  Qst11 = Qst22 = Qst12 = 0.0
do j = 1,Np
  st11(j) = st22(j) = st12(j) = 0.0
end do

do k = 1,Np
  if ((y(k) .lt. 10.0) .and. (y(k) .gt. ystep(i))) then
c    st11(k) = -2.*s11(k) - 2.*ga11(k) + 2.*gp11(k) - 4.*sa11(k)      ! For 83% surface coverage at the
                                                                    top interface
c    st22(k) = -2.*s22(k) - 2.*ga22(k) + 2.*gp22(k) - 4.*sa22(k)
    st11(k) = -3.*s11(k) - 3.*ga11(k) + 3.*gp11(k) - 6.*sa11(k)      !For 75% surface coverage at the
                                                                    top interface
    st22(k) = -3.*s22(k) - 3.*ga22(k) + 3.*gp22(k) - 6.*sa22(k)
    Qst11 = Qst11 + st11(k)
    Qst22 = Qst22 + st22(k)
  end if

  if ((y(k) .lt. 10.75) .and. (y(k) .gt. ystep(i))) then
c    st12(k) = -2.*s12(k) - 2.*ga12(k) + 2.*gp12(k) - 4.*sa12(k)
    st12(k) = -3.*s12(k) - 3.*ga12(k) + 3.*gp12(k) - 6.*sa12(k)
    Qst12 = Qst12 + st12(k)
  end if
end do

```

c since both 'TOP' and 'BOTTOM' bonds are considered on all layers, the total thickness becomes NoML
 • 1.46; Factor 2 in the denominator is due to double counting of each bond
 c The calibration factors are: $DOP(exp) = -37.885 * stdiff(Ansys) + 1.48$;
 $ROP(exp) = -22.99 * Gamma(Ansys) - 0.274$

```

      NoML(i) = Int(((10.0 - ystep(i))*4) - 1)
c      NoML(i) = Int((10.0 - ystep(i))*2)
      QLz(i) = NoML(i) * 1.46
      DOP(i) = -(Qst11 - Qst22)*37.885*100.0 / (2*NoML(i))
      DOP(i) = DOP(i) + 1.48
      ROP(i) = -(Qst12*22.99*100.0) / ((2*NoML(i))+3)
      ROP(i) = ROP(i) - 0.274
    end do

    open (unit = 5, file = 'c:\watcom\lak\vffdop1.txt', form='formatted')
    write (5,*)'Values obtained using VFFdopcal.for'
    write (5,*) 'Files used: stcalG.txt, stcalI.txt, stcalK.txt, stcalL.txt'
    write (5,*)'y(i), No. of MLs, Lz, DOP (%), ROP (%)'
10    FORMAT (F6.2,2x,I4,2x,F8.3,2(2x,F10.6))
      do i = 1,34
        write (5,10) ystep(i),NoML(i),QLz(i),DOP(i),ROP(i)
      end do
    close(5)
  end

```

References

1. S. Adachi, 'Material parameters of $\text{In}_{1-x}\text{Ga}_x\text{As}_y\text{P}_{1-y}$ and related binaries', *J. Appl. Phys.* **53**(12), 8775-8792, 1982.
2. T.P. Pearsall, ed., 'GaInAsP alloy semiconductors', John Wiley & Sons, New York, 1982.
3. R.E. Nahory, F.A. Pollack, W.D. Johnston Jr., and R.L. Barns, 'Band gap versus composition and demonstration of Vegard's law for $\text{In}_{1-x}\text{Ga}_x\text{As}_y\text{P}_{1-y}$ lattice matched to InP', *Appl. Phys. Lett.* **33**, 659-661, 1978.
4. E. Khupal, 'Phase diagrams of InGaAsP, InGaAs and InP lattice-matched to (100) InP', *J. Cryst. Growth*, **67**, 441-457, 1984.
5. G.P. Agrawal, and N.K. Dutta, 'Long-wavelength semiconductor lasers', Van Nostrand Reinhold Company, 1986.
6. J.R. Arthur, 'Interaction of Ga and As₂ molecular beams with GaAs surfaces', *J. Appl. Phys.*, **39**, 4032-4034, 1968.
7. A.Y. Cho, 'Film deposition by molecular-beam techniques', *J. Vac. Sci. Technol.* **8**, S31-S32, 1971.
8. A.Y. Cho, 'Growth of periodic structures by the molecular-beam method', *Appl. Phys. Lett.*, **19**, 467-468, 1971.
9. R. Dingle, 'Confined carrier quantum states in ultrathin semiconductor heterostructures *Festkörperprobleme XV*, 21-48, 1976.
10. R. Dingle, W. Wiegmann, and C.H. Henry, 'Quantum states of confined carriers in very thin AlGaAs-GaAs-AsGaAs heterostructures', *Phys. Rev. Lett.* **33**, 827-830, 1974.
11. L.L. Chang, L. Esaki, and R. Tsu, 'Resonant tunneling in semiconductor double barriers', *Appl. Phys. Lett.* **24**, 593-595, 1974.
12. M.B. Panish, H. Temkin, R.A. Hamm, and S.N.G. Chu, 'Optical properties of very thin GaInAs(P)/InP quantum wells grown by gas source molecular beam epitaxy', *Appl. Phys. Lett.*, **49**, 164-166, 1986.

13. R.C. Miller, D.A. Kleinman, W.T. Tsang, and A.C. Gossard, 'Observation of the excited level of excitons in GaAs quantum wells', *Phys. Rev. B* **24**, 1134-1136, 1981.
14. J.W. Matthews and A.E. Blakeslee, 'Defects in epitaxial multilayers', *J. Cryst. Growth* **27**, 118-125, 1974.
15. J. Honstra and W.J. Bartels, 'Determination of the lattice constant of epitaxial layers of III-V compounds', *J. Crystal Growth*, **44**, 513-517, 1978.
16. G.E. Pikus and G.L. Bir, 'Effect of deformation on the hole energy spectrum of germanium and silicon', *Sov. Phys. Solid State* **1**, 1502-1517 (1960).
17. R. Dingle, Ed., 'Applications of multiquantum wells, selective doping and superlattices', *Semiconductors and semimetals*, **24**, Chapter 8, Ed. By R.K. Williardson and A.C. Beer, Academic Press, San Diego, 1987.
18. P. Voisin, C. Delande, M. Voos, L.L. Chang, A. Segmuller, C.A. Chang, and L. Esaki, 'Light and heavy valence subband reversal in GaSb-AlSb superlattices', *Phys. Rev. B*, **30**, 2276-2278, 1984.
19. R. Sooryakumar and D.S. Chemla, A. Pinczuk, A.C. Gossard, W. Wiegmann, and L.J. Sham, 'Valence band mixing in GaAs-(AlGa)As heterostructures', *Solid State Commun.* **54**, 859-862, 1985.
20. I.C. Bassignana, C.J. Miner, and N. Puetz, 'Photoluminescence and double-crystal x-ray study of InGaAs/InP: Effect of mismatch strain on band gap', *J. Appl. Phys.* **65**, 4299-4305, 1989.
21. D. Gershoni and H. Temkin, 'Optical properties of III-V strained-layer quantum wells', *J. Lumin.* **44**, 381-398, 1989.
22. E.P. O'Reilly, 'Valence band engineering in strained layer structures', *Semicond. Sci. Technol.* **4**, 121-137, 1989.
23. M.A. Herman, D. Bimberg, and J. Christen, 'Heterointerfaces in quantum wells and epitaxial growth processes: Evaluation by luminescence techniques', *J. Appl. Phys.* **70**, R1-R51, 1991.
24. J. Singh and K.K. Bajaj, 'Role of interface roughness and alloy disorder in photoluminescence in quantum-well structures', *J. Appl. Phys.* **57**, 5433-5437, 1985.

25. C.W. Tu, R.C. Miller, B.A. Wilson, P.M. Petroff, T.D. Harris, R.F. Kopf, S.K. Sputz, and M.G. Lamont, 'Properties of (Al,Ga)As/GaAs heterostructures grown by molecular beam epitaxy with growth interruptions', *J. Crystal Growth* **81**, 159-163, 1987.
26. D. Bimberg, D. Mars, J.N. Miller, R. Bauer, and D. Oertel, 'Structural changes of the interface, enhanced interface incorporation of acceptors, and luminescence efficiency degradation in GaAs quantum wells grown by molecular beam epitaxy upon growth interruption', *J. Vac. Sci. Technol.* **B4**, 1014-1021, 1986.
27. T. Hayakawa, T. Suyama, K. Takahashi, M. Kondo, S. Yamamoto, S. Yano, and T. Hijikata, 'Interface disorder in GaAs/AlGaAs quantum wells grown by MBE', *Surface Science* **174**, 76-81, 1986.
28. J.M. Vandenberg, M.B. Panish, R.A. Hamm, and H. Temkin, 'Modification of intrinsic strain at lattice-matched GaInAs/InP interfaces', *Appl. Phys. Lett.* **56**, 910-912, 1990.
29. A. Tabata, T. Benyattou, G. Guillot, S.A. Clark, J.E. Macdonald, D.I. Westwood, and R.H. Williams, 'Strain relaxation studied by photoluminescence and by double crystal X-ray diffraction measurements in strained InGaAs', *Mat. Sci. and Engineering*, **B22**, 222-226, 1994.
30. P. van der Sluis, 'Determination of strain in epitaxial semiconductor structures by high-resolution X-ray diffraction', *Appl. Phys. A* **58**, 129-134, 1994.
31. P.D. Colbourne, and D.T. Cassidy, 'Bonding stress measurements from the degree of polarization of facet emission of AlGaAs superluminescent diodes', *IEEE J. Quantum Electron.* **27**, 914-920, 1991.
32. P.D. Colbourne and D.T. Cassidy, 'Imaging of stresses in GaAs diode lasers using polarization-resolved photoluminescence', *IEEE J. Quantum Electron.* **29**, 62-68, 1993.
33. Jian Yang, and D.T. Cassidy, 'Strain measurement and estimation of photoelastic effects and strain-induced gain change in ridge waveguide lasers', *J. Appl. Phys.* **77**, 3382-3387, 1995.
34. P.D. Colbourne, and D.T. Cassidy, 'Dislocation detection using polarization-resolved photoluminescence', *Can. J. Phys.* **70**, 803-812, 1992.

35. M. Yamanishi and I. Suemune, 'Comment on polarization dependent momentum matrix elements in quantum well lasers', *Jap. J. Appl. Phys.* **23**, L35-L36, 1984.
36. M. Asada, A. Kameyama, and Y. Suematsu, 'Gain and intervalence band absorption in quantum well lasers', *J. Quantum Electronics*, **QE-20**, 745-753, 1984.
37. B. Lakshmi, D.T. Cassidy, and B.J. Robinson, 'Quantum well strain and thickness characterization by degree of polarization', *J. Appl. Phys.* **79**, 7640-7645, 1996.
38. C.T. Foxon and B.A. Joyce, 'Surface processes controlling the growth of GaInAs and GaInP alloy films by MBE', *J. Crystal Growth*, **44**, 75-83, 1978.
39. D.E. Aspnes, M.C. Tamargo, M.J.S.P. Brasil, R.E. Nahory and S.A. Schwartz, 'As capture and the growth of ultrathin InAs layers on InP', *Appl. Phys. Lett.* **64**, 3279-3281, 1994.
40. J. Jönsson, F. Reinhart, M. Zorn, K. Ploska, W. Richter, and J. Rumberg, 'In situ time-resolved monitoring of PH₃ induced exchange reactions on GaAs under metalorganic vapor phase epitaxy conditions', *Appl. Phys. Lett.* **64**, 1998-2000, 1994.
41. M. Zorn, J. Jönsson, W. Richter, J.-T. Zettler, and K. Ploska, 'Anisotropic reflectance from semiconductor surfaces for in-situ monitoring in epitaxial growth systems', *Phys. Stat. Sol. (a)* **152**, 23-34, 1995.
42. K. Knorr, A. Rumberg, M. Zorn, C. Meyne, T. Trepk, J.-T. Zettler, W. Richter, P. Kurpas and M. Weyers, 'Real-time monitoring of P-based semiconductor growth by linear-optical spectroscopy', *Proc. of the Eighth International Conference on Indium Phosphide and Related Materials*, Schwäbisch Gmünd, Germany, WP-C 33 (1996).
43. B.R. Bennett, J.A. Del Alamo, M.T. Sinn, F. Peiro, A. Cornet, and D.E. Aspnes, 'Origin of optical anisotropy in strained InGaAs/InP and InAlAs/InP heterostructures', *Journal of Electronic Materials*, **23**, 423-429, 1994.
44. Guang-Jye Shiau, Chih-Ping Chao, Paul E. Burrows, and Stephen R. Forrest, 'Growth of abrupt InGaAs(P)/InP(GaAs)P heterointerfaces by gas source molecular beam epitaxy', *J. Appl. Phys.* **77**, 201-209, 1995.
45. W.G. Bi, and C.W. Tu, ' Optimization and characterization of interfaces of InGaAs/InGaAsP quantum well structures grown by gas-source molecular beam epitaxy', *J. Appl. Phys.* **78**, 2889-2891, 1995.

46. R. Benzaquen, and A.P. Roth, ' Structural and optical characterization of monolayer interfaces in GaInAs/InP multiple quantum wells grown by chemical beam epitaxy', *J. Appl. Phys.* **79**, 2640-2648, 1996.
47. G. Hollinger, D. Gallet, M. Gendry, C. Santinelli, and P. Viktorovitch, ' Structural and chemical properties of InAs layers grown on InP(100) surfaces by arsenic stabilization', *J. Vac. Sci. Technol.* **B8**, 832-837, 1990.
48. K. Mahalingam, Y. Nakamura, N. Otsuka, H.Y. Lee, M.J. Hafich, and G.Y. Robinson, 'TEM study of the effect of growth interruption in MBE of InGaP/GaAs superlattices', *J. Electronic Materials*, **21**, 129-133, 1992.
49. A.Y. Lew, C.H. Yan, C.W. Tu, and E.T. Yu, ' Characterization of arsenide/phosphide heterostructure interfaces grown by gas-source molecular beam epitaxy', *Appl. Phys. Lett.* **67**, 932-934, 1995.
50. E. Zolotoyabko, Y. Finkelstein, M. Blumina, and D. Fekete, ' X-ray diffraction in quantum-well structures', *Physica B*, **221**, 487-493, 1996.
51. A.R. Clawson, and C.M. Hanson, ' Interface strain in InGaAs-InP superlattices', *J. of Electronic Materials*, **25**, 739-744, 1996.
52. M.G. Proietti, S. Turchini, J. Garcia, G. Lamble, F. Martelli, and T. Prospero, 'Microscopic structure of strained InGaAs/GaAs heterostructures', *Solid-State Electronics*, **40**, 653-658, 1996.
53. B.Lakshmi, B.J. Robinson, and Daniel T. Cassidy, '[001] interface anisotropy using degree of polarization', *Proc. of the Eighth International Conference on Indium Phosphide and Related Materials*, Schwäbisch Gmünd, Germany, MA1-4, 27 1996.
54. B. Lakshmi, B.J. Robinson, D.T. Cassidy, and D.A. Thompson, 'Anisotropic interfacial strain in InP/InGaAs/InP quantum wells studied using degree of polarization of photoluminescence', *J. Appl. Phys.* **81**, 3616-3621, 1997.
55. B. Lakshmi, D.T. Cassidy, B.J. Robinson, and D.A. Thompson, 'Anisotropic interfacial strain in InP/InGaAs/InP quantum wells', *To be submitted to J. Appl. Phys.*
56. B. Lakshmi, and D.T. Cassidy, 'Technique for simultaneous measurement of difference in the normal components of strain and shear strain using degree of polarization of photoluminescence', *To be published.*

57. F.H. Peters, and D.T. Cassidy, 'Spatially and polarization resolved electroluminescence of 1.3 μm InGaAsP semiconductor diode lasers', *Applied Optics* **28**, 3744-3750, 1989.
58. D.T. Cassidy, 'Phase sensitive detectors', Documentation, McMaster University, 1994.
59. T. Arakawa, S. Tsukamoto, Y. Nagamune, M. Nishioka, 'Fabrication of InGaAs strained quantum wire structures using selective-area metal-organic chemical vapor deposition growth', *Jpn. J. Appl. Phys.* **32**, L1377-L1379, 1993.
60. K. Kash, B.P. Van der Gaag, D.D. Mahony, A.S. Gozdz, L.T. Florez, J.P. Harbison, and M.D. Sturge, 'Observation of quantum confinement by strain gradients', *Phys. Rev. Lett.* **67**, 1326-1329.
61. S.C. Jain, M. Willander, and H. Maes, 'Stresses and strains in epilayers, stripes, and quantum structures of III-V compound semiconductors', *Semicond. Sci. Technol.* **11**, 641-671, 1996.
62. A. Gupta, G.C. Weatherly, D.T. Cassidy, and D.M. Bruce, 'Characterization and modelling of the strain fields associated with InGaAs layers on V-grooved InP substrates', submitted to *J. Appl. Phys.*
63. P.D. Colbourne, 'Measurement of stress in III-V semiconductors using the degree of polarization of luminescence', Ph.d thesis, McMaster University, 1992.
64. S. Timoshenko, and J.N. Goodier, 'Theory of Elasticity', McGraw Hill, New York, 1951.
65. 'Properties of Indium Phosphide', INSPEC, New York, 1991.
66. E.H.C. Parker, Editor, 'The technology and physics of molecular beam epitaxy', Plenum Press, New York, 1985.
67. M.B. Panish, and H. Temkin, 'Gas source molecular beam epitaxy - Growth and properties of Phosphorous containing III-V heterostructures', Springer-Verlog, Berlin, 1993.
68. A. Katz, Editor, 'Indium Phosphide and related materials: Processing, technology, and devices', Artech House, Boston, 1992.

69. A.Y. Cho, 'Bonding direction and surface-structure orientation on GaAs (001)', *J. Appl. Phys.* **47**, 2841-2843, 1976.
70. E.A. Wood, 'Vocabulary of surface crystallography', *J. Appl. Phys.* **35**, 1306-1312, 1964.
71. E.H.C. Parker, Editor, 'The technology and physics of molecular beam epitaxy: Chapter 9', Plenum Press, New York, 1985.
72. Y. Tang, D.H. Rich, E.H. Lingunis, and N.M. Haegel, 'Polarized-cathodoluminescence study of stress fro GaAs grown selectively on patterned Si(100)', *J. Appl. Phys.* **76**, 3032-3040, 1994.
73. G.S. Horner, A. Mascarenhas, R.G. Alonso, D.J. Friedman, K. Sinha, K.A. Bertness, J.G. Zhu, and J.M. Olson, 'Polarized photoluminescence measurements of the valence-band splitting in single-variant, spontaneously ordered GaInP₂', *Phys. Rev. B* **48**, 4944-4947, 1993.
74. T. Kanata, M. Nishimoto, H. Nakayama, and T. Nishino, 'Valence-band splitting in ordered GaInP studied by temperature-dependent photoluminescence polarization', *Phys. Rev. B* **45**, 6637-4947, 1992.
75. R.J. Thomas, H.R. Chandrasekhar, M. Chandrasekhar, E.D. Jones, and R.P. Schneider, 'Polarized photomodulated reflectivity and photoluminescence studies of ordered InGaP₂ under pressure', *J. Phys. Chem. Solids* **56**, 357-362, 1995.
76. D.V. Korbutyak, V.G. Litovchenko, L.V. Troschchenko, S.G. Krylyuk, H.T. Grahn, and K. Ploog, 'Polarization effects in semiconductor superlattices', *Semicond. Sci. Technol.* **10**, 422-424, 1995.
77. T. Shima, J-S. Lee, K. Kudo, K. Tanaka, S. Niki, A. Yamada, and Y. Makita, 'Polarization-resolved photoluminescence of InAs/GaAs strained structures on variously oriented substrates', *Applied Surface Science* **75**, 164-168, 1994.
78. F. Clerot, H.L. Haridon, A. Le Corre, A. Godefroy, S. Salaün, and A. Ponchet, 'Simulation and photoluminescence characterization of transverse electric-transverse magnetic emission of strained Ga_{0.47}In_{0.53}As/Ga_{0.62}In_{0.38}As superlattices', *Materials Science and Engineering* **B31**, 293-297, 1995.
79. W. Monch, 'Semiconductor surfaces and interfaces', Springer series in surface sciences 26, 1993.

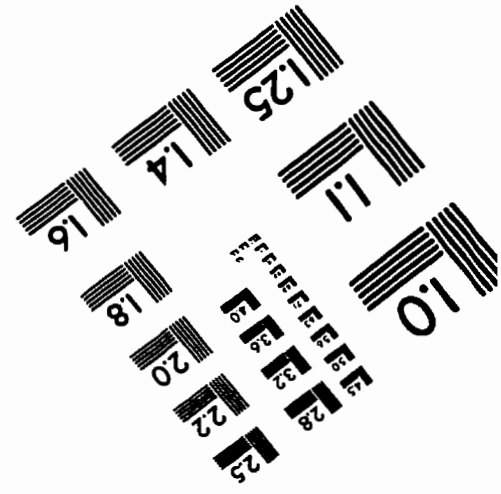
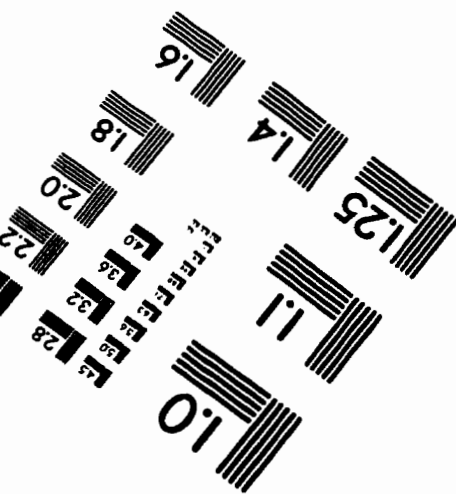
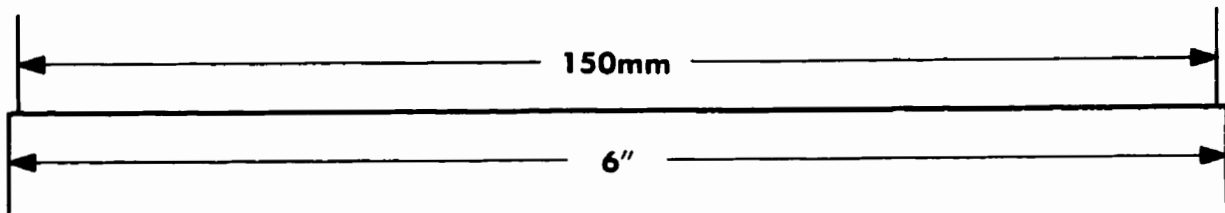
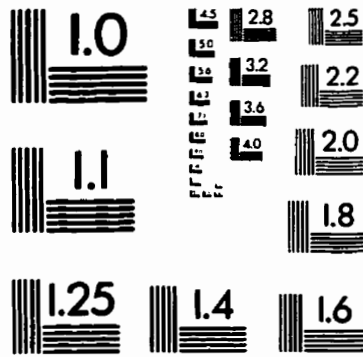
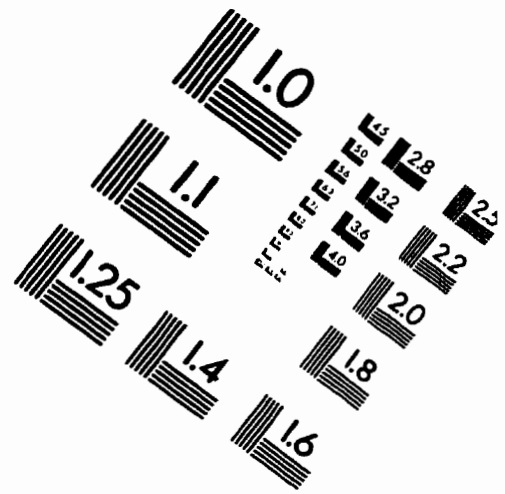
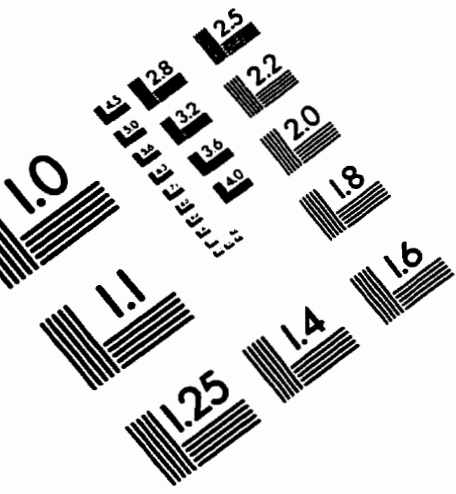
80. J. Yang, 'Study of III-V semiconductors by spatially-resolved and polarization-resolved photoluminescence', *Ph.d thesis, McMaster University, 1995*.
81. E.O. Kane, 'Band structure of Indium Antimonide', *J. Phys. Chem. Solids* **1**, 249-261, 1957.
82. M. Yamada, S. Ogita, M. Yamagishi, K. Tabata, N. Yakaya, M. Asada, and Y. Suematsu, 'Polarization-dependent gain in GaAs/AlGaAs multi-quantum-well lasers: Theory and experiment', *Appl. Phys. Lett.* **45**, 324-325, 1984.
83. C. Weisbuch, 'Optical properties of quantum wells', NATO ASI series B, 'Physics and applications of quantum wells and superlattices', ed. E.Z. Mendez, and K.Von Klitzing, 1987.
84. D. Ahn, and S-L. Chuang, 'Optical gain in a strained-layer quantum-well laser', *IEEE J. Quantum Electron.* **24**, 2400- 2406, 1988.
85. S.L. Chuang, 'Efficient band-structure calculations of strained quantum wells', *Phys. Rev. B* **43**, 9649-9661, 1991.
86. S. Seki, T. Yamanaka, W. Lui, Y. Yoshikuni, and K. Yokoyama, 'Theoretical analysis of pure effects of strain and quantum confinement on differential gain in InGaAsP/InP strained-layer quantum well lasers', *IEEE J. Quantum Electron.* **30**, 500-510, 1994.
87. I. Vurgaftman, J.M. Hincley, and J. Singh, 'A comparison of optoelectronic properties of lattice-matched and strained quantum-well and quantum-wire structures', *IEEE J. Quantum Electron.* **30**, 75- 84, 1994.
88. A. Baliga, D. Trivedi, and N.G. Anderson, 'Tensile-strain effects in quantum-well superlattice band structures', *Phys. Rev. B* **49**, 10402-10416, 1994.
89. C-S. Chang, and S.L. Chuang, 'Universal curves for optical-matrix elements of strained quantum wells', *Appl. Phys. Lett.* **66**, 795- 797, 1995.
90. G. Bastard, 'Wave-mechanics applied to semiconductor heterostructures', Chapter 7, Les Ulis Cedex, France, Les Editions de Physique, New York, Halsted Press, 1988
91. S.L. Chuang, 'Physics of optoelectronic devices', John Wiley & Sons, New York, 1995.

92. P.S. Zory, Jr., Editor, 'Quantum well lasers', Chapter 2, Academic press, New York, 1993.
93. G. Bastard, 'Superlattice band structure in the envelope-function approximation', *Phys. Rev. B* **24**, 5693-5697, 1981.
94. G. Bastard, and J.A. Brum, 'Electronic states in semiconductor heterostructures', *IEEE J. Quantum Electron.* **22**, 1625- 1644, 1986.
95. D. Ahn, and S.J. Yoon, 'Theory of optical gain in strained-layer quantum wells within the 6x6 Luttinger-Kohn model', *J. Appl. Phys.* **78**, 2489-2497, 1995.
96. R. Sooryakumar, A. Pinczuk, A.C. Gossard, D.S. Chemla, and L.J. Sham, 'Tuning of the valence-band structure of GaAs quantum wells by uniaxial stress', *Phys. Rev. Lett.* **58**, 1150-1153, 1987.
97. M. Tanaka, and H. Sakaki, 'Atomistic models of interface structures of GaAs-AlGaAs quantum wells grown by interrupted and uninterrupted MBE', *J. Cryst. Growth* **81**, 153-158, 1987.
98. H.H. Farrell, and C.J. Palmstrom, 'Reflection high energy electron diffraction characteristic absences in GaAs (100) (2x4)-As: A tool for determining the surface stoichiometry', *J. Vac. Sci. Technol* **B8**, 903-907, 1990.
99. D.J. Chadi, 'Atomic structure of GaAs (100)-(2x1) and (2x4) reconstructed surfaces', *J. Vac. Sci. Technol.* **A5**, 834-837, 1987.
100. D.K. Biegelsen, R.D. Bringans, J.E. Northrup, and L.-E. Swartz, 'Surface reconstruction of GaAs (100) observed by scanning tunneling microscopy', *Phys. Rev. B* **41**, 5701-5706, 1990.
101. B.X. Yang, L. He, and H. Hasegawa, 'Properties of InAsP layer formed by P-As exchange reaction on (001) InP surface exposed to As₄ beam', *J. Electronic Materials* **25**, 379-384, 1996.
102. T. Anan, S. Sugou, and K. Nishi, 'Improvement of InP/InGaAs heterointerfaces grown by gas source molecular beam epitaxy', *Appl. Phys. Lett.* **63**, 1047-1049, 1993.
103. H.Y. Lee, M.J. Hafich, and G.Y. Robinson, 'The effect of growth pause on the composition of InGaP/GaAs heterointerfaces', *J. Cryst. Growth* **105**, 244-248, 1990.

104. Landolt-Bornstein Numerical Data and Functional Relationship in Science and Technology, New Series, edited by O. Madelung, Group **III/17a** (1982), **22a** (1987).
105. M.J.P. Musgrave and J.A. Pople, 'A general valence force field for diamond', *Proc. Roy. Soc. A* **268**, 474-484, 1962.
106. R.M. Martin, 'Elastic properties of ZnS structure semiconductors', *Phys. Rev. B* **1**, 4005-4011, 1970.
107. R.M. Martin, 'Effect of invariance requirements on the elastic strain energy of crystals with application to the diamond structure', *Phys. Rev.* **145**, 637-645, 1966.
108. R.M. Martin, 'Relationship between elastic tensors of Wurtzite and zinc-blend structure materials', *Phys. Rev. B* **6**, 4546-4553, 1972.
109. W.A. Harrison, 'Electronic structure and the properties of solids: The physics of the chemical bond', W.H. Freeman and Co., 1980.
110. Y. Cai, and M.F. Thorpe, 'Length mismatch in random semiconductor alloys. I. General theory for quaternaries', *Phys. Rev. B* **46**, 15872-15878, 1992.
111. Y. Cai, and M.F. Thorpe, 'Length mismatch in random semiconductor alloys. II. Structural characterization of pseudobinaries', *Phys. Rev. B* **46**, 15879-15886, 1992.
112. Y. Cai, and M.F. Thorpe, 'Length mismatch in random semiconductor alloys. III. Crystalline and amorphous SiGe', *Phys. Rev. B* **46**, 15887-15893, 1992.
113. J.C. Wojcik, J.G. Pellegrino, S.H. Southworth, P.S. Shaw, B.A. Karlin, and C.E. Bouldin, 'Accommodation of strain in ultrathin InAs/GaAs films', *Phys. Rev. B* **52**, R2281-R2284, 1995.
114. J.G. Kirkwood, 'The skeletal modes of vibration of long chain molecules', *J. Chem. Phys.* **7**, 506-509, 1939.
115. K.H. Huebner, E.A. Thornton, and T.G. Byrom, 'The finite element method for engineers', John-Wiley & Sons, Inc., 1995.
116. W.H. Press, S.A. Teukolsky, W.T. Vetterling, and B.P. Flannery, 'Numerical recipes in Fortran: The art of scientific computing', Cambridge University press, 1992.
117. Part Number: 900-series Biaxial clinometer, Applied Geomechanics, Santa Cruz, California.

118. P. Ramvall, N. Carlsson, P. Omling, L. Samuelson, W. Seifert, M. Stolze, and Q. Wang, 'GaInAs/InP quantum wells with extremely high and anisotropic two-dimensional electron gas mobilities', *Appl. Phys. Lett.* **86**, 1111-1113, 1996.
119. F. Riesz, 'Rotated tilting in lattice-matched heteroepitaxial systems', *J. Cryst. Growth*, **140**, 213-218, 1994.

IMAGE EVALUATION TEST TARGET (QA-3)



APPLIED IMAGE, Inc
 1653 East Main Street
 Rochester, NY 14609 USA
 Phone: 716/482-0300
 Fax: 716/288-5989

© 1993, Applied Image, Inc., All Rights Reserved